GEOMORPHIC CONTROLS ON HYPORHEIC EXCHANGE

by

Byron Edward Amerson

A dissertation submitted in partial fulfillment
of the requirements for the degree

of

Doctor of Philosophy

in

Ecology and Environmental Sciences

MONTANA STATE UNIVERSITY
Bozeman, Montana

May 2026

DEDICATION

I dedicate this work to Mom and Pop. My salty, lovable, incorrigible, and absurdly hilarious father Edward Floyd Amerson, died much too young at age 47, on February 22nd, 1992. My loving, supportive, comedic and truly unique mother also died much too young at the age of 79 on October 17th, 2025. We are going to play Farkle in heaven.

ACKNOWLEDGMENTS

This research was conducted on the ancestral homelands of the Cayuse, Umatilla, and Walla Walla peoples, whose relationship with this land extends far beyond the span of any scientific study. The Confederated Tribes of the Umatilla Indian Reservation (CTUIR) have stewarded the rivers of this region since time immemorial, and I was privileged to work within a landscape central to their First Foods river vision. Meacham Creek was restored to support the water and fish, and I am grateful for the opportunity to have contributed, however modestly, to that effort.

This work would not have been possible without Geoffrey Poole. His patience, creative insight, and tolerant disposition carried this project through more than a few difficult stretches. I am also deeply grateful to Scott O'Daniel, whose friendship, scientific generosity, and thoughtful engagement shaped this work at every stage. At the CTUIR, Eric Quaempts, Jim Webster, and Mike Lambert provided support, guidance, and were instrumental in securing the funding that made this research possible. That funding came from the Bonneville Power Administration, the Columbia River Inter-Tribal Fish Commission (CRTFC), and the Oregon Watershed Enhancement Board, and I thank each of those organizations for their investment in applied science.

My doctoral committee shaped this work in ways large and small. Stephanie Ewing was a founding member of the committee and consistently pushed me toward greater rigor, both in analysis and in how I communicated the results. Rob Payne joined later, after moving from a postdoctoral position in Geoff's lab to a faculty appointment of his own. He joined me in the field during my first season in 2010 and introduced me to tracer methods in stream hydrology, and on winter days away from the work he was reliably good company on cross country skis, mulled wine in tow. Glenn Shaw received an out-of-the-blue request from a graduate student asking to borrow twenty thousand dollars worth of brand-new radon sampling equipment, and he said yes. He subsequently gave generously of his time and was good company through that chapter of the work. The radon data never made it into the final dissertation, but his generosity is not forgotten.

Andrea Brookfield answered a cold call from a modeler in distress, welcomed me to her lab, and spent several generous days walking me through the subtleties of *HydroGeoSphere*. That act of collegial kindness changed the trajectory of this work.

Finally, thank you to my family and friends, who supported me through a process that was longer and stranger than any of us anticipated. I am still a little astonished that I made it through.

TABLE OF CONTENTS

TABLE OF CONTENTS – CONTINUED

TABLE OF CONTENTS – CONTINUED

LIST OF TABLES

LIST OF TABLES – CONTINUED

LIST OF TABLES – CONTINUED

LIST OF FIGURES

LIST OF FIGURES – CONTINUED

LIST OF FIGURES – CONTINUED

ABSTRACT

Water moves continuously between rivers and the gravel aquifers beneath their floodplains, sustaining cold-water refuges, aquatic life, and water quality. Stream restoration projects reshape channels and floodplains to recover this subsurface exchange, but practitioners cannot predict how specific design choices change it across the range of flows that matter ecologically. This dissertation closes that gap through three studies at Meacham Creek, a salmon-bearing tributary in northeastern Oregon.

The first study evaluates a temperature-based analytical method for characterizing the gravel aquifers beneath floodplains. Heat-transport simulations show that the method yields reliable estimates in a "proximal zone" near the channel. Farther away, heat exchanges with the atmosphere and bedrock distort the temperature signal and degrade the estimates.

The second study uses a three-dimensional hydrogeologic model to quantify how restoration changes subsurface exchange across baseflow, bankfull, and flood conditions. The framework separates total exchange into two parts: the wetted area available for exchange, and the rate at which water moves through each unit of that area.

The third study attributes the restoration effect to three geomorphic outcomes: channel and floodplain area, channel complexity, and alluvial depth. Expanding wetted area produces the largest gains at most flows. Channel complexity dominates at intermediate flows and fades during floods. Alluvial depth contributes modestly and is fixed by site geology.

Together, these studies form a connected toolkit for measuring, quantifying, and attributing restoration's effects on subsurface exchange. The framework lets practitioners ground restoration design in a physical accounting of which choices yield the largest subsurface returns at the flows most relevant to a project's ecological goals.

INTRODUCTION

Hyporheic Exchange in Mountain Drainage Basins

In mountain drainage basins, streams and their alluvial aquifers exchange water continuously, a process known as *hyporheic exchange*. Water infiltrates the streambed, travels through the alluvium, and returns to the channel [64], creating subsurface flow paths that extend vertically beneath individual bedforms and laterally across floodplain aquifers [11]. Along the way, the water exchanges heat with the sediment matrix, reacts with mineral surfaces, and sustains microbial communities, with transformations accumulating as flow paths lengthen and velocities slow [89]. Because transit times range from hours beneath individual bedforms to months across floodplain aquifers, water returns to the stream in varying states of thermal and chemical transformation, buffering stream temperatures, processing nutrients, and sustaining aquatic habitat [17, 34]. How much water moves through the hyporheic zone, how fast, and through what volume of sediment shapes the subsurface contribution to stream ecosystem function. Restoration practitioners increasingly recognize this, seeking to recover subsurface hydrologic processes rather than channel form alone [41]. Yet what geomorphic research has learned about the controls on exchange and what practitioners can apply at a project site remain largely disconnected. The dissertation that follows examines how stream restoration modifies hyporheic exchange, and through what physical mechanisms, bringing hyporheic process research into closer contact with restoration practice.

Geomorphic Controls on Hyporheic Exchange

Geomorphic controls on hyporheic exchange are hierarchically organized. Valley-scale constraints, including confinement, gradient, sediment supply, and the depth of alluvium above bedrock, determine the channel types a reach can support [60]. Channel type, in turn, integrates these constraints at the reach scale, producing characteristic bed topography, planform geometry, and cross-section shape [20, 60]. A pool-riffle channel, for example, develops the amplitude and wavelength of bed topography that a plane-bed channel in the same valley setting cannot sustain, and with that topography come larger near-bed pressure variations and deeper penetration of flow into the alluvium. Channel type also determines cross-section geometry and the approximately power-law relationships that describe how wetted width, depth, and area scale with discharge [48, 49]. A wide, shallow pool-riffle channel wets substantially more streambed at a given flow than a narrow, incised plane-bed channel, and that difference compounds as discharge rises.

Buffington and Tonina [20, 80] extended this geomorphic framework into the subsurface, demonstrating that exchange flux, storage volume, and residence time distributions scale predictably with the morphometric variables that define channel type, a relationship subsequent work has confirmed across nested spatial scales [42, 56, 64, 84]. Bed topography, planform heterogeneity, cross-section shape, alluvial depth, and wetted area are not independent properties a channel happens to possess. They co-vary because the same valley-scale boundary conditions shape them all. Restoration projects modify these same variables, within the constraints the valley setting allows.

Temperature as a Natural Tracer

As stream water infiltrates the subsurface, it carries a thermal signal that damps in amplitude and lags in phase with distance along the flow path [2, 27]. How quickly the signal attenuates depends on how fast the water moves and how readily the sediment matrix conducts and stores heat. Analytical solutions of the one-dimensional advection-diffusion equation exploit this relationship, extracting estimates of Darcy velocity, hydraulic conductivity, and thermal diffusivity from paired temperature records without requiring artificial tracers or complex instrumentation [39, 52, 73]. The approach works well for daily temperature signals penetrating centimeters to meters vertically into streambeds, where longitudinal advection dominates the energy balance and the one-dimensional assumption holds [40, 45]. Annual temperature signals in floodplain aquifers damp and lag over horizontal distances of tens to hundreds of meters in an analogous way [6, 63]. But at these scales, heat exchange with the atmosphere and underlying bedrock may overwhelm the longitudinal signal on which the analytical solutions depend. Whether the one-dimensional advection-diffusion equation can reliably estimate aquifer properties under these conditions has not been tested.

Stream Restoration and Hyporheic Exchange

Stream restoration practice has evolved through distinct paradigms, each emphasizing different aspects of channel and floodplain recovery. Form-based approaches recreate characteristic morphologies such as pool-riffle sequences and meander geometry, drawing on channel classification and reference reach design [9, 71]. Process-based strategies remove constraints on fluvial processes, such as levees and bank armoring, and allow the channel to rebuild appropriate morphology through natural sediment transport and flow dynamics [9, 25, 91]. A related approach targets bed aggradation to reverse channel incision and recover lost floodplain storage [26, 61]. These paradigms sound distinct, but in practice most projects combine elements from several, shaped as much by site constraints and feasibility as by theory, and all modify the same geomorphic variables that control hyporheic exchange [41, 91].

Regardless of the paradigm guiding design, restoration alters hyporheic exchange through three physical pathways. First, adding or restoring channel complexity (*e.g.*, pool-riffle sequences, meander bends, large wood) intensifies the near-bed pressure variations that drive water into and out of the alluvium [11, 84]. Second, widening the active channel and reconnecting it to its floodplain wets more streambed at a given discharge, expanding the exchange interface between stream and aquifer [20]. Third, reversing past incision and promoting aggradation deepens the alluvium, increasing aquifer storage and allowing the pressure fields generated by bed topography to propagate more fully into the subsurface [78, 80]. These three pathways map directly onto the geomorphic variables that control exchange: bed topography and planform complexity, which generate the pressure gradients that drive flow into the alluvium; cross-section geometry, which governs how much streambed is wetted at a given discharge; and alluvial depth, which controls how fully those pressure gradients propagate into the subsurface.

Researchers understand the mechanisms through which restoration alters the geomorphic drivers of exchange. Yet restoration practice typically evaluates success primarily through metrics of channel morphology, riparian vegetation, and biological response, with limited attention to subsurface hydrologic outcomes [41, 91]. What is missing is not the mechanistic understanding itself but a quantitative conceptual framework for connecting specific design outcomes to their hyporheic consequences, and for evaluating how those consequences shift across the flows that matter for a project's ecological objectives.

Knowledge Gaps and Research Objectives

The disconnect between hyporheic process research and restoration practice reflects three specific gaps in the current literature, each of which this dissertation addresses.

The first is methodological. The analytical solutions described in Section 1 offer a low-cost, physically grounded approach to aquifer characterization, but they have been developed and validated only for daily temperature signals in vertical streambed flow paths. Restoration monitoring programs routinely collect temperature records from floodplain wells over annual cycles. Whether the same analytical framework can extract reliable aquifer properties from these records, where flow paths span tens to hundreds of meters and lateral heat losses may violate the one-dimensional assumption, has not been tested. Establishing the conditions under which the approach holds and where it breaks down would give practitioners a foundation for interpreting the temperature data they already collect.

The second concerns magnitude. Systematic quantification of how restoration changes the total volume of water cycling through the subsurface across a range of flows remains limited. Earlier we described two physical pathways through which restoration increases exchange: expanding the wetted area and intensifying pressure gradients. These two mechanisms respond differently to discharge, yet their relative contributions have not been separated. Without that separation, a practitioner who measures increased exchange after a restoration cannot distinguish how much of the gain came from wetting more streambed versus driving water into the alluvium more intensely, or anticipate how that balance shifts across the hydrograph.

The third concerns which design outcomes produce the observed gains. A typical restoration simultaneously adds channel complexity, expands the wetted area, and deepens the alluvium, and as described earlier, each alters exchange through a different physical pathway. But current approaches for evaluating restoration effectiveness provide no way to separate these contributions. That a restoration increased total exchange reveals nothing about which design outcome was responsible, whether a different combination would have produced a larger or more persistent effect, or how the attribution changes with discharge. Partitioning the restoration effect among its constituent mechanisms would let practitioners evaluate which outcomes matter most, under what flow conditions, and begin to connect design decisions to hyporheic results.

Research Approach

We address these knowledge gaps through three studies that share a common field site, a common modeling platform, and a common analytical question: how does restoration change hyporheic exchange, and through what physical mechanisms?

All three studies draw on data collected at Meacham Creek, a salmon-bearing tributary to the Umatilla River in northeastern Oregon where the Confederated Tribes of the Umatilla Indian Reservation completed a 1.6 km floodplain and channel restoration in 2011. Monitoring wells installed throughout the floodplain at the time of restoration recorded five years of temperature and water table elevation in the alluvial aquifer. The temperature records motivated and informed the analytical work in Chapter 1; the water table records provided observational constraints for the numerical models in Chapters 2 and 3.

Chapter 1 extends temperature-based analytical methods from vertical streambed flow paths to horizontal floodplain flow paths. Using heuristic simulation experiments in HydroGeoSphere, we evaluate whether inverse solutions of the one-dimensional advection-diffusion equation can reliably estimate hydraulic conductivity and dispersivity from damping and lagging of annual temperature signals as water traverses floodplain aquifers. The experiments reveal a proximal zone near the channel where longitudinal advection dominates and estimates are reliable, and a distal zone where vertical heat exchange with the atmosphere and bedrock degrades those estimates. The proximal zone concept provides practical guidance for monitoring design and establishes the conditions under which annual temperature signals can characterize floodplain aquifer properties. The simulation framework developed here also provides the foundation for the coupled surface-subsurface models used in Chapters 2 and 3.

Chapter 2 uses the Meacham Creek restoration as a natural experiment to quantify how restoration changes hyporheic exchange across the hydrograph. We model restored and unrestored channel configurations across four flow conditions and five alluvial depths, using the water table observations to constrain modeled hydraulic response. A multiplicative decomposition of aquifer discharge, $Q_{\uparrow} = A\, q_{\uparrow}$, separates the restoration effect into contributions from expanded wetted area and intensified specific discharge. Here $Q_{\uparrow}$ [$\mathrm{m^3\,s^{-1}}$] is total aquifer discharge, A [$\mathrm{m^2}$] is the wetted area through which stream and aquifer exchange water, and $q_{\uparrow}$ [$\mathrm{m\,s^{-1}}$] is the specific discharge. The decomposition reveals that area expansion consistently accounts for the largest share. Two geomorphic constraints emerge, each subject to diminishing returns: an area limit governed by channel cross-section shape and its expression through at-a-station hydraulic geometry, and a gradient limit set by the depth of alluvium above bedrock, which determines how fully the geomorphic pressure field develops as subsurface hydraulic gradients. Their interaction through Darcy's law produces the strongest restoration effect at intermediate flows. The chapter leaves one question open: the decomposition separates area from gradient but does not identify which design elements produce the flux differences between channels.

Chapter 3 addresses the question Chapter 2 leaves open: what produces the flux differences between channels? We develop a semi-empirical model that predicts specific discharge from aquifer storage and geomorphic state, then multiplies by wetted area to yield total aquifer discharge. Because the model preserves the Darcy structure of $Q_{\uparrow} = A\, q_{\uparrow}$, its fitted coefficients map to physical mechanisms, and the resulting partitioning traces to processes rather than statistical artifacts. The partitioning attributes the restoration effect to three factors: expanded wetted area, the morphological changes that intensify near-bed pressure gradients, and the gain in alluvial depth that allows those gradients to develop more fully. Their relative contributions shift systematically across the hydrograph. Wetted area accounts for the largest share at every flow. The morphological contribution peaks at intermediate flows where near-bed pressure variations are strongest, and diminishes at overbank flows as submergence dampens them. Alluvial depth plays a supporting but persistent role. The partitioning framework offers practitioners a way to evaluate which restoration outcomes yield the largest hyporheic returns at the flows that matter for a given project's ecological objectives.

Together, the three chapters trace an arc from method development through effect quantification to effect attribution, building a foundation that connects hyporheic process research to restoration practice.

CHARACTERIZING FLOODPLAIN AQUIFER PROPERTIES FROM ANNUAL TEMPERATURE SIGNALS

Introduction

Hyporheic exchange in coarse-grained floodplain aquifers of montane drainages shapes stream temperature, nutrient cycling, and aquatic habitat by routing channel water through subsurface flow paths that extend tens to hundreds of meters laterally and span months of residence time [6, 63]. Quantifying the magnitude and timing of this exchange requires three-dimensional hydraulic models, which in turn require estimates of the aquifer's hydrologic properties—hydraulic conductivity, dispersivity, and storage. Two approaches dominate. Inverse modeling with tools such as PEST becomes computationally expensive at the spatial scales of these aquifers, and calibrated parameters often lack independent empirical support. Artificial tracers released in the channel can travel flow paths too long to be recovered before they are lost to long residence times or lateral dispersion [37]. Natural tracers avoid both limitations and may provide a practical alternative for floodplain aquifers at this scale.

Temperature serves as a well-documented natural hydrologic tracer in aquifers [2, 75, 76]. Paired temperature sensors along vertical flow paths through the streambed record how the surface signal damps and lags as water infiltrates, yielding estimates of streambed seepage rates [18, 39, 40, 52]. The method relies on inverse solutions of the one-dimensional advection-dispersion equation (1D ADE) for heat with a periodic boundary condition [50]. Early analyses used plots and look-up tables to solve the equation [73]. Hatch [39] derived analytical solutions, and Luce *et al.* [52] and McCallum [59] later published closed-form variants that recover aquifer properties directly from amplitude and phase without iterative calibration.

Analytical solutions of the 1D ADE have typically been applied to phase lagging and amplitude damping in daily-period temperature cycles, which penetrate tenths of meters to meters vertically into the streambed [40, 45, 47]. Similar to daily temperature cycles, annual-period temperature cycles from the floodplain hyporheic zone [6, 63] exhibit phase lagging and amplitude damping, but penetrate tens to hundreds of meters horizontally into the aquifer. Five years of recent annual temperature records measured in 17 wells installed to record annual temperature in the floodplain of Meacham Creek (Figure 1), a tributary to the Umatilla River, exhibited similar phase lagging and amplitude damping in temperature variation at seasonal time scales as observed in daily records. Whether the same signal-processing approach can extract aquifer properties from annual-period cycles in floodplain aquifers has not been tested.

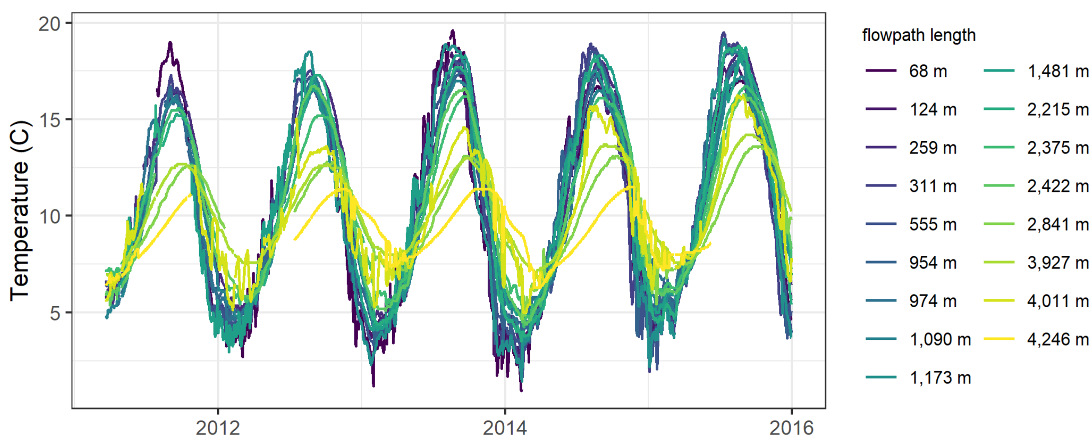

Figure 1: Floodplain aquifer temperature records measured between 2011 and 2016 in 17 wells installed in the Meacham Creek floodplain upstream, within, and downstream of the restoration site. Color encodes flow-path length from the stream channel to each well, ranging from 68 m (dark) to 4,246 m (light).

Whether considering annual or daily temperature signal frequency, inverse modeling of the 1D ADE with a cyclical temperature boundary hinges on two assumptions: (1) steady, unidirectional advective flux of heat and water, and (2) a sinusoidal temperature signal [46]. Violations of these assumptions produce systematic errors in parameter estimates, and those errors have been well characterized for the daily-period streambed application. At the daily scale, numerical simulations show that misalignment between a vertical sensor array and the direction of water flow inflates errors in fitted water velocity; the error grows with the misalignment angle [46]. Uncertainty in material-property estimates or instrument spacing can also yield substantial error in fitted water flux [72]. A non-stationary signal mean can bias fitted water flux and thermal diffusivity as well [69].

The same 1D ADE assumptions face different vulnerabilities at the annual scale. An annual temperature signal spreads over a 10 to 100 m flow path, producing a smaller longitudinal gradient than a daily signal. The smaller gradient leaves the aquifer's energy balance more exposed to heat exchange with the overlying unsaturated zone and the underlying bedrock. Both exchanges are vertical, violating the 1D assumption.

Here, we present a series of heuristic simulation modeling experiments that derive estimates of aquifer properties from inverse modeling of the 1D ADE applied to annual temperature signals observed in flow paths of tens to hundreds of meters in length. Our first goal is to demonstrate that aquifer hydraulic properties (e.g., hydraulic conductivity or hydrodynamic dispersion) can be successfully estimated from inverse modeling of annual temperature signals under ideal conditions that conform to the assumptions of the 1D ADE. Our second goal is to examine how such estimates are influenced by violations of underlying assumptions of the 1D ADE. In doing so, we aim to identify flow-path length scales that satisfy the assumptions of the 1D ADE. Within those scales, damping and lagging of annual temperature signals along the flow path carry the information needed to estimate aquifer hydraulic properties.

Methods

We tested whether the 1D advection-dispersion equation can recover known aquifer properties from annual-period temperature signals along horizontal flow paths. The test uses synthetic temperature records generated by a 3D heat-transport model (HydroGeoSphere) configured with prescribed aquifer properties, then fits the 1D ADE to those records and

Table 1: Physical constants used to represent aquifer properties in the alluvial aquifer for the analytical and numerical model aquifers.

Variable	Value
Thermal conductivity, sediment (W m^{-1} °C^{-1})	8.37
Thermal conductivity, water (W m^{-1} °C^{-1})	0.598
Specific heat, sediment (J kg^{-1} °C^{-1})	840
Specific heat, water (J kg^{-1} °C^{-1})	4186
Density, sediment (kg m^{-3})	2650
Density, water (kg m^{-3})	1000
Porosity (n)	0.25
Water surface slope	0.01
Shape parameter (α)	2.20
Shape parameter (β)	1.72
Residual soil saturation (Θ)	0.33

compares the estimated properties against the prescribed values.

Applying the 1D ADE in a horizontal reference frame carries over the assumptions of its more familiar vertical-frame application [18, 39, 73, 77]: water and heat move in one dimension along the flow path, inputs to the flow path follow a sinusoidal temperature cycle, and subsurface water velocity is constant. The two frames differ in scale and period. The vertical frame treats water and heat moving through the streambed at scales of 0.1 to 1 m and resolves daily cycles [52, 77]. The horizontal frame treats down-valley flow at scales of 1 to 100 m and resolves annual cycles.

A Synthetic Aquifer Temperature Data Set

The validation required synthetic temperature records from a hypothetical aquifer with known properties. The records had to span horizontal flow paths under both "ideal" conditions that conform to 1D ADE assumptions and "non-ideal" conditions that violate them.

HGS is a finite-element modeling environment that couples surface and subsurface water flow with heat and solute transport [4].

We used HGS to create dynamic temperature profiles along an aquifer flow path and across seasons for three different sets of assumptions about the aquifer structure, which differed in their representation of heat exchange between the subsurface flow path and lateral sources or sinks of heat:

- "U" scenarios represent ideal conditions consistent with 1D ADE assumptions, having an (U)pstream sinusoidal temperature and constant head hydrologic boundaries at the upstream and downstream ends of the flow path;
- "UB" scenarios represent non-ideal conditions with the same boundaries as the (U)pstream scenarios, but with underlying (B)edrock that absorbs and releases heat, causing vertical heat flux between the bedrock and flow path;
- "UBS" scenarios represent the non-ideal conditions of the UB scenario, but with an additional (S)urface temperature boundary representing heat exchange between the flow path and the overlying unsaturated sediments, which are in turn subject to heating and cooling from the atmosphere.

We used each of these three structural assumptions (boundary configuration) to run the model assuming two different values of hydraulic conductivity, 100 $\mathrm{m\,d^{-1}}$ (K100) and 400 $\mathrm{m\,d^{-1}}$ (K400), for a total of 6 model scenarios: U:K100, UB:K100, UBS:K100, U:K400, UB:K400, and UBS:K400.

Scenarios – Aquifer structure

HGS simulates heat flow within a three-dimensional mesh of model nodes. We created a high aspect ratio (long, thin, and narrow) mesh representing the domain influencing the heat transport of a flow path through the Meacham Creek, OR alluvial aquifer. Under the U scenarios, the mesh was 5 m deep $\times$ 2 m wide $\times$ 1000 m long and parameterized to represent porous media. The model mesh was discretized at 1 m spacing in all three dimensions.

In both the UB and UBS scenarios, the mesh was extended downward by 25 m to incorporate subtending bedrock at the same 1 m vertical spacing.

In the UBS scenario, a dynamic specified temperature boundary ran the length of the mesh to simulate the effects of seasonal warming and cooling of the aquifer via the atmosphere.

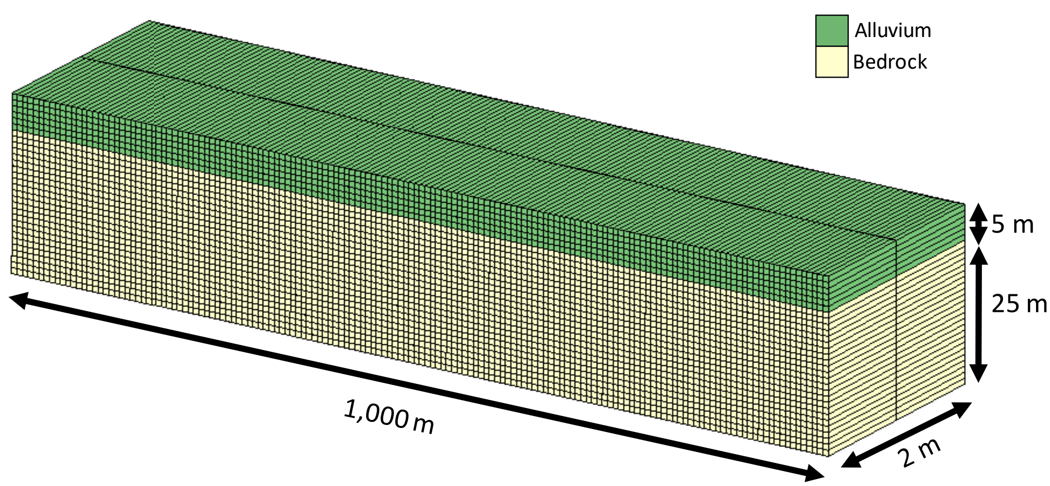

Figure 2: A schematic illustration of the model domain used for the analysis. Length is reduced and width is exaggerated to emphasize detail.

Scenarios – Parameterization

We selected physical parameters for the model (Table 1) to be representative of the geological and climatic setting of the Umatilla River basin. Thermal properties of Columbia River basalt, appropriate for both the porous media and bedrock, were based on findings presented by Burns [21]. HGS incorporates unsaturated sediment properties into solutions for flow

Table 2: Atmospheric inputs held constant across all scenarios in the HGS simulations. Air temperature varies seasonally and is specified in §2.

Variable	Value
Air density (kg m^{-3})	1.2
Air pressure (Pa)	1.013×10^{5}
Specific heat of air (J kg^{-1} K^{-1})	7.17×10^{2}
Specific humidity (kg kg^{-1})	1.062×10^{-2}
relative humidity	0.75
wind speed (m s^{-1})	1.0
latent heat of vaporization (J kg^{-1})	2.258×10^{6}
Soil-water suction at surface (m)	0.138
incoming shortwave radiation (W m^{-2})	1.10×10^{2}
Incoming longwave radiation (W m^{-2})	3.0×10^{2}
Drag coefficient	2.0×10^{-3}
Cloud cover	0.5

and thermal flux in the unsaturated zone of the porous media using the Van-Genuchten relationships [86], with our model parameters based on estimates for coarse, sandy-gravel-cobble substrate of alluvial floodplains similar to Meacham Creek from a sprinkler experiment performed in a floodplain along the Boise River in the Snake River Plain [79]. Atmospheric conditions at the floodplain surface drive the heat flux into the subsurface. We held these conditions constant across scenarios so that subsurface structure remained the only control on the annual temperature signal (Table 2). Air temperature is the only atmospheric driver that varies seasonally; we specify it as a daily time series in §2.

Scenarios – Boundary Driving Variables

Specified head boundaries at the upstream and downstream ends of the flow path maintained a water table elevation of 1 m below the upper surface of the model domain, leaving a 1 m thick volume to represent unsaturated sediment above the water table. A specified temperature boundary at the upstream end of the model imposed the stream's annual thermal regime on the porous media domain. Direct stream-temperature measurements in Meacham Creek covered only summers between 2011 and 2016, with one or two loggers spanning full annual cycles. We synthesized a continuous six-year record by regressing the logger data against concurrent air temperature from the Union Pacific Railroad Bonfer weather station (UP211), then applying the regression to the air-temperature record. The boundary used the mean daily stream temperature for each Julian day of the year, averaged across 2011–2016.

For the UBS scenarios, an additional boundary condition prescribed atmospheric forcing at the floodplain surface. The air-temperature component of that forcing used the mean daily air temperature for each Julian day, averaged across the 2011–2016 record from the same weather station. The other atmospheric inputs (incoming radiation, humidity, wind, etc.) were held at the constant values in Table 2.

Scenarios – Initialization

For every model scenario, initial conditions consisted of groundwater head set to equal the elevation of the model surface, and temperature throughout the porous media was set to 10.5°C, the mean value of the temperature records depicted in Fig. 1. We ran the model for five years, and considered the first three years to be model "spin-up." We verified that the model reached a cyclic steady-state by comparing temperatures between simulation years 4 and 5. For each observation point and day of the year, we calculated the root mean squared difference (RMSD) between year 4 and year 5. Because the driving variables repeated on a 365-day cycle, a negligible RMSD confirmed that the spin-up period was sufficient and any artifacts of the initial conditions had washed out of the system.

Scenarios – Visualization of HGS results

To avoid splitting the 12-month cycles arbitrarily in our visualizations, we plotted the last 18 months of simulated temperature from each model scenario. We generated plots of at-a-site temperature time series, arrayed along the x-dimension of the model. The sampling locations were 2.5 m below the model surface, placing them 1.5 m below the water table. Sites were spaced every 10 m from x = 0 through x = 100 m, and every 100 m from x = 100 through x = 1000 m along the flow path. Each scenario therefore yielded 20 temperature time series, spaced at increasing distances from the upstream boundary along the flow path.

We also made longitudinal contour plots along the model's centerline (the x,z plane at y = 1 m, half the 2 m transverse extent). Each contour plot depicted groundwater temperature throughout the alluvial portion of the model domain on the last day of the simulation.

Numerical Basis for inverse modeling of the 1D ADE

Using the HGS model output from each scenario as a synthetic data set (i.e., a surrogate for field data), we used inverse modeling to estimate hydraulic conductivity and effective thermal diffusivity of the simulated aquifer by fitting the 1D ADE to the synthetic data, once for each of the six scenarios. We present our approach to inverse modeling, below, using the notation of Luce *et al.* [52], but use x (rather than z) to represent distance along an aquifer flow path to denote our focus on horizontal flow through the floodplain aquifer rather than vertical flow through the streambed.

Our approach uses the conventional governing partial differential equation (PDE) to model subsurface water temperature (T, °C) along a flow path. Heat flux through the porous medium is often modeled as the combination of conduction and convection [10, 51, 52]. The governing equation is based on conservation of energy where the volumetric change in thermal energy stored is composed of the divergences of the conductive and advective fluxes [10, 51, 52]:

$$\frac{\partial T}{\partial t} = \kappa_e \frac{\partial^2 T}{\partial x^2} - v_t \frac{\partial T}{\partial x}. \tag{1}$$

v_t is related to the specific discharge (q, m s^{-1}) and is expressed as:

$$v_t = q \frac{\rho_w c_w}{\rho_m c_m}, \tag{2}$$

where ρ (kg m^{-3}) is the bulk density and c (J kg^{-1} °C^{-1}) is the specific heat of the porous medium (m) and water (w). Porosity does not appear explicitly in equation 2. It enters through the bulk volumetric heat capacity $\rho_m c_m$, which combines water and solid-matrix contributions weighted by volume fraction. κ_e consists of the sum of thermal diffusivity, κ_{cond} (m^2 s^{-1}), and thermomechanical dispersion, κ_{disp} (m^2 s^{-1}):

$$\kappa_e = \kappa_{cond} + \kappa_{disp}. \tag{3}$$

κ_{cond} is a bulk material property derived from the thermal properties of the mineral and fluid components of the porous medium:

$$\kappa_{cond} = \frac{\lambda_m}{\rho_m c_m}, \tag{4}$$

where λ_m is thermal conductivity (W m^{-1} °C^{-1}) of the medium. κ_{disp} is derived from thermal dispersivity (β, m):

$$\kappa_{disp} = v_t \beta, \tag{5}$$

and is an emergent, scale-dependent system property governed by interactions between particle size distribution, stratigraphy of the porous medium, and differential flow of thermal energy along gradients through both the mineral and the fluid components of the bulk medium [8, 16, 36, 51, 67]. Thus, by substitution into equation 1, we find:

$$\frac{\partial T}{\partial t} = \left(\frac{\lambda_m}{\rho_m c_m} + q \frac{\rho_w c_w}{\rho_m c_m} \beta \right) \frac{\partial^2 T}{\partial x^2} - \left(q \frac{\rho_w c_w}{\rho_m c_m} \right) \frac{\partial T}{\partial x}. \tag{6}$$

Recasting the presentation of Luce et al. [52] in terms of annual frequency, the temperature of water entering the aquifer from the stream, $T(0, t)$, is a sinusoidal annual temperature signal of surface water:

$$T(0,t) = T_\mu + A_0 \cos(\omega(t - t_{\max})), \tag{7}$$

where T_μ is the mean periodic water temperature, A_0 is the annual temperature amplitude (°C), t_{max} (s) is the time of maximum temperature (*i.e.,* phase) in surface water, and ω is the angular frequency of the annual temperature signal (rad s^{-1}), or:

$$\omega = \frac{2\pi}{P}. \tag{8}$$

P (s) is the period of the oscillation – one year in the case of annual variations. Given this boundary condition, the PDE has a solution [39, 50, 52, 73, 87]

$$T(x,t) = T_\mu + A_0 e^{-x/x_d} \cos(\omega(t - t_{\max} - x/v_d)), \tag{9}$$

where the frequency- and velocity-dependent amplitude decay length (x_d, m) is:

$$x_d = 2\kappa_e \left(\sqrt{\frac{2}{\sqrt{v_{\mathrm{t}}^2 + (4\omega\kappa_e)^2} + v_{\mathrm{t}}^2}} - \frac{1}{v_t} \right), \tag{10}$$

and phase velocity (v_d, m s^{-1}) is

$$v_d = 2\kappa_e \left(\sqrt{\frac{2}{\sqrt{v_{\mathrm{t}}^2 + (4\omega\kappa_e)^2} - v_{\mathrm{t}}^2}} \right), \tag{11}$$

following the formulation of Vogt et al. [87] for (9), which casts the exponent describing amplitude damping as the ratio of x to x_d and phase shift term of the periodic function as x to v_d.

Inverse Solutions to Estimate Aquifer Properties

Equations for estimating aquifer properties presented by Luce et al. [52] are built upon concepts originally proposed by Stallman [73] to derive equations for direct, inverse solution to the 1D ADE using values of amplitude and phase derived from observed stream and aquifer temperature cycles. The procedure is as follows:

- Use curve fitting to estimate temperature amplitude and phase at multiple locations along a flow path.
- For each location, calculate the rate of amplitude damping and phase lagging relative to the beginning of the flow path (e.g., stream temperature).
- Calculate aquifer properties (hydraulic conductivity and effective thermal diffusivity) consistent with rate of amplitude damping normalized to phase lagging at each location.

Estimating Amplitude and Phase from Observation Temperature Records

We estimated the amplitude (A, °C) and phase (ϕ, radian) of the temperature record for each observation using linear regression. ϕ is related to the time of peak temperature observation, t_{max} (s), by:

$$\phi = \omega \, t_{max} \tag{12}$$

We fit a simple harmonic using the following trigonometric identity to linearize a cosine wave:

$$A \cos(2\pi f t - \phi) = \alpha_s \sin(2\pi f t) + \alpha_c \cos(2\pi f t), \tag{13}$$

where $\alpha_s = A\sin(\phi)$, $\alpha_c = A\cos(\phi)$, and f is signal frequency. Linear regression yields α_s and α_c, which were in turn used to solve for A and ϕ via:

$$A = \sqrt{\alpha_{\mathrm{s}}^2 + \alpha_{\mathrm{c}}^2}, \tag{14}$$

and

$$\phi = \begin{cases} \arctan(\alpha_s/\alpha_c), & \text{if } \alpha_c/A > 0, \alpha_s/A > 0; \\ \arctan(\alpha_s/\alpha_c + \pi), & \text{if } \alpha_c/A < 0, \alpha_s/A > 0; \\ \arctan(\alpha_s/\alpha_c + \pi), & \text{if } \alpha_c/A > 0, \alpha_s/A < 0; \\ \arctan(\alpha_s/\alpha_c), & \text{if } \alpha_c/A < 0, \alpha_s/A < 0. \end{cases} \tag{15}$$

Dimensionless Ratio of Amplitude and Phase

The change in temperature amplitude (A) and phase (ϕ) between two different locations along the synthetic data flow path can be expressed as the amplitude ratio ($A_{x2:x_1}$, dimensionless):

$$A_{x2:x_1} = \frac{A_{x_2}}{A_{x_1}} \tag{16}$$

and phase lag ($\Delta\phi$, radian):

$$\Delta\phi = \phi_{x_2} - \phi_{x_1}. \tag{17}$$

The annual temperature signal completes one cycle per year, so a $\Delta\phi$ of $2\pi \approx 6.28$ radians corresponds to a full year of phase lag along the flow path. In turn, η (radian^{-1}):

$$\eta = \frac{-\ln(A_{x_2:x_1})}{\Delta\phi} \tag{18}$$

expresses the logarithmic amplitude decay per radian of phase lag along the flow path. Aquifer properties follow from η as shown below.

Estimating Aquifer Properties

Given estimates of $\Delta\phi$ and $A_{x_2:x_1}$, values for v_t, q, K, κ_e, and β are derived using η. The advective thermal velocity, v_t, can be solved empirically using the following [52]:

$$v_t = \frac{\omega \Delta x}{\sqrt{\ln^2(A_{x_2:x_1} + \Delta\phi^2)}} \frac{1-\eta^2}{\sqrt{1+\eta^2}} \tag{19}$$

Once v_t is found, specific discharge, q, can be calculated using equation 2. Hydraulic conductivity then follows from q and an estimate of the longitudinal hydraulic gradient in the alluvial aquifer. In the horizontal reference frame, the water table maintains approximately constant depth below the floodplain surface, so the longitudinal valley slope approximates the hydraulic gradient:

$$K = \frac{q}{slope}. \tag{20}$$

The effective thermal diffusivity, κ_e, can be solved empirically using η and estimates of flow-path length (Δx, m; derived, *e.g.*, from a groundwater model) [52]:

$$\kappa_e = \frac{\eta \omega \Delta x^2}{\ln^2(A_{x_2:x_1}) + \Delta\phi^2}. \tag{21}$$

An empirically-derived solution for thermal dispersivity (β) for annual temperature signals can be found by rearranging 2 and assuming the effects of thermal conduction are negligible compared to mechanical dispersion along horizontal flow paths:

$$\beta = \frac{1}{v_t}\left(\kappa_e - \frac{\lambda_m}{(\rho_m c_m)}\right). \tag{22}$$

Longitudinal temperature gradients are largest near the upstream boundary and attenuate with the signal along the flow path [52]. The mechanical-dispersion contribution to κ_e therefore peaks near the inlet and weakens downstream.

Applying the fitted A and ϕ at each observation point in every scenario, we computed $A_{x_2:x_1}$, $\Delta\phi$, η, x_d, v_d, K, and β from the analytical expressions derived above.

Results

Numerical Model Initialization

For all scenarios, RMSD in temperature between model year 4 and 5 at each node on each simulation day was less than 0.01 °C (Tables 13 and 14), confirming that each simulation had reached cyclic steady state: the annual temperature signal repeated identically from year to year. The 3-year spin-up was therefore long enough to wash out initial-condition effects in each HGS simulation.

Numerical temperature solutions

Each boundary configuration produced a distinctive pattern of temperature lagging and damping along the simulated 1000 m flow path, while increasing K reduced phase lag in every configuration (Figure 3). The U scenarios showed little amplitude damping relative to the UB and UBS configurations (Figure 3), though the U:K100 scenario damped more strongly at a given distance than the U:K400 scenario. For instance, the amplitude ratio between the end and beginning of the flow path ($A_{1000:0}$) was 0.86 in the U:K100 scenario vs. 0.99 in the U:K400 scenario (Tables 15 and 16). The phase lags for the entire flow path under the U scenarios were larger than for other scenarios, and increased with decreasing K. For instance, the whole-flow-path phase lag ($\Delta\phi$) for the U:K100 scenario was 12.1 radians (Table 17) vs. 3.0 radians for the U:K400 scenario (Table 18).

The UB scenarios exhibited prominent damping in addition to lagging (Figure 3). Amplitude damping was more substantial for the UB:K100 scenario ($A_{1000:0} = 0.06$) than for the UB:K400 scenario ($A_{1000:0} = 0.5$) (Tables 15 and 16). As with the U scenarios, phase lag decreased as K increased; whole-flow-path $\Delta\phi$ was 14 radians for UB:K100, but only 3.6 radians for UB:K400 (Tables 17 and 18).

The UBS scenarios included both atmospheric temperature and bedrock boundaries, yielding patterns of $A_{x_2:x_1}$ and $\Delta\phi$ distinct from both the U and UB scenarios (Figure 3). Phase lagging exhibited by the U and UB scenarios was arrested by the addition of the atmospheric boundary. However, as in the UB scenarios, $A_{x_2:x_1}$ decreased as K increased. For instance, $A_{1000:0} = 0.57$ for the UBS:K100 scenario and 0.83 for the UBS:K400 scenario. (Tables 15 and 16). Under the UBS scenarios, troughs damped more than peaks, breaking the symmetric damping evident in the U and UB scenarios. $\Delta\phi$ was also more nuanced in the UBS scenarios, as $\Delta\phi$ exhibited asymptotic behavior with flow-path distance. For x $<$ 200 m under the UBS:K100 scenario and x $<$ 500 m for the UBS:K400 scenario, phase lag increased with distance, but plateaued and even decreased slightly thereafter (Tables 17 and

18). The plateau of phase lag indicated that temperature signals were more synchronized in the UBS scenarios than in the U or UB scenarios (Figure 3). The synchronization of annual temperature signals was especially pronounced for UBS:K400.

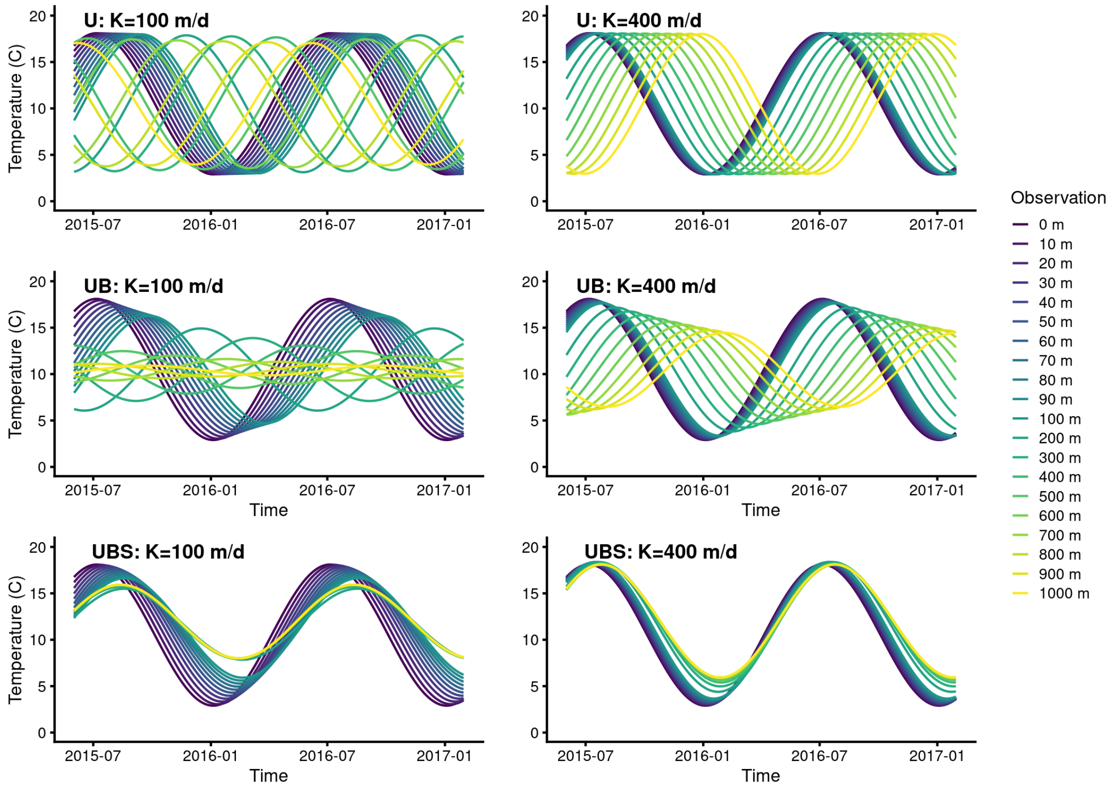

Figure 3: Annual temperature records for observation points along a 1000 m flow path, derived from HGS model scenarios. From top to bottom, the boundary configuration changes from upstream only (U) to upstream and bedrock (UB) to upstream, bedrock, and surface (UBS) boundary conditions. The left and right columns contain scenarios where hydraulic conductivity, K, was 100 and 400 m d^{-1}, respectively.

Temperature contours for summer (July 1) and winter (January 1), plotted in the longitudinal vertical (x,z) plane of the model domain, show the depth-resolved temperature distribution for each season (Figures 4 and 5). Boundary configurations determined the overall pattern of contours. Contour spacing was wider in the K400 scenarios than in the K100 scenarios in every configuration.

Under the U scenarios, heat moved only along the flow path, as the 1D ADE assumes.

Contour plots therefore showed discrete vertical temperature bands (Figure 4) that preserved the upstream temperature record.

In the UB scenarios, vertical temperature bands were present, but the longitudinal temperature gradients were less pronounced than in the U scenarios. Further, the bands had distinctive curves near the contact between the alluvial aquifer and the bedrock boundary (Figure 4). Temperature variation along the flow path was greater in the UB:K100 scenario than in the UB:K400 scenario, with more pronounced bedrock-induced curvature near the contact (Figure 4).

For the UBS:K100 scenario, the contours stood nearly vertical in the first ∼20 m along the flow path at depths of 1 to 3 m, while contours between 0 and 1 m depth curved subtly upward (Figure 4). Between 20 m and 250 m along the flow path, temperature contours were concave down. Beyond about 250 m, the temperature contours were predominantly horizontal. Contours in the UBS:K400 scenario were spaced more widely than in the UBS:K100 scenario and ran nearly vertical between 1 and 2 m depth for the first ∼20 m along the flow path. Between 0 and 1 m below the surface the contours were concave up. Beyond ∼20 m along the flow path, the temperature contours were broadly concave down up to ∼500 m, reflecting the temperature history at the beginning of the flow path. Beyond 500 m, the temperature contours transitioned to horizontal.

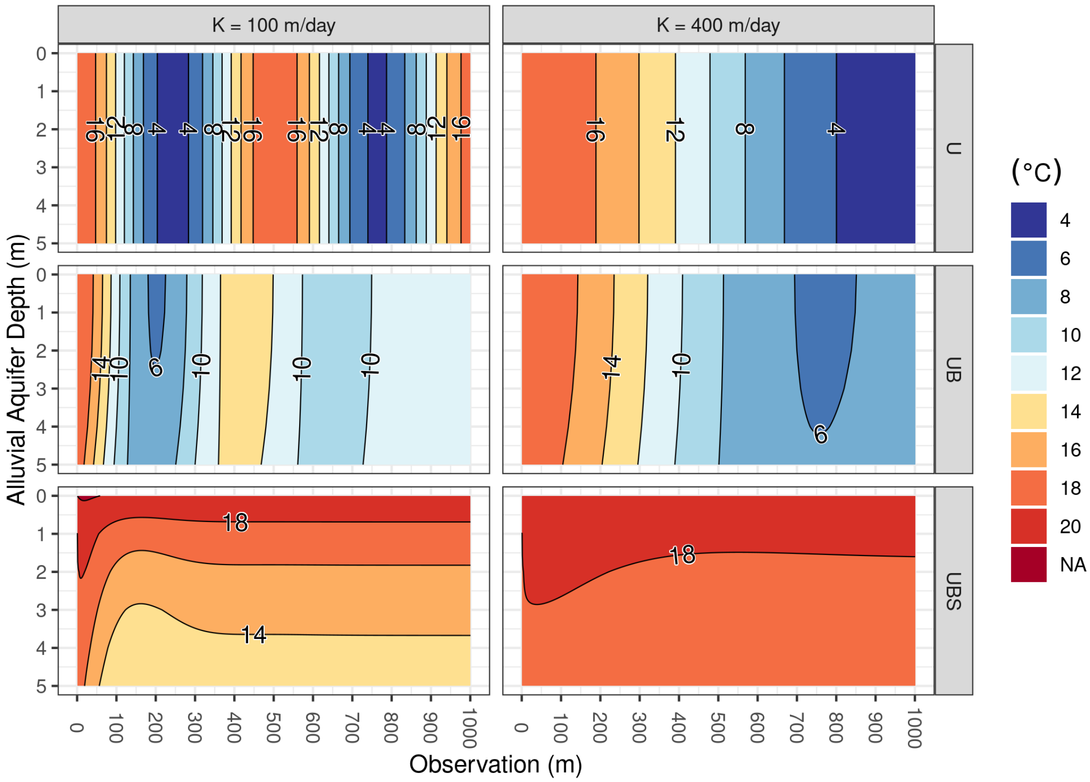

Figure 4: Modeled summer (July 1) aquifer temperatures in a longitudinal vertical profile along a subsurface flow path from 0 m to 1000 m. Rows (top to bottom) depict the U, UB, and UBS model scenarios; columns (left to right) depict hydraulic conductivity (K) of 100 and 400 m d^{-1}.

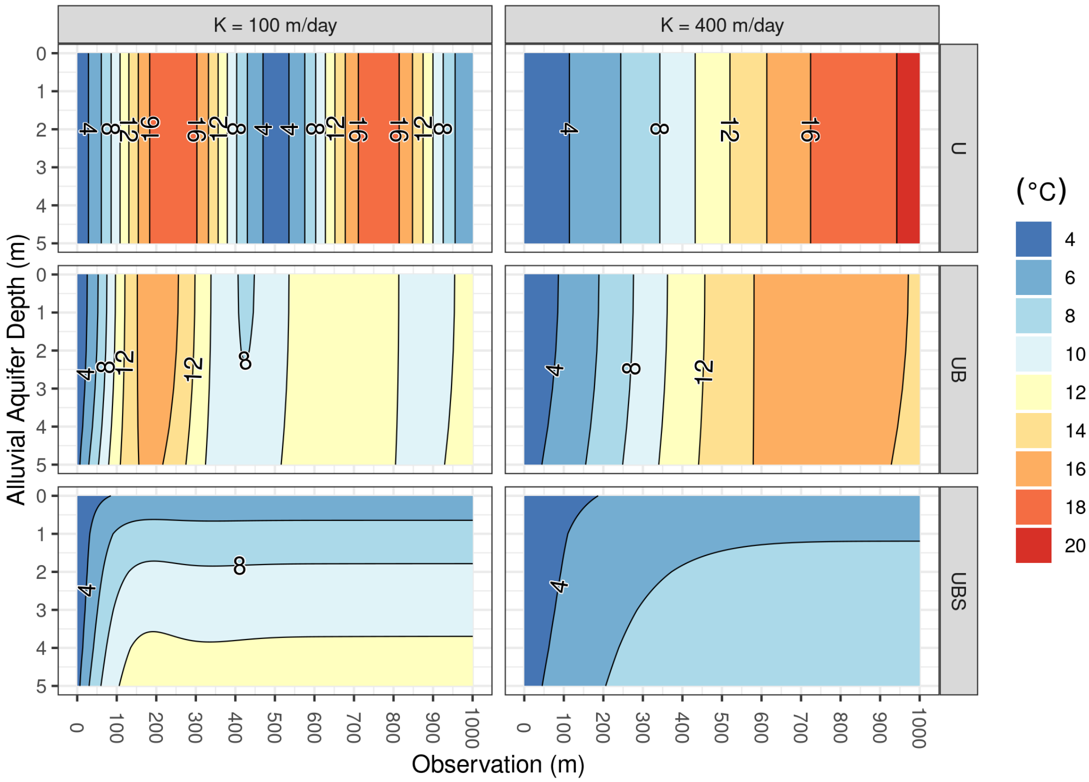

Figure 5: Modeled winter (January 1) temperatures in a longitudinal vertical profile along a subsurface flow path from 0 m to 1000 m. Rows (top to bottom) depict the U, UB, and UBS model scenarios; columns (left to right) depict hydraulic conductivity (K) of 100 and 400 m d^{-1}.

<u>Inverse Solutions – Estimates of Aquifer Properties from HGS Scenario Output</u>

As implied by Eq. 18, the assumptions of the 1D ADE yield a proportional relationship between fitted solutions of $-\ln(A_{x2:x_1})$ and $\Delta\phi$ (Figures 6 and 7). The slope of this relationship is indicative of the change in damping relative to lagging under different scenarios. The U scenario exhibited the linear relationship between $-\ln(A_{x_2:x_1})$ and $\Delta\phi$ expected under the assumptions of the 1D ADE. For the UB scenarios, the relationship was still linear, but amplitude damped more steeply per radian of phase lag than in the U scenarios. For the UBS scenarios, amplitude damped even more steeply per radian of phase lag, but the relationship was distinctly nonlinear, reflecting the asymptotic behavior of $\Delta\phi$. The range of both $-\ln(A_{x_2:x_1})$ and $\Delta\phi$ are larger for $K = 100\ \mathrm{m\,d^{-1}}$ scenarios than for $K = 400\ \mathrm{m\,d^{-1}}$.

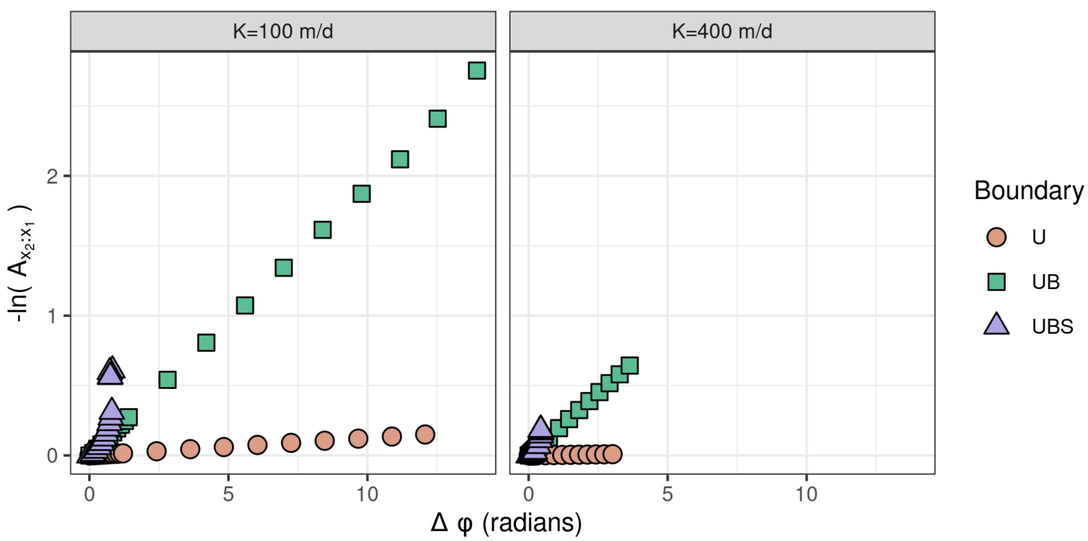

Figure 6: Negative natural log of amplitude ratio ($-\ln(A_{x_2:x_1})$) versus phase difference ($\Delta\phi$) grouped by hydraulic conductivity. The left panel shows scenarios where hydraulic conductivity, K, was set to $100\ \mathrm{m\,d^{-1}}$, while the right panel shows scenarios where K was set to $400\ \mathrm{m\,d^{-1}}$.

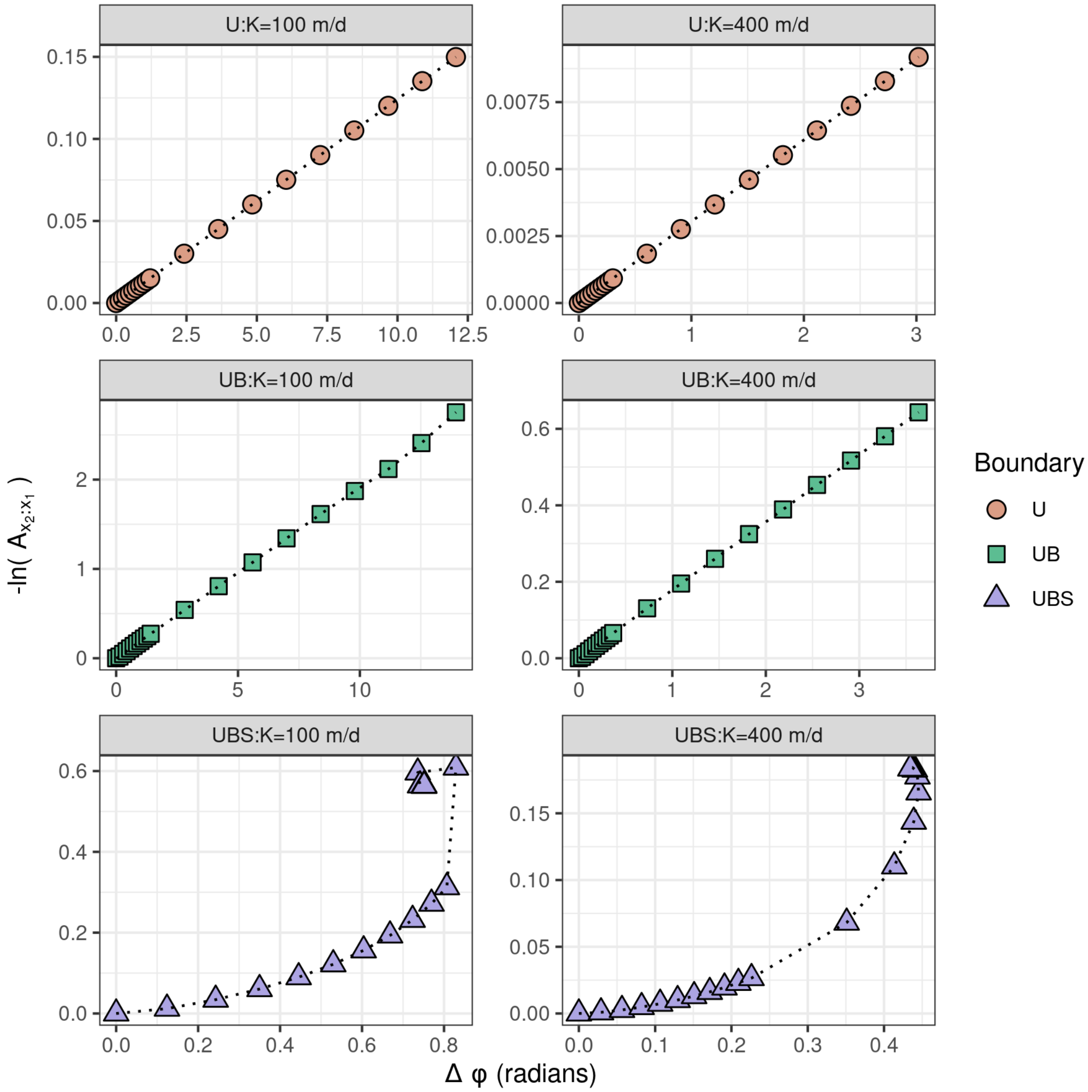

Figure 7: Negative natural log of amplitude ratio ($-\ln(A_{x_2:x_1})$) versus phase difference ($\Delta\phi$) for each scenario. The left column shows scenarios where hydraulic conductivity, K, was set to 100 $\mathrm{m\,d^{-1}}$, while the right column shows scenarios where K was set to 400 $\mathrm{m\,d^{-1}}$. The dotted line traces the trajectory of $-\ln(A_{x_2:x_1})$ versus $\Delta\phi$ with distance along the flow path.

The fitted value of η (Eq. 18), which expresses the logarithmic amplitude decay per radian of phase lag, is the intermediate quantity from which we estimated K and β. The relationship between η and observation distance was distinctive for each scenario and was a function of boundary conditions and hydraulic conductivity. As expected for the U scenarios, fitted values of η were constant, and slightly greater for the U:K100 than for U:K400 (Figure 8; Tables 19 and 20). For the UB scenarios, η rapidly increased in value between 0 and 100 m, and plateaued thereafter (Figure 8). The fitted values for η for the UB:K100 scenario were lower than for the UB:K400 scenario. For the UBS:K100 scenario, fitted values for η increased with observation distance, peaked at a value of 0.81, then decreased asymptotically to ~0.75 (Figure 8; Tables 19 and 20). For the UBS:K400 scenario, values of η asymptotically increased to ~0.42 (Figure 8; Tables 19 and 20).

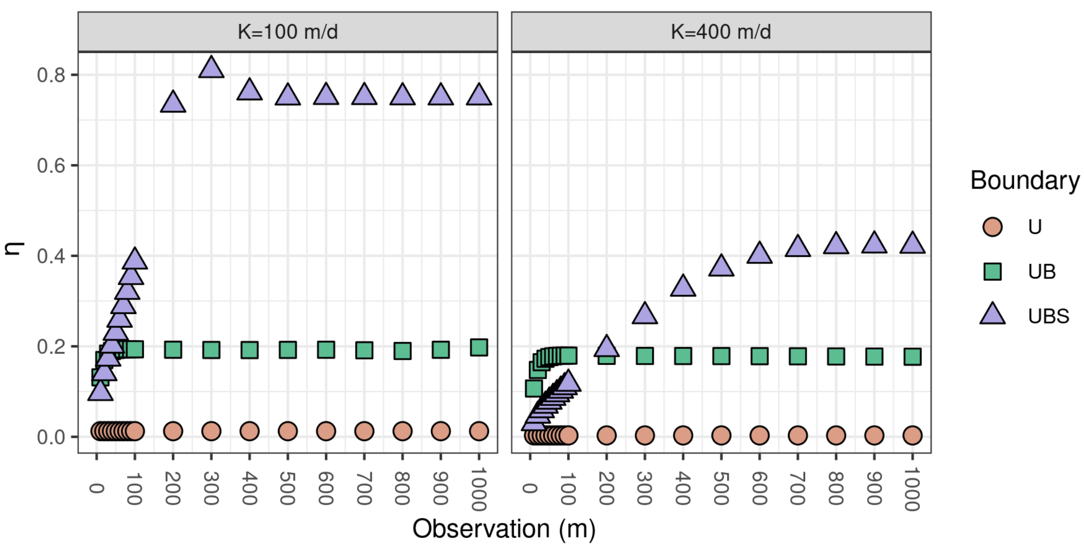

Figure 8: Plots of η versus observation location (m) grouped by hydraulic conductivity. The left column shows scenarios where hydraulic conductivity, K, was set to 100 $\mathrm{m\,d^{-1}}$, while the right column shows scenarios where K was set to 400 $\mathrm{m\,d^{-1}}$.

Fitted values for amplitude decay length (x_d) for the U scenarios were constant and adhered to the assumptions of 1D ADE (Tables 21 and 22). For the UB scenarios, x_d steadily decreased. In both the U and UB scenarios, x_d was larger at $K = 400\ \mathrm{m\,d^{-1}}$ than at $K =$

100 $\mathrm{m\,d^{-1}}$. Fitted values for x_d for the UBS:K100 scenario increased for all observations, while for the UBS:K400 scenario, x_d decreased in value up to the observation at 200 m, and increased thereafter (Tables 21 and 22).

Under the U scenarios, fitted solutions for phase velocity (v_d) were constant and adhered to the assumptions of 1D ADE (Tables 23 and 24). For the UB scenarios, v_d increased with increasing distance along the subsurface. In both the U and UB configurations, v_d was larger at $K = 400$ $\mathrm{m\,d^{-1}}$ than at $K = 100$ $\mathrm{m\,d^{-1}}$. Under the UBS:K100 scenario, v_d increased up to 100 m, decreased between the observations at 200 m and 300 m, and increased thereafter. For the UBS:K400 scenario, v_d increased between 100 m and 1000 m (Tables 23 and 24).

Fitted values of K and β for the U scenarios matched the values for K and β used in the HGS model.

Estimates of K and β derived from temperature patterns associated with the UB boundary configuration underestimated K by about 10 % for both the $K = 100$ and 400 $\mathrm{m\,d^{-1}}$ cases (Figures 9 and 10; Tables 25, 26, 27 and 28). For the UB:K100 scenarios, estimates of β were approximately 10 times greater than the expected value of β (i.e., the β parameter used in the HGS model); under the UB:K400 scenarios the estimate of β was between 30 and 50 times greater than the expected value (Figures 9 and 10; Tables 25, 26, 27 and 28).

The UBS boundary configuration yielded underestimates of K by about 10% for $x < 100$ m, but for 100 m $< x <$ 300 m, estimates of K were somewhat lower than the trend. For $x >$ 400 m estimated values of K were increasingly inflated. Estimated values of β were increasingly inflated with flow-path length in all of the UBS scenarios. For the UBS:K100 scenario at observations 100 m - 300 m, estimates of β lie above the general trend, and correspond to the peak in solutions for η (Figure 8).

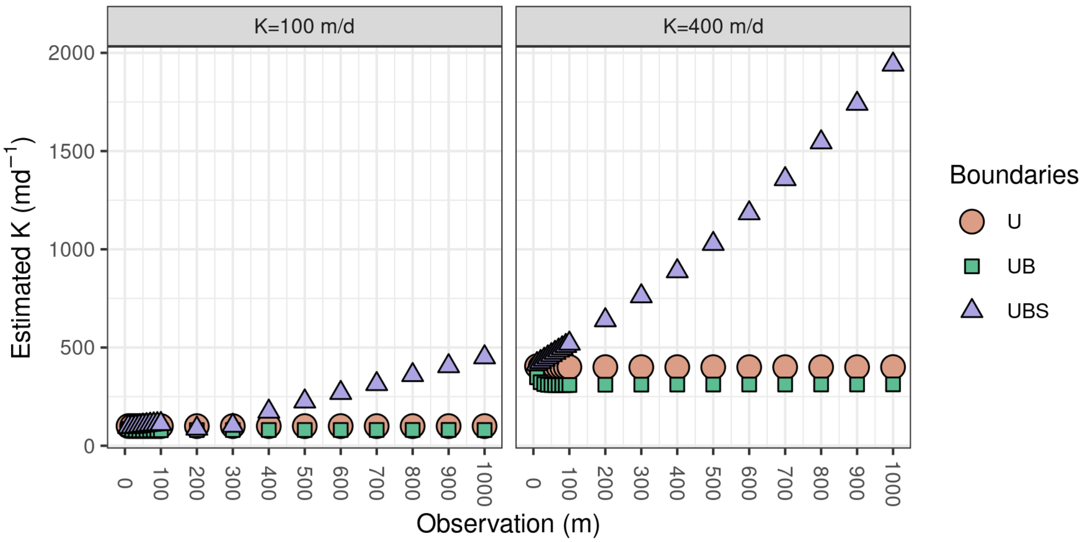

Figure 9: Estimates of hydraulic conductivity (K) from inverse modeling of temperature signals using the 1D advection-dispersion equation. The left column shows scenarios where hydraulic conductivity, K, was set to 100 m d^{-1}, while the right column shows scenarios where K was set to 400 m d^{-1}.

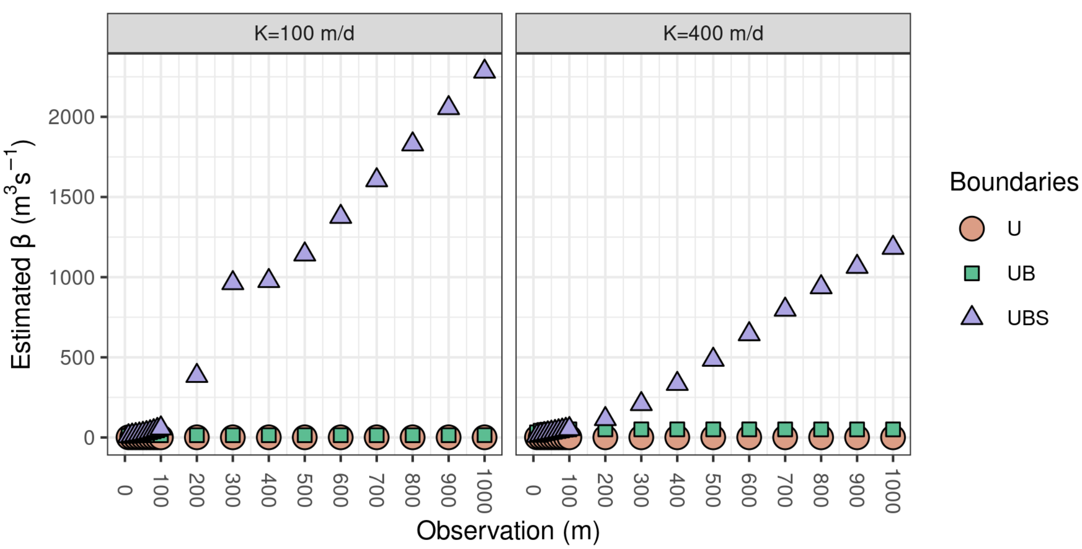

Figure 10: Estimates of dispersivity (β, in m) from inverse modeling of temperature signals using the 1D advection-dispersion equation. The left column shows scenarios where hydraulic conductivity, K, was set to 100 m d^{-1}, while the right column shows scenarios where K was set to 400 m d^{-1}.

Discussion

Under 1D assumptions with a periodic boundary, the phase shift in the temperature signal depends on distance from the boundary, the effective thermal diffusivity (κ_e), the transport velocity (v_t), and the frequency of the boundary condition [50]. Our experiments held all aquifer properties constant except hydraulic conductivity (K), which took two values: 100 $\mathrm{m\,d^{-1}}$ and 400 $\mathrm{m\,d^{-1}}$. Holding K fixed across scenarios isolates the effect of adding bedrock and atmospheric boundaries to the model (Figures 3, 4, and 5). Varying K within a scenario isolates the effect of water velocity in the aquifer.

Drivers of temperature patterns across model scenarios

The U scenarios are designed to satisfy the 1D ADE's assumptions: heat moves only along the flow path, with no heat exchanged laterally with the bedrock or atmosphere. The simulated patterns bear out that construction and serve as the baseline for the UB and UBS comparisons. The annual signal propagates downstream with little damping (Figure 3), isotherms in the longitudinal vertical profile stand vertical (Figures 4 and 5), and $-\ln(A_{x_2:x_1})$ varies linearly with $\Delta\phi$ (Figure 7), as Eq. 9 predicts.

Where hydraulic conductivity was higher, water moved faster along the flow path, and faster water carried the annual temperature signal downstream more quickly. At $K = 400$ $\mathrm{m\,d^{-1}}$ the signal traversed the 1000 m flow path in a quarter of the time it took at $K = 100$ $\mathrm{m\,d^{-1}}$. Faster advection left shallower longitudinal temperature gradients between upstream and downstream observation points. Thermal dispersion acts continuously on whatever gradient exists; where the gradient is shallower, dispersion redistributes less amplitude per unit distance. The K400 scenarios therefore showed less amplitude damping per meter along the flow path than the K100 scenarios.

The UB scenarios add a bedrock boundary that opens a vertical heat-exchange pathway.

During warm seasons, heat leaks downward from the alluvial aquifer into the cooler bedrock; during cool seasons, the stored heat returns. The bedrock functions as a thermal reservoir, damping the annual signal along the flow path. The simulated patterns bear out this mechanism: the signal propagates downstream but damps substantially (Figure 3); isotherms stand nearly vertical but tail toward the upstream temperature boundary near the alluvium–bedrock contact (Figures 4 and 5); and $-\ln(A_{x_2:x_1})$ varies linearly with $\Delta\phi$ but on a steeper slope than in the U scenarios (Figures 6 and 7), indicating more amplitude loss per radian of phase lag.

Longitudinal dispersion cannot account for the extra damping. Thermal diffusivity was constant across all scenarios, and longitudinal temperature gradients under the UB scenarios were smaller than their U counterparts, not larger. The same diffusivity acting on a shallower gradient redistributes less amplitude per unit distance, not more. A further puzzle: heat moves vertically between alluvium and bedrock, yet isotherms stay nearly vertical rather than bowing toward the contact. The alluvium's thermal conductivity redistributes the bedrock-exchange signal upward through the 5 m saturated column faster than the annual signal propagates downstream, so the vertical profile equilibrates more quickly than the longitudinal one. That timescale ordering matters for interpreting the UBS scenarios below.

Where hydraulic conductivity was higher, faster water carried the annual signal downstream more quickly, leaving less time for the bedrock to extract amplitude at any given location. The K-effect is visible mainly in the first ~400 m of the flow path (Figure 4); beyond that, bedrock damping has pulled aquifer temperatures close to the bedrock's stable mean, and further K-driven differences in longitudinal gradient no longer register against that near-uniform background.

The UBS scenarios add an atmospheric boundary to the UB bedrock configuration. Two vertical heat-exchange pathways now act on the alluvial aquifer: downward into the cooler bedrock, upward into the seasonally warming and cooling unsaturated zone above. As water travels downstream, it is exchanging heat vertically the whole way, and aquifer temperature at a given flow-path distance reflects the accumulated influence of that vertical exchange on top of whatever stream signal remains. The simulated patterns bear this out: the annual signal propagates downstream with substantial damping over the first $\sim$100 m, then the time series from more-distal observations collapse onto one another (Figure 3); contours stand nearly vertical at the upstream end, curve as the vertical exchange accumulates, and lie horizontal far downstream where the stream signal has been fully overwritten (Figures 4 and 5); and $-\ln(A_{x_2:x_1})$ varies nonlinearly with $\Delta\phi$ (Figure 7), the asymptotic curve tracking the phase-lag ceiling that the distal zone imposes.

Where contours lie horizontal, aquifer temperature at each depth has equilibrated to a vertical profile set jointly by the atmospheric and bedrock boundaries, and the upstream stream temperature no longer registers. That does not mean longitudinal heat transport has stopped. Water is still advecting, and heat still moves with it. The longitudinal temperature gradient has collapsed to near-zero, so advective heat flux no longer produces a visible downstream signal at fixed depth. Heat has not stopped moving; the temperature field no longer records where the water started. As in the UB scenarios, longitudinal dispersion cannot account for the damping: gradients under UBS were smaller than under U or UB, and the same diffusivity acting on a still-shallower gradient redistributes still less amplitude per unit distance. Vertical exchange with both boundaries is the mechanism.

Higher hydraulic conductivity lets water carry the stream signal further downstream before vertical exchange overwrites it. Under UBS:K100, horizontal contours and superimposed time series appear beyond about 400 m; under UBS:K400, the upstream boundary's influence still reaches beyond 900 m (Figures 4 and 5). The proximal zone, where the stream signal dominates, stretches with K; the distal zone, where the vertical boundaries dominate, contracts.

Dimensions of heat flux in alluvial aquifers

The UBS contour plots reveal two zones within the floodplain aquifer, distinguished by what drives aquifer temperature (Figures 4 and 5). In the proximal zone, longitudinal advection of the stream temperature signal dominates. In the distal zone, vertical conduction of heat among the atmosphere, alluvial aquifer, and underlying bedrock dominates. A transition zone separates the two, where isotherms rotate from vertical to horizontal as the dominant driver shifts from the stream to the vertical boundaries.

In our modeling experiments, hydraulic conductivity controlled the extent of the proximal zone. At higher K (400 $\mathrm{m\,d^{-1}}$), faster water carried the stream signal further downstream before vertical exchange overwrote it, stretching the proximal zone.

In real-world floodplain aquifers, a suite of factors other than K may play a role in the extent of the proximal zone. These factors include the thickness of the alluvium, the thermal conductance of the vadose zone, and riparian shade. Alluvial aquifer thickness plays a role in vertical energy transport between the atmosphere, the porous media, and the bedrock. All other factors being equal, a thicker aquifer will have a larger proximal zone because thermal energy takes more time to make the vertical traverse of a thicker volume. The degree of saturation and properties of the vadose zone mediate vertical movement of energy as well, and a less conductive vadose zone will insulate the alluvial aquifer from the atmosphere, yielding a larger proximal zone. Similarly, riparian shade blocks direct solar radiation, and therefore slows vertical movement of thermal energy. Slower vertical thermal exchange enlarges the proximal zone. Higher hydraulic conductivity acts in the same direction by speeding longitudinal advection.

Although the UBS scenarios were driven by regionally representative parameters rather than by a Meacham-specific calibration, they generate temperature records that bear a strong resemblance to those observed in floodplain aquifers of mountain drainage basins, such as Meacham Creek (Figures 1 and 3). Temperature records from short flow paths proximate to the channel are damped and lagged, indicating the dominance of longitudinal advective energy transport, while those records from flow paths distal to the channel become more superimposed, indicating the dominance of vertical conductive energy transport. Hence, in shallow coarse-grained alluvial aquifers, vertical heat exchange with the bedrock and atmosphere grows increasingly important along the subsurface flow path away from the channel.

Implications for estimating hydraulic properties of aquifers

Whether a temperature record comes from the proximal or distal zone sets how accurately the 1D ADE recovers aquifer properties. The 1D ADE is intuitive and simple to apply, but vertical heat exchange at the boundaries degrades the accuracy of fitted estimates. Proximal-zone records therefore yield more accurate estimates than distal-zone records.

The extent to which the proximal zone penetrates the alluvial aquifer determines the rate (per unit flow distance) at which fitted estimates of aquifer properties diverge from actual values. Under the U scenarios, fitted estimates matched input values along the full flow path because no vertical-exchange pathway existed to displace the stream signal. The proximal zone was shorter and the divergence between estimated and actual aquifer properties sharper under UBS than under UB (Tables 27, 28, 25 and 26). The larger difference between input and fitted values of β compared to K was driven by the atmospheric and bedrock boundary conditions: those boundaries impose a steeper vertical thermal gradient than the longitudinal one, so vertical conduction damps the signal amplitude more than longitudinal advection does. The inversion derives κ_e, and hence β, from amplitude damping observed along the flow path; under UBS, vertical conduction dominates that damping, so the inversion absorbs vertical exchange into κ_e and β. The resulting effect is an apparent scaling of fitted estimates of K and β with observation distance from the point of infiltration (Figure 10). Under UBS:K100, fitted K does not scale monotonically with distance. Estimates dip below the trend at 100–300 m before increasing at larger distances (Figure 9), tracking a local peak in η (Figure 8). The dip marks the transition zone where vertical exchange damps amplitude faster than longitudinal advection accumulates phase lag. Although temperature signals that are damped and lagged relative to the stream may be observed in the distal zone, the signals are driven by vertical exchange of energy between the atmosphere and bedrock. Therefore, estimates derived from distal-zone temperature signals systematically overestimate aquifer properties; they reflect boundary-driven vertical exchange rather than the aquifer's intrinsic transport properties. In contrast, estimates of aquifer properties from the proximal zone will more closely match the true values, although such estimates will require careful interpretation. Ideally, temperature monitoring would occur down-gradient of the stream, close enough to the channel to stay within the proximal zone but far enough to accumulate measurable damping and lagging of the stream signal and to sample a flow-path length representative of the aquifer.

In our models, fitted values of K and β fall within an order of magnitude of the input values at observations within 100 m of the point of infiltration (Tables 25, 26, 27 and 28). In an aquifer similar to that represented by our model scenarios, more reliable locations for collecting aquifer temperature signals would be less than 100 m downstream of the stream channel, but at some minimum distance where damping and lagging are sufficient to be measurable. Importantly, vertical exchange systematically inflates fitted estimates of K and β above their true values.

The UBS scenarios incorporated atmospheric and bedrock boundaries. Their temperature signals most closely resembled field observations from mountain drainage basins. The aquifer-property estimates from these scenarios were nevertheless the least accurate of any scenario group. A two-dimensional inverse framework that represents both boundaries explicitly would improve accuracy, but at a cost. An analytical 2D solution demands additional boundary data and a tractable set of simplifying assumptions about vertical energy fluxes. A numerical 2D or 3D simulation adds the computational cost of running many forward models during inversion. Either path forfeits the 1D ADE's key appeal: recovery of hydraulic properties from two temperature signals arrayed along the aquifer's hydraulic gradient. Proximal-zone sampling keeps the 1D approach viable.

Conclusion

The 1D advection-dispersion equation, applied to heat transport, links annual temperature signals along a floodplain flow path to the aquifer's hydraulic properties. The inverse application is intuitively appealing but requires care. Temperature records must come from the region down-gradient of the channel where horizontal advection of the stream signal dominates the thermal dynamics. We call this region the aquifer's proximal zone. Beyond the proximal zone, vertical heat exchange with the atmosphere and underlying bedrock violates the 1D ADE's assumptions, so parameter estimates fitted to distal-zone records are unreliable.

Hydraulic conductivity and the water velocity it sets mediate the proximal zone's extent in our simulations. Other site attributes, including aquifer thickness and floodplain shade, likely shape the extent as well and remain as directions for future work. Bounding the proximal zone before fitting the 1D ADE is a practical prerequisite. Temperature monitoring at multiple distances from the channel offers one route to that bound. Along the flow path, fitted K estimates diverge where advective signals give way to conductive ones, and that divergence marks the proximal zone's outer edge.

Two extensions of this work warrant note. A 2D inverse framework that represents vertical heat exchange with the atmosphere and underlying bedrock could extend the approach to distal-zone records. Field validation of the proximal-zone recommendation across a wider range of aquifer thicknesses and riparian canopies would sharpen the practical guidance. Until those extensions are in place, the 1D ADE paired with proximal-zone data remains a tractable route to first-order estimates of aquifer hydraulic properties.

DECOMPOSING HYPORHEIC EXCHANGE INTO WETTED AREA AND SPECIFIC DISCHARGE

Introduction

Contemporary stream restoration paradigms emphasize designs that mimic normative physical templates for specific geomorphic settings and promote the fluvial processes that shape and maintain these features [9, 25, 91]. Form-based approaches recreate characteristic morphologies such as pool-riffle sequences, while process-based strategies encourage natural channel evolution through controlled disturbance and sediment management [26, 61, 65]. These restoration frameworks primarily target geomorphic outcomes, seeking to establish stable channel configurations that provide appropriate habitat and maintain connectivity with floodplain environments. Increasingly, restoration practitioners recognize that deliberate restoration of hyporheic processes represents a fundamental component of recovering stream ecosystem functions, rather than merely an incidental outcome of channel reconfiguration [41].

Despite growing recognition of hyporheic process importance, restoration practice remains predominantly focused on achieving geomorphic targets rather than explicitly designing for hydrologic outcomes. This emphasis persists even as a substantial body of research demonstrates how channel geomorphology drives hyporheic exchange through predictable physical mechanisms. Recent studies establish that geomorphic complexity, aquifer volume, and wetted area represent the primary interactive characteristics controlling hyporheic exchange across multiple spatial scales [11, 64, 82]. Geomorphic complexity influences exchange rates through hydrostatic and hydrodynamic head gradients created by topographic features from grain-scale roughness to reach-scale planform heterogeneity [22, 42]. Alluvial depth constrains aquifer volume and determines whether exchange processes remain confined by shallow bedrock or extend throughout deeper alluvial deposits [78, 82].

Wetted area directly controls total exchange capacity through the available interface between surface water and underlying sediments [20]. However, the translation of these research insights into restoration design and evaluation remains limited.

To bridge this gap, we built a modeling experiment that contrasts hyporheic exchange in a floodplain reach between its unrestored and restored states. We examined a reach-scale (1.6 km) river restoration project at Meacham Creek, a salmon-spawning tributary to the Umatilla River in Oregon, U.S.A. This restoration combined form-based and process-based principles to increase aquifer storage, create more sinuous and complex channel morphology, and expand wetted channel area. For each state, we tracked the total water returning to the stream from the floodplain aquifer, its vertical intensity across the streambed, and the rate at which the stored aquifer water turns over.

Beyond the two restoration states, we varied alluvial depth and stream discharge across the simulations. The depth range captures how a deeper or shallower floodplain aquifer changes the pool of water available to exchange with the stream. The discharge range traces the contrast between the unrestored and restored states from baseflow to bankfull conditions. Together, these three factors let us separate restoration effects from the effects of aquifer depth and stream flow.

Here we present an analysis demonstrating that restoration-induced changes in channel planform heterogeneity, floodplain aquifer volume, and wetted area produce measurable and predictable alterations to hyporheic hydrology in a bedrock-bounded creek draining a mountain drainage basin. These findings provide a framework for incorporating hyporheic process considerations into restoration design and evaluation, thereby strengthening the scientific foundation for ecosystem-based restoration approaches. While our analysis focuses on the Meacham Creek restoration project, we present generalized results and conclusions applicable to similar stream restoration efforts in bedrock-bounded mountain valley settings where multi-scale topographic features interact to control hyporheic exchange processes.

Methods

We used the HydroGeoSphere simulation model (HGS) [19], a 3-dimensional control-volume finite element model, to simulate hyporheic hydrology for unrestored and restored states of a 1.6 km-long Meacham Creek floodplain reach. HGS couples surface and subsurface water transport and simulated mass flux between these domains. We ran multiple scenarios of the restoration site in a factorial experimental design to simulate the effects of channel reach geomorphology, floodplain aquifer storage volume and stream discharge. We contrasted the unrestored versus restored states. All models maintained identical hydrologic boundary conditions and porous media properties (aquifer sediments). Changes in surface layer topography represented the differences in channel reach geomorphology between unrestored and restored states. From the model, we developed estimates of our response variables, $Q_{\uparrow}$, $q_{\uparrow}$, and $\bar{\tau}$ to elucidate hyporheic hydrology in an applied context.

Conceptually, we can think of aquifer storage, S, as two reservoirs stacked vertically within the aquifer. The lower reservoir, or structural storage, lies between bedrock and the streambed; its volume is set by that vertical distance. Structural storage stays saturated across every model scenario and therefore holds a fixed water volume. The upper reservoir, or dynamic storage, lies between the streambed and the floodplain surface. Dynamic storage is variably saturated with changes in river stage; its volume rises and falls with flow.

Therefore, geomorphic processes that alter alluvial depth change the volume of structural storage. Geomorphic processes that alter the stage–discharge relationship change the volume of dynamic storage. Such contrasts in alluvial volume and stage–discharge response are apparent within and between stream reaches, and across basins.

Study Area

Meacham Creek flows northward through the western Blue Mountains of north central Oregon, draining a 464-km^2 basin in the Columbia River Basalt terrane [54] before joining the Umatilla River (Fig. 11). Along its lower 25 km, the creek runs through a ribbon-like floodplain of roughly uniform width (200–300 m), bordered by steep valley walls. The floodplain consists of gravelly cobble alluvium 2–5 m deep overlying bedrock. The alluvium holds a phreatic aquifer that actively exchanges water with the creek, so the entire floodplain acts as the hyporheic zone [64].

Basin elevations range from roughly 600 m at the valley mouth to 1,280 m at the headwaters. The catchment receives 890 to 915 mm of mean annual precipitation, falling as snow at higher elevations and rain at lower elevations [3]. The largest peak flows arrive as rain-on-snow events from November through February; a secondary peak follows spring snowmelt in April. Peak discharge has exceeded 260 m^3 s^{-1}, while summer baseflow drops to 0.1 m^3 s^{-1} by August. Summer air temperatures routinely exceed 35 °C during July and August heat waves. Ponderosa pine dominates the streamside overstory. Cottonwood grows in patches near the channel, and the understory is sparse grass and scattered shrubs.

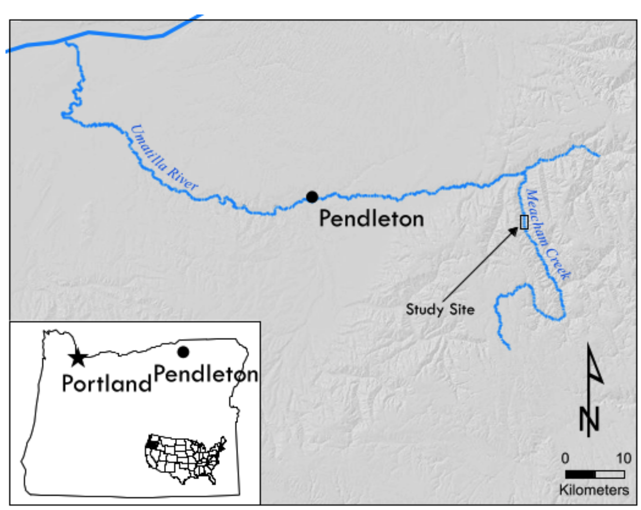

Figure 11: Location of the Meacham Creek restoration site in north-central Oregon, U.S.A.

The study reach is located approximately 8 km upstream of the confluence with the Umatilla River. The eastern edge of the floodplain is bounded by the Union Pacific Railroad and an adjacent access road. After historical high flows in 1965, the creek was confined to the western valley wall by a 4–5 m high levee, and spur dikes were constructed to deflect the creek away from the railway. In summer 2011, the Confederated Tribes of the Umatilla Indian Reservation completed a 1.6 km floodplain and channel restoration project. The restoration included removing levees and dikes, realigning the channel, adding large woody debris, and re-establishing riparian vegetation. The site has been well-studied before and after restoration, with extensive data available including: high-resolution LiDAR topography from 2009 and 2011, an as-built channel profile survey, floodplain water table elevation time series from twelve wells throughout the study area (period of record 2011–2016, see next section for details), and records from a USGS stream gaging station 6 km downstream, in continuous operation since 1975.

By 2011, the levee-confined channel had incised through the alluvium to the bedrock valley floor. A veneer of gravelly cobble covered the bed, with bedrock patches exposed between cobble. The straightened channel functioned like a flume: steep banks, a low width-to-depth ratio, and no inset floodplain to carry moderate flows. The confined plane-bed morphology reduced both profile and planform variability. As a result, the bed- and reach-scale head gradients that drive exchange were weaker in this channel than in pool-riffle or meandering channels.

The restored channel was designed from pre-1965 aerial photographs that documented the channel before levee construction. It features a sinuous, multi-threaded, pool-riffle morphology with frequent floodplain connection. Raising the streambed reduced effective bank height, increased aquifer storage capacity, and generated greater profile and planform variability. Wetted area at a given flow is greater than in the unrestored channel. Added sinuosity, bedform relief, and floodplain connection strengthened both the magnitude and variability of the hydrostatic and hydrodynamic head gradients driving hyporheic exchange.

Meacham Creek is well suited for contrasting hyporheic exchange between restored and unrestored channels at the same site. The 2011 restoration replaced the incised, levee-confined channel with a reconstructed sinuous channel in the same 1.6 km floodplain reach; the two states describe this reach before and after restoration. They differ in sinuosity, cross-section, and bedform relief across scales from individual clasts to the entire reach. Bedrock bounds the floodplain, isolating the hyporheic zone and making a mass balance of surface-subsurface exchange tractable. The LiDAR, water table, and USGS gage records allow controlled comparison while holding geologic and climatic boundary conditions fixed.

Monitoring Wells We installed 12 monitoring wells within the study area using a GeoProbe 5410 direct push drill rig mounted on a small tracked tractor. The wells were pushed to refusal, generally *ca.* 2 m – 3.5 m in depth. One-inch inside diameter PVC pipe, slotted over its full length, was installed in each boring. Each well fully penetrates the alluvium. Well position, total well pipe length, well pipe offset, and ground surface elevation were surveyed for each well. In each well, a pressure transducer suspended about 15 cm above the bottom on a nylon line recorded absolute pressure and water temperature. An on-site barometric pressure logger recorded atmospheric pressure in parallel. A depth sounder provided periodic manual water-level measurements to cross-check the transducer-derived records.

We subtracted atmospheric pressure from each absolute-pressure record using the on-site barometric logger. We then converted the resulting hydrostatic pressure to water depth above each transducer, using water density computed from the co-recorded temperature. Combining the water depths with surveyed transducer elevations produced an hourly water-table elevation record spanning early 2011 to late 2016.

Simulation Model

Model Grid We designed the model to represent the Meacham Creek floodplain stratigraphy, where a deposit of alluvium overlies the basaltic valley bottom. The model included a surface layer (overland flow domain in HGS terminology), an alluvial layer, and a bedrock layer (porous media domain components). We used the 2009 (unrestored) LiDAR DEM for the baseline model and the 2013 (restored) LiDAR DEM for the restored model surface topography. The 1 m LiDAR DEMs contain surface artifacts and small non-representative depressions that destabilize overland-flow routing. We filled the depressions with the ArcGIS "Fill" function, then smoothed the result using the ArcGIS "Focal Mean" function over a 20 m × 20 m window. The final grid retained 1 m resolution with 20× smoothed cell values. The bedrock boundary was a constant-slope surface. We set its slope to 0.01, estimated from the reach-averaged water-surface slope. Over 3.2 km, local variations wash out, so this average approximates the channel slope. We adjusted the bedrock boundary elevation to approximate a plane fitted through the depth of refusal at monitoring well locations. The model bottom extended 5 m below the bedrock. We vertically discretized the alluvium between the surface and the bedrock boundary into three stacked element layers, and represented the bedrock below as a single element layer.

The model domain extended from UTM 5,052,273.0 N to 5,055,490 N, creating a total valley length of 3,217 m. The floodplain width varied from 250 m to 300 m throughout the domain. The domain encompassed the 1.6 km-long restoration project area (5,053,200 N to 5,055,000 N), with 490 m and 927 m buffers at the upstream and downstream model boundaries. We meshed the domain in plan view as a regular 5 m × 5 m grid clipped to the floodplain outline (Figure 12). The grid extended vertically through the three alluvium element layers and the single bedrock layer.

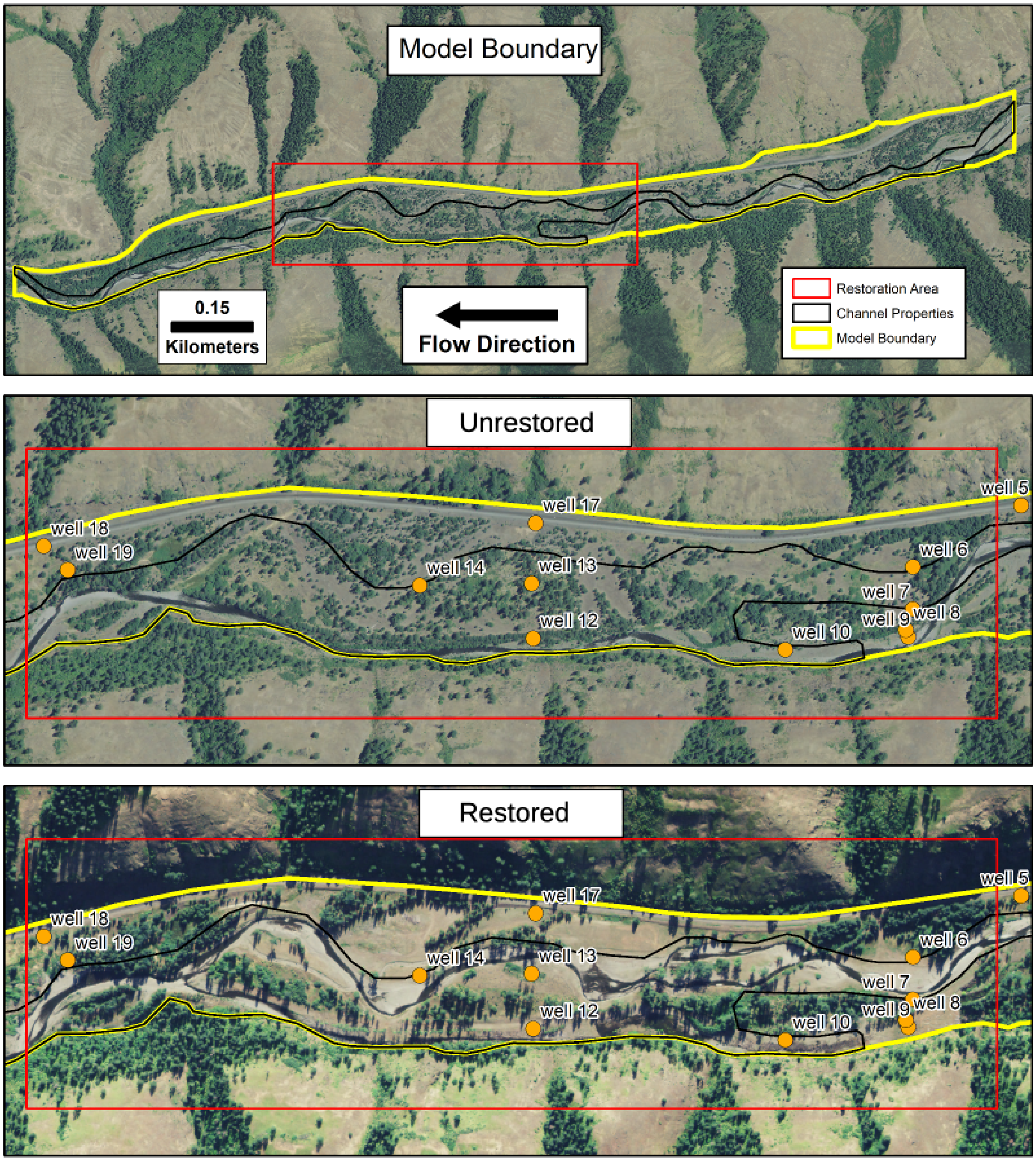

Figure 12: Meacham Creek study area. The three panels show the same 1.6 km floodplain reach. The top panel shows the full HGS model domain, with the restoration project area outlined. The middle and bottom panels show the pre-restoration (unrestored) and post-restoration (restored) channel, respectively. Orange dots mark monitoring well locations.

Material Properties We set hydraulic conductivity (K) of the alluvium to 400 m d^{-1}, a bulk value for the Umatilla River [63] that reflects preferential flow through coarse alluvium. For the massive basalt bedrock, we set K to 0.00273 m d^{-1} (Table 3) based on findings from Zakharova (2012) [93]. We divided the overland flow domain into a stream channel zone and a floodplain zone, each with its own parameters. The stream channel zone spans the channel migration zones of both the unrestored and restored configurations (Figure 12). In the stream channel, we used a Manning's roughness coefficient of 0.043, measured on the Grande Ronde River at La Grande, Oregon [7], a similar stream 30 km east of Meacham Creek. We held Manning's roughness constant across both configurations; the single value represents reach-scale bulk friction and does not resolve pool-riffle variation. Rill height represents the height of surface-flow obstructions such as cobbles or vegetation. We selected values representative of large gravel and small cobbles in the Meacham Creek channel. We set the surface-subsurface coupling length to the value from the Abdul example problem in the HGS manual. The coupling length controls the rate at which water exchanges between the overland-flow and porous-media domains. For the floodplain zone, we based all values on the Abdul example problem (HGS Verification Manual). Tables 3 and 4 summarize the material properties.

Table 3: Material properties for the alluvium and bedrock.

Variable	Value	Units
Alluvium		
Hydraulic conductivity, alluvium (K)	400	m d^{-1}
Porosity, alluvium (ϕ)	0.25	–
longitudinal dispersivity (β)	1.0	m
Shape parameter (α)	2.20	–
Shape parameter (β)	1.72	–
Residual soil saturation (θ)	0.33	–
Bedrock		
Hydraulic conductivity, bedrock (K)	0.00273	m d^{-1}
Porosity, bedrock (ϕ)	0.04	–
longitudinal dispersivity (β)	10^{-20}	m

Table 4: Material properties for the surface domain.

Variable	Value	Units
Manning's roughness, channel	0.043	s $m^{-1/3}$
Rill storage height, channel	0.015	m
Manning's roughness, floodplain	0.3	s $m^{-1/3}$
Rill storage height, floodplain	0.002	m
Coupling length	0.1	m

Boundary Conditions

We ran each experimental scenario as a steady-flow simulation: upstream and downstream boundary conditions were held constant, and the flow field ran to equilibrium. We imposed specified-head boundaries on the porous-media domain at the upstream and downstream ends of the floodplain, using the water table elevations derived in the Driving Hydrology section below. We delivered stream discharge at a single "flux nodal" node in the stream channel of the overland-flow domain, approximately 5 m downstream of the upstream model boundary (HGS Reference Manual, p. 156, [5]). A critical-depth boundary governed discharge at the downstream end of the overland-flow domain (HGS Reference Manual, p. 174, [5]). Critical depth is the minimum-specific-energy depth for open-channel flow; specific energy is the sum of kinetic and potential energy per unit weight of water, measured relative to the channel bottom. Lateral no-flow boundaries followed the floodplain outline at the alluvium–basalt contact. The bottom no-flow boundary lay 5 m below the alluvium–bedrock contact, within the bedrock layer; because bedrock hydraulic conductivity is negligible, this placement does not materially affect flow in the alluvium.

Experimental Design

We used HGS to run a factorial experiment of steady-flow simulation scenarios varying restoration state (unrestored vs. restored topography), minimum aquifer storage, and stream discharge. Unrestored and restored restoration states differed only in the surface-layer topography of each model, taken from the unrestored and restored LiDAR DEMs, respectively. All other model parameters were identical across corresponding scenarios.

In the factorial design, we considered:

- two restoration states, unrestored and restored, differing in channel position, planform, and the area wetted at any given flow;
- four stream discharge rates (Q, [$\mathrm{m^3 s^{-1}}$]): baseflow, the annual flood, the bankfull flood, and an overbank flood;
- five minimum aquifer storage volumes (S), set by varying alluvial thickness (see Aquifer Storage below).

The full factorial yielded 40 steady-flow scenarios: two restoration states $\times$ four discharges $\times$ five storage volumes.

<u>Driving Hydrology</u> To investigate the effect of stream discharge, we modeled four steady stream flows. Baseflow was a typical summer low flow observed in the field. The three flood magnitudes came from recurrence-interval analysis of annual peak-flow records at the USGS Meacham Creek at Gibbon, OR gage (14020300; 1975–2024). We selected $Q_{1.5}$, Q_2, and Q_5, which we label the annual, bankfull, and overbank floods respectively (Table 5). These labels are convenient shorthand for flows of a given recurrence interval, not strict definitions based on channel geometry. We developed the recurrence-interval analysis using USGS PeakFQ software (https://rconnect.usgs.gov/peakfq/), which implements Bulletin 17C [32] with regional skew values from USGS Scientific Investigations Report 2016-5118 [58]. We assigned one of these four flows to the upstream flux nodal boundary in each experimental scenario.

We determined water table elevation at the upstream and downstream specified head boundaries using a power-law fit to an empirical water table–discharge relationship. We built this relationship from mean daily water table elevation in Well 8 and mean daily stream discharge at the USGS Meacham Creek gage. Well 8 was located in the floodplain approximately 3 m west of the channel at the upstream end of the restored reach. We expressed water table elevation relative to bedrock at the well, calculated as the difference between water surface elevation in the well and bedrock elevation at the well location (see Monitoring Wells section for details). From the water table–discharge relationship, we estimated water table elevation at the upstream and downstream ends of the model domain for each of the four steady stream flows.

Flow Name	Discharge (m^3s^{-1})
Baseflow	0.31
Annual Flood	22.0
Bankfull Flood	71.9
Overbank Flood	112.0

Table 5: Steady stream flows modeled in HGS.

Aquifer Storage Aquifer discharge ($Q_{\uparrow}$), aquifer storage (S), and mean turnover time ($\bar{\tau}$) are linked by the identity $Q_{\uparrow} = S/\bar{\tau}$ (Section 3 gives the formal definitions). If $\bar{\tau}$ were constant, larger S would produce larger $Q_{\uparrow}$. However, a larger aquifer should be associated with longer $\bar{\tau}$. Therefore, to assess the interactive effects of changes in S and associated changes in $\bar{\tau}$ on $Q_{\uparrow}$, we incorporated a simple experiment into our study design. We decreased the elevation of the bedrock relative to the floodplain surface. In a general way, this simulates the effect of thicker alluvium at the site.

We made five floodplain storage scenarios by lowering the bedrock boundary of existing conditions in 1 m increments for both the unrestored and restored topography (Table 6 for a listing of S at baseflow for each scenario).

Depth Decrement (m)	Unrestored Aquifer Storage (m^3)	Restored Aquifer Storage (m^3)
0	328,479	400,970
1	436,952	515,347
2	555,864	625,942
3	684,991	736,690
4	803,500	846,490

Table 6: Meacham Creek floodplain aquifer storage volumes modeled in HGS.

Verification

Confidence in our simulation model's ability to approximate the potential effects of restoration-induced geomorphic changes on hyporheic hydrology depends on the model's accurate representation of Meacham Creek's surface and subsurface hydrology.

To assess model performance, we compared modeled outputs against two sets of field observations. In the channel, we compared modeled stream stage at the gage location against observed stage–discharge records from the USGS Meacham Creek stream gage. In the floodplain, we compared modeled water table elevation at each well location against observed water table–discharge records from wells on the Meacham Creek floodplain (Figure 12). Both comparisons used the 0 m bedrock decrement scenario under restored conditions at each of the four steady stream flows.

Initialization

We ran a separate 365-day transient spin-up for each experimental scenario. The spin-up used the same specified-head and flux-nodal boundary conditions as the scenario itself, at the scenario's assigned stream discharge. The initial head field was set equal to the ground surface elevation at every node, an HGS convenience option for a fully saturated starting state. The head field at the end of the spin-up served as the initial condition for the corresponding steady-flow simulation.

Model Analysis

Model Output We used saturation and head derived from HGS output files. We also applied the HGS function "Nodal fluid mass balance from shp file" (hereafter, the mass-balance function) to retrieve fluid mass balance within a polygon bounding the restoration project area (5,053,200 N to 5,055,000 N) (See Figure 12). This command generated a mass balance summary for each model layer, including horizontal flow in/out, vertical flow in/out, and total fluid volume. The uppermost layer in the model was a dual domain layer representing both the overland flow domain (the streambed) and the top of the porous media domain (the floodplain aquifer). The water balance for this layer was reported in two parts: surface water and upper aquifer. Twelve observation points were specified in the model domain corresponding to the location and depth of monitoring wells in the project area (Figure 12). Each observation point recorded modeled head. All analyses were performed using R Statistical Software [66] and the tidyverse packages [90].

Model Water Balance HGS automatically writes the model water balance to a dedicated output file, along with an estimate of the fluid mass balance error. The percent fluid balance error quantifies the discrepancy between water sources/sinks and storage changes in a model. It is calculated using the absolute difference between NET1 (rate of water entering/leaving the overland flow and porous media domains through sources and sinks, $\pm Q$ $[L^3T^{-1}]$) and NET2 (rate of change in storage for all model domains, ΔS $[L^3T^{-1}]$). The absolute error is simply:

$$\text{Absolute Error} = (\text{NET1} - \text{NET2})$$

The percent error provides a normalized measure expressed as:

$$\text{Percent Error} = \frac{\text{abs}(\text{NET1} - \text{NET2})}{\max\{\text{NET1}(+), \text{abs}(\text{NET1}(-))\}} \times 100.0\%$$

This calculation divides the absolute difference by the maximum of either positive NET1 contributions or the absolute value of negative NET1 contributions, then multiplies by 100 to express the result as a percentage. Across all 40 experimental scenarios, the water balance closed to within 0.001% of the flow through the system.

Aquifer Discharge, Specific Discharge, and Turnover Rate Total aquifer discharge ($Q_\uparrow$) is the reach-scale sum of upward flow from the floodplain aquifer to the stream channel. For each scenario, we computed $Q_\uparrow$ as the vertical flow-out component of the overland flow domain, extracted using the mass-balance function.

Wetted area (A) is the total top-layer footprint where saturation equals one. We calculated A by counting saturated top-layer nodes and multiplying by each node's 25 m^2 area. We did not label nodes as streambed or floodplain; those terms describe where saturation occurs at different flows. At baseflow, saturated nodes fall within the stream channel. At higher flows, overbank inundation wets additional nodes on the floodplain surface. We then calculated specific discharge ($q_\uparrow$) as:

$$q_\uparrow = Q_\uparrow / A \tag{23}$$

Aquifer storage (S) has two common meanings: the storage capacity of the saturated medium, and the total fluid volume of the porous medium. We use the latter throughout this work. For each scenario, we extracted S as the total fluid volume summed across all porous-media layers of the study area, using the mass-balance function. Because HGS solves the Richards equation, S includes both saturated storage and water held in the unsaturated zone above the water table. The floodplain aquifer is dominantly saturated, so unsaturated contributions to S are small.

We calculated mean turnover rate [s^{-1}] as a measure of exchange efficiency. Mean turnover rate is the inverse of mean turnover time ($\bar{\tau}$). We calculated $\bar{\tau}$ as:

$$\bar{\tau} = \frac{S}{Q_{\uparrow}} \tag{24}$$

We defined mean turnover rate as:

$$\frac{1}{\bar{\tau}} = \frac{Q_{\uparrow}}{S} \tag{25}$$

Mean turnover rate thus represented the fraction of S exchanged by $Q_{\uparrow}$ per unit time.

Results

Model Verification Simulated water table elevation rose with discharge in every monitoring well, though agreement with observed values varied across flow conditions (Figure 13). At baseflow, simulated and observed water table elevations closely matched in all monitoring wells. In 8 of 12 wells, however, model accuracy declined at higher flows.

The lower-than-observed water table elevations in most wells at higher flows likely resulted from the model's under-prediction of river stage at high flows. The model does not account for increased form drag as point bar vegetation, large wood, and other roughness elements on the floodplain are inundated. These features would slow flow velocity and increase stage relative to our simplified channel representation. That said, the model did exhibit a realistic water table response to temporal variation in stream stage. Since the purpose of this study is to evaluate relative relationships between geomorphic change and hyporheic response, we deemed the model sufficient for our purpose.

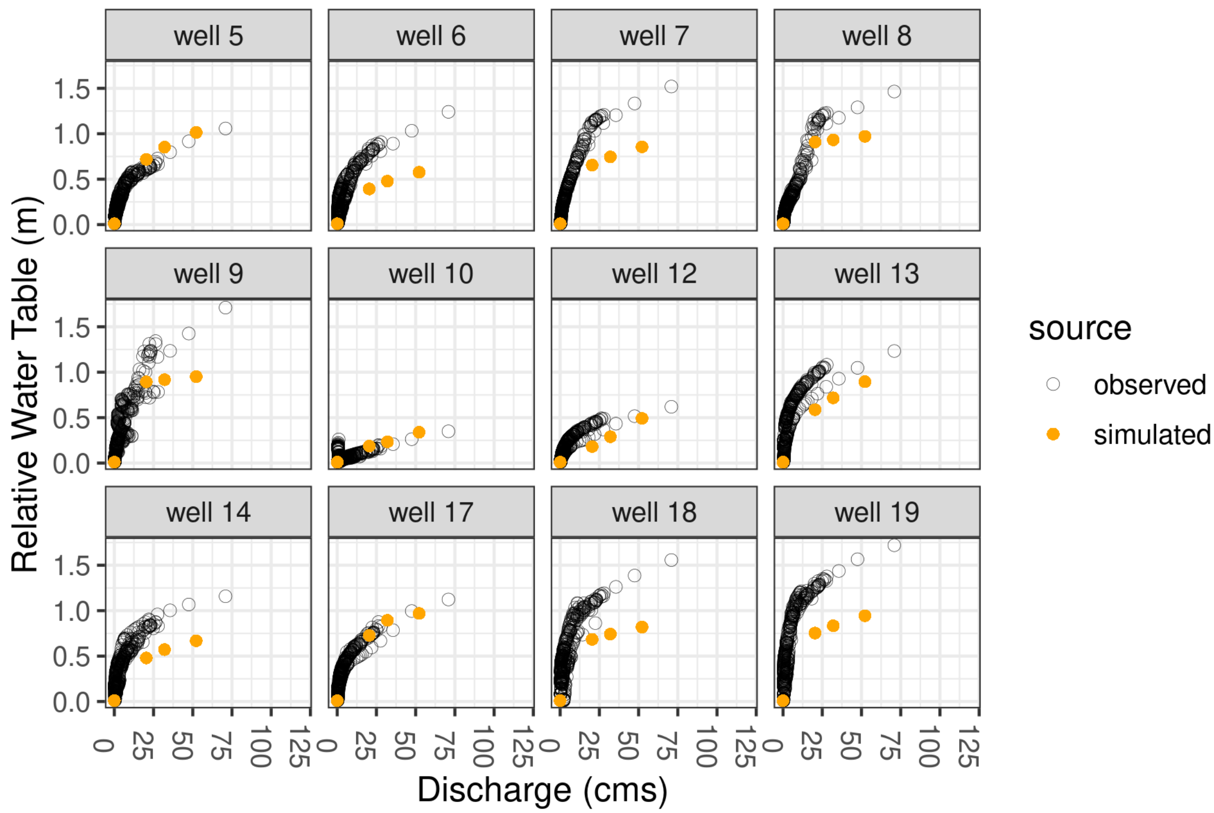

Figure 13: Observed and simulated water table at twelve wells in the Meacham Creek study area, plotted against stream discharge. For each well, water table is referenced to its lowest observed value, so all panels share a common vertical scale. Observations span 2011–2016.

Restoration Effects on Wetted Area, Specific Discharge, Aquifer Discharge, and Turnover Rate The unrestored channel has a confined, trapezoidal, plane-bed form. The restored channel is wider and has an unconfined pool-riffle form with shoaling point bars. Wetted area (A) was greater in the restored channel at every flow (Figure 15). In both channels, A increased with stream discharge, but the rate of increase differed. In the unrestored channel, A grew at a roughly uniform rate across all flows. In the restored channel, small increases in stream stage yielded disproportionately large increases in A, especially between baseflow and the annual flood.

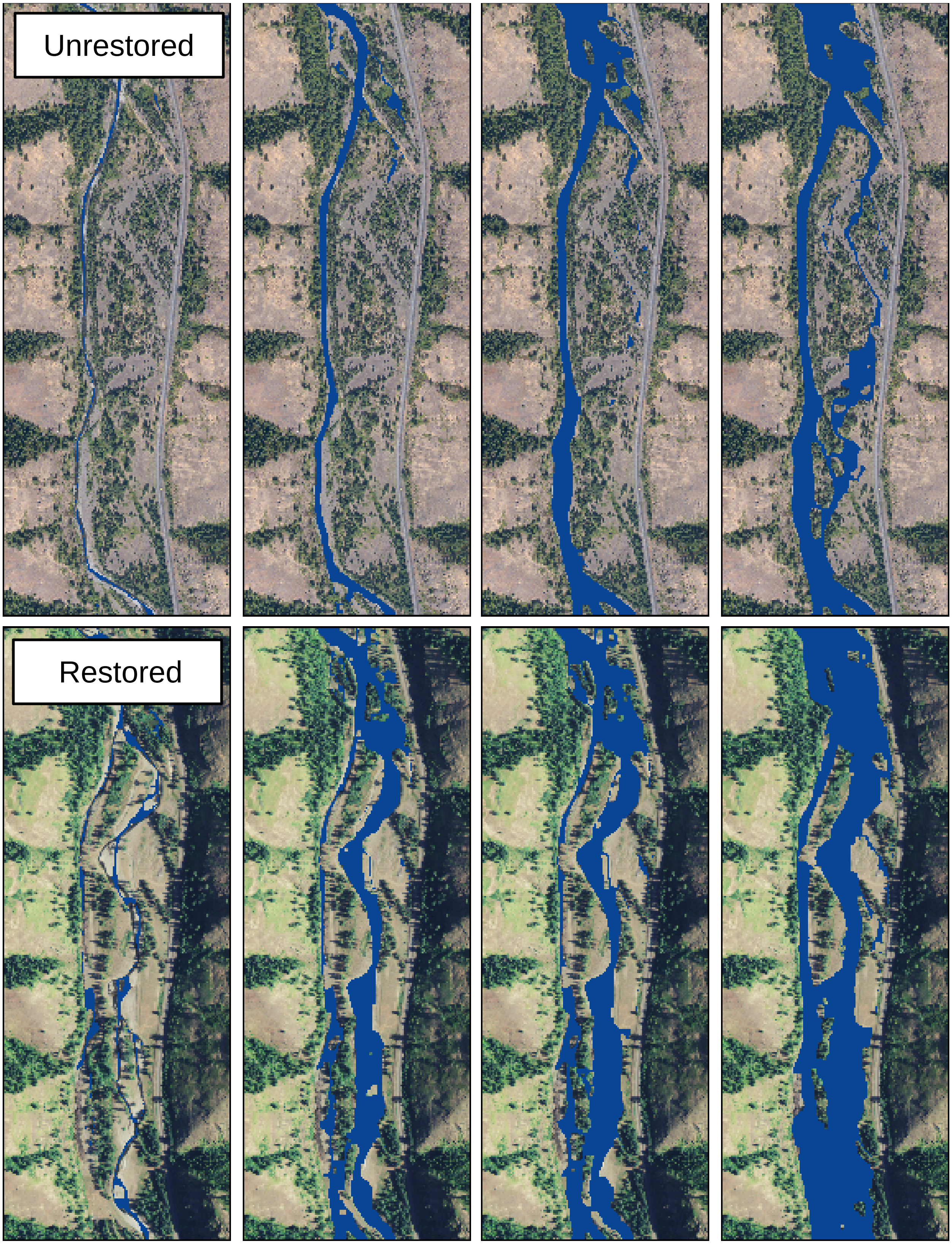

Figure 14: Modeled wetted area by flood magnitude for the unrestored and restored scenarios.

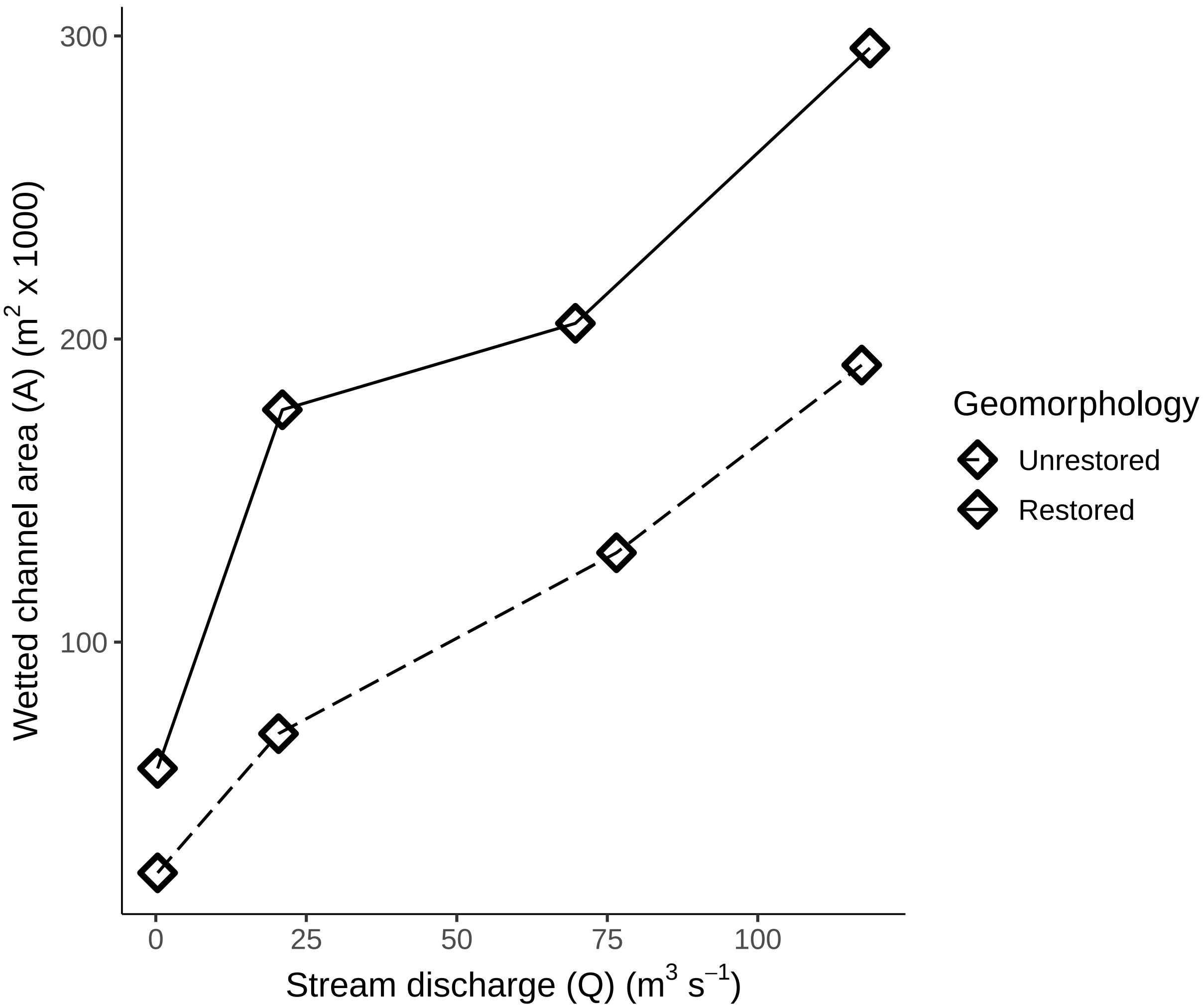

Figure 15: Modeled wetted area by flood magnitude for the unrestored and restored scenarios.

<u>Restoration Effects on Specific Discharge</u> Each curve plots $q_{\uparrow}$ against aquifer storage for a single combination of restoration state and Q (Figure 16). Within a curve, points move rightward as S_{lower} grows with deeper alluvium (bedrock-depth decrements of 0.0 to 2.0 m). Higher Q shifts entire curves rightward by raising stream stage and S_{upper}.

Across all scenarios, $q_{\uparrow}$ increased non-linearly with S. The downward bend in the curves showed that, as S increased, the influence of S on hyporheic exchange became less pronounced.

$q_{\uparrow}$ peaked at baseflow in the restored channel, and so did its sensitivity to S (the slope of each curve). The unrestored channel was less responsive in both respects.

Mean $q_{\uparrow}$ for intermediate flows (annual flood and bankfull) was similar across restoration states. $q_{\uparrow}$ dropped substantially from baseflow to intermediate flows in both channels. By Darcy's law, $q_{\uparrow}$ equals streambed hydraulic conductivity times vertical hydraulic gradient (VHG), and conductivity was held constant across scenarios. Streambed VHG therefore tracked $q_{\uparrow}$: higher in the restored channel at baseflow, and lower at intermediate flows in both channels.

At overbank flow, $q_{\uparrow}$ in the restored channel continued to drop from its bankfull value. $q_{\uparrow}$ in the unrestored channel rose, reversing its within-bank decline. Overbank $q_{\uparrow}$ values were therefore comparable across restoration states. Because conductivity was held constant, floodplain VHG at overbank flow was substantially higher in the unrestored channel than in the restored channel.

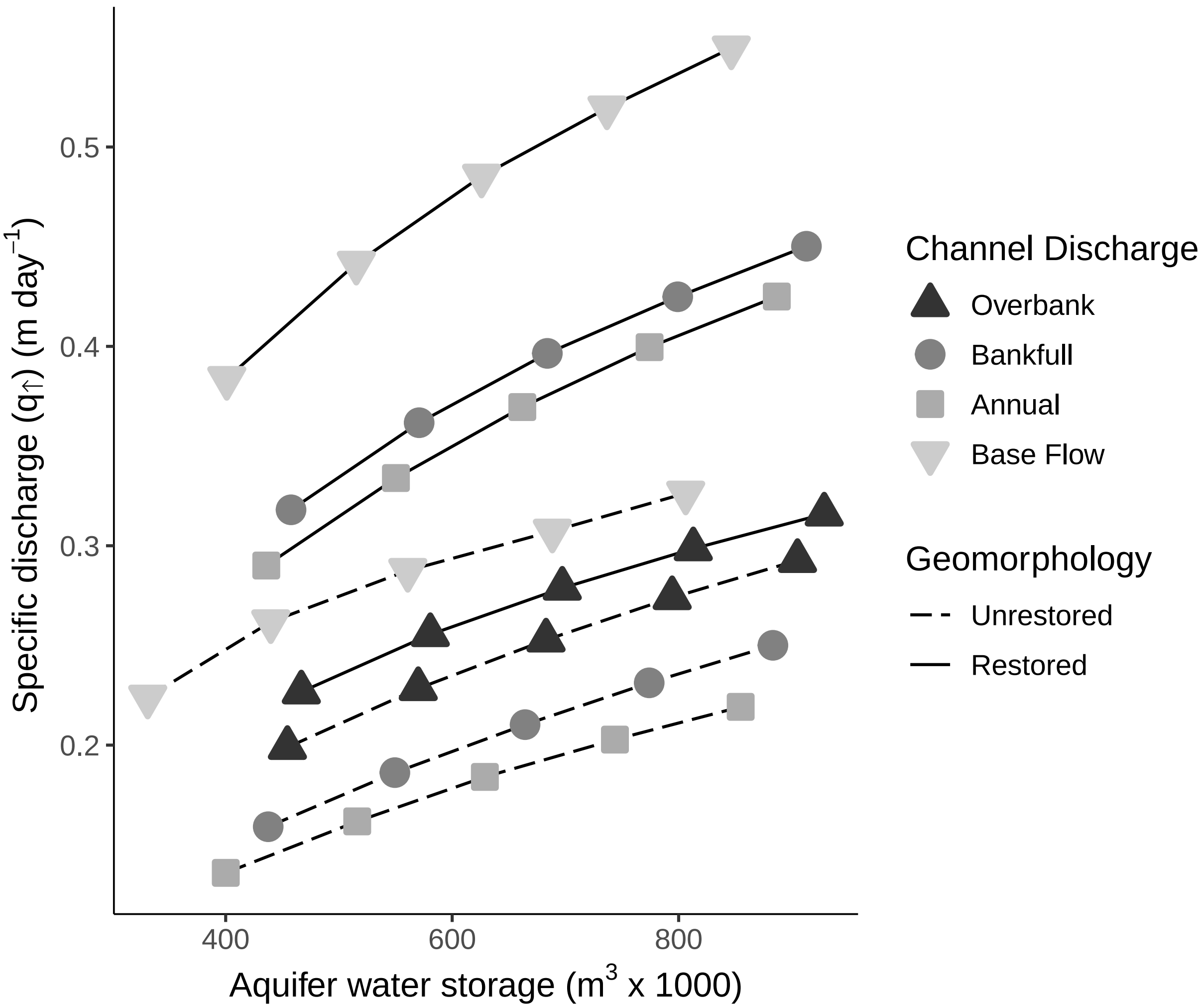

Figure 16: Specific discharge ($q_{\uparrow}$) versus aquifer storage (S) for unrestored and restored states for each stream discharge. Points represent model outputs; lines connection results for different values of aquifer storage between otherwise identical model scenarios.

Restoration Effects on Aquifer Discharge Multiplying $q_{\uparrow}$ by wetted area gives total aquifer discharge, $Q_{\uparrow} = A\, q_{\uparrow}$ (Figure 14). As with $q_{\uparrow}$, $Q_{\uparrow}$ increased with aquifer S for both the restored and unrestored states (Figure 17). The slope of $Q_{\uparrow}$ versus S was greater at higher discharge and in the restored channel. In contrast to $q_{\uparrow}$, however, $Q_{\uparrow}$ was strictly increasing with channel Q; the associated increase in floodplain wetted area A offset any reductions in $q_{\uparrow}$.

$Q_{\uparrow}$ increased with Q in both channels, but the increments between flow states were not evenly spaced. In the unrestored channel, $Q_{\uparrow}$ rose modestly from base to annual flow, more from annual to bankfull, and most from bankfull to overbank. The restored channel showed the opposite pattern: $Q_{\uparrow}$ rose sharply from base to annual flow and then changed little through bankfull and overbank. Wetted area A followed the same ordering. For instance, the unrestored channel gained little A from base to annual flow, while the restored channel gained substantial A over the same step.

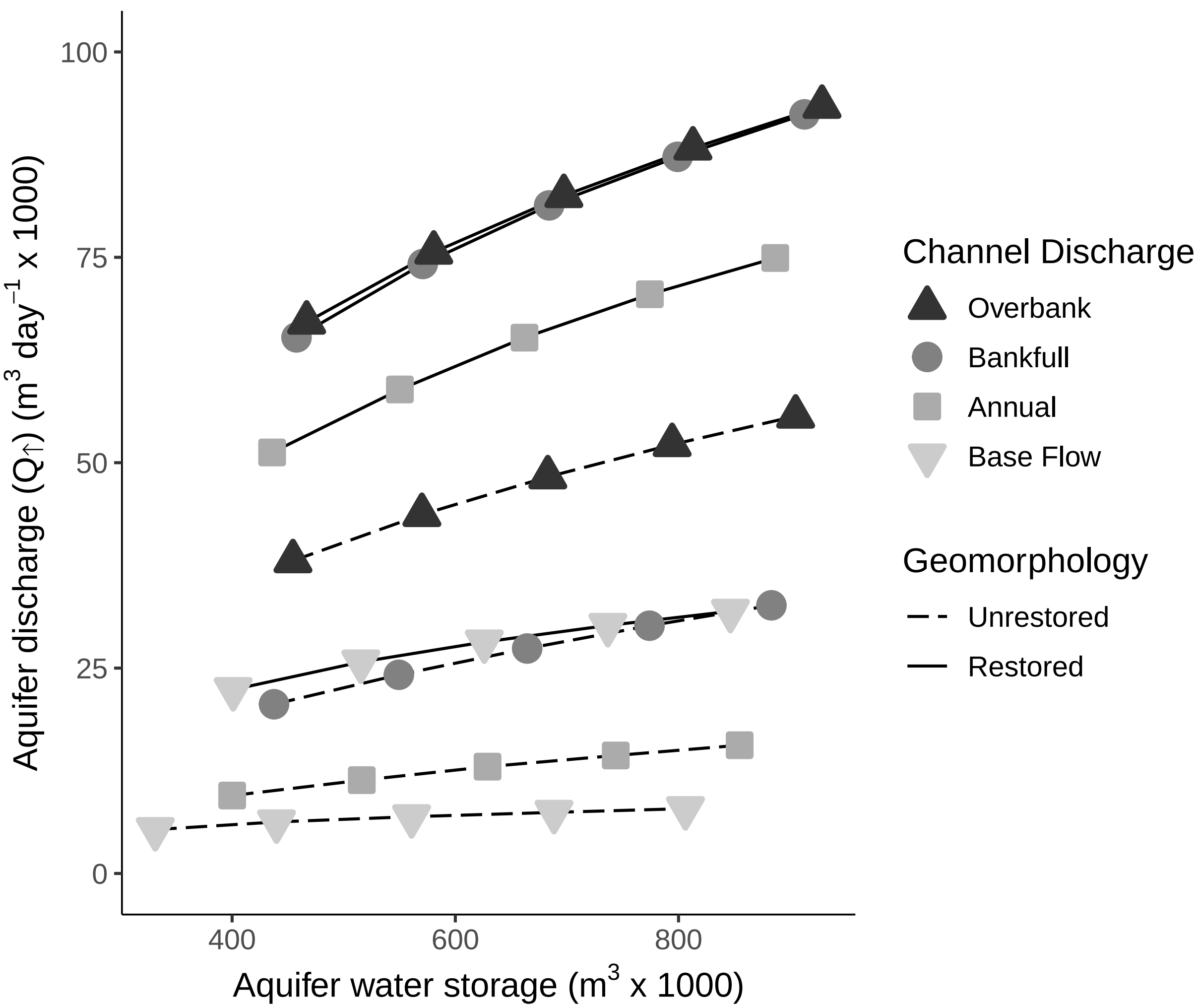

Figure 17: Aquifer discharge ($Q_{\uparrow}$) versus aquifer storage (S) for unrestored and restored states for each stream discharge. Points represent model outputs; lines connect data for different aquifer sizes among otherwise identical model scenarios.

On log–log axes, the flux identity $Q_{\uparrow} = A\, q_{\uparrow}$ becomes a coordinate system: contours of constant $q_{\uparrow}$ are diagonals, spaced one isopleth per doubling (Figure 18).

S_{lower} increases with bedrock lowering and drives greater specific discharge with no change in inundated area. Across all channel states and discharge levels, S_{lower} yields similar proportional increases in $q_{\uparrow}$ (Figure 18). Linear axes hide this consistency, since proportional changes appear smaller at lower specific discharge (Figure 16).

At baseflow, restoration doubled both the specific discharge and inundated area of the unrestored channel, roughly quadrupling $Q_{\uparrow}$. At the annual flood, the restoration effect grew to five-fold. Specific discharge declined similarly in both channels, but the unrestored channel gained proportionally less inundated area. At bankfull flow, the restoration benefit dropped to about three-fold. The unrestored channel gained substantially in both specific discharge and inundated area; the restored channel gained specific discharge but little additional area. At overbank flow, the restoration benefit dropped below two-fold. The unrestored channel again gained both area and specific discharge. The restored channel gained area but lost specific discharge, leaving $Q_{\uparrow}$ unchanged.

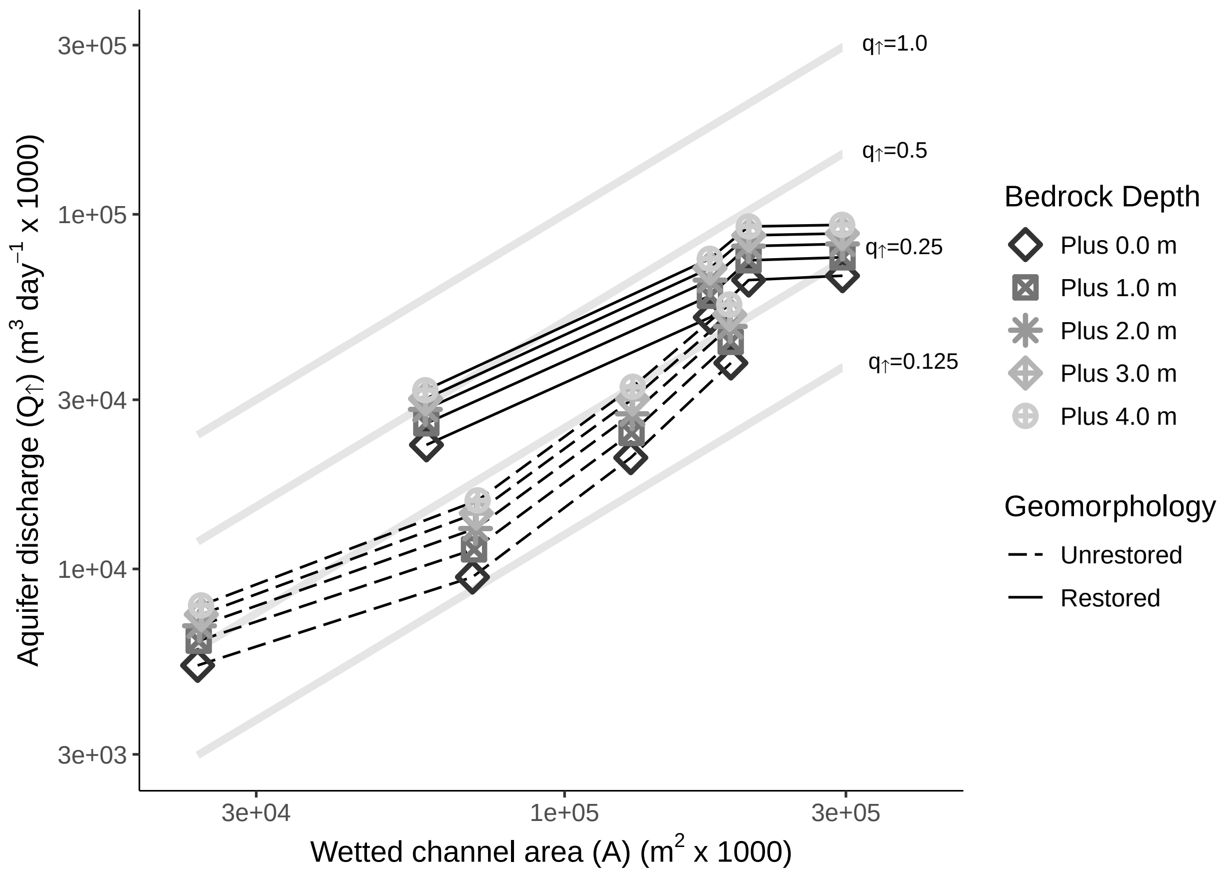

Figure 18: Aquifer discharge ($Q_{\uparrow}$) versus wetted area (A) on log–log axes. Points represent model outputs grouped by aquifer storage (symbol) and restoration state (line style).

Restoration Effects on Aquifer Turnover Rate In both channels, mean aquifer turnover rate decreased as aquifer storage increased (Figure 19). If aquifer discharge stayed constant, larger aquifer volumes would take longer to turn over. However, aquifer discharge was not constant: it increased with aquifer storage (Figure 17), though not enough proportionally to keep pace. Mean turnover rate therefore decreased nonlinearly with storage. Turnover rate also increased with stream discharge.

Holding discharge and storage constant, restoration yielded higher mean aquifer turnover rates through greater wetted area and higher specific discharge. At baseflow, restoration tripled the turnover rate. The effect peaked at fourfold at the annual flood. At bankfull, it dropped back to about threefold. At overbank flow, the restoration effect was smallest, about twofold.

In the unrestored channel, turnover rate rose more with each successive step to higher discharge. The base-to-annual step added the least, and the bankfull-to-overbank step the most. The restored channel showed the opposite: the base-to-annual step added the most, and the bankfull-to-overbank step added negligibly.

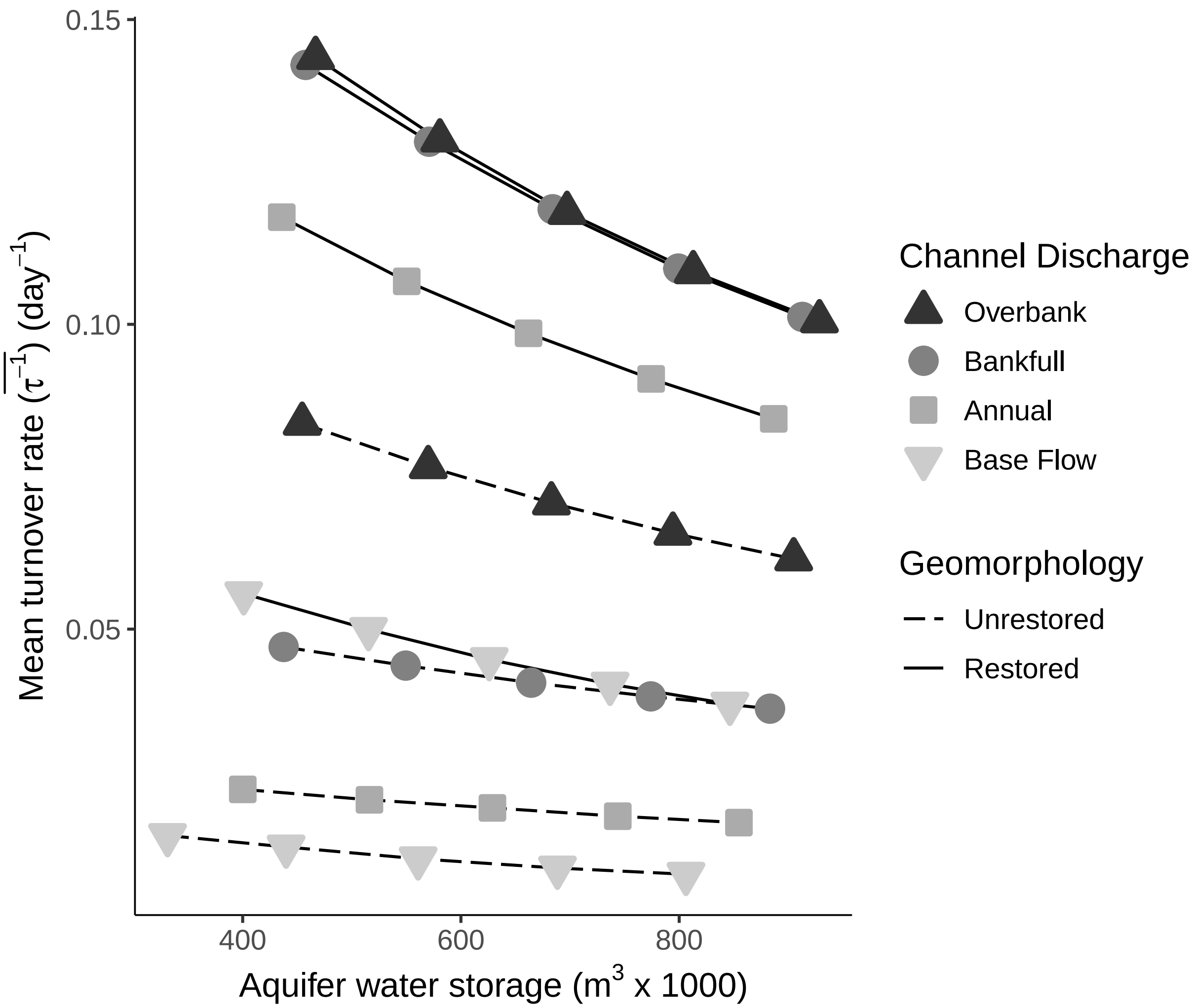

Figure 19: Mean turnover rate $(1/\bar{\tau})$ versus aquifer storage (S) for unrestored and restored states for each stream discharge. Points represent model outputs, connected by lines.

Discussion

Modeled Water Table and Stream Stage Relationships

The model reproduced the overall pattern of water-table response to discharge observed at monitoring wells across the Meacham Creek floodplain, but underestimated how rapidly the water table rose with discharge, particularly at higher flows. The bias suggests that calibrated channel roughness was effectively lower than actual roughness; modeled estimates of dynamic storage at high flow are therefore likely conservative. The model was not built to predict Meacham Creek's water-table response in detail. Its purpose was to provide a calibrated representation of two reach configurations, a confined plane-bed reach and a wide pool-riffle reach, in which restoration-state contrasts could be examined. The same channel and floodplain roughness coefficients calibrated each configuration, so the underestimation enters both scenarios in the same direction, and the contrasts reported here are robust to its magnitude.

Controls on Specific Discharge

The shape of the $q_{\uparrow}$–S relationship reflects two kinds of aquifer storage change: structural variation, set by alluvium thickness at fixed discharge, and dynamic variation, set by changes in stream discharge (Figure 16). Streambed elevation, alluvial depth, and structural storage are three expressions of the same geometric variable. Aggrading the streambed deepens the alluvium, lengthens subsurface flow paths, and proportionally increases structural storage. Because stream discharge is held constant within each series, variation in S along a series is entirely structural, and the influence of structural storage on $q_{\uparrow}$ is expressed by the shape of each series on the plot.

Between series, variation in S is dynamic. Increasing stream discharge raises the stream stage, which raises the water table in the adjacent floodplain aquifer and saturates additional aquifer volume above the streambed. The stage–discharge relationship depends on both channel cross-section and channel roughness. At-a-station hydraulic geometry (AHG) formalizes this dependence, expressing stage and width as power-law functions of discharge with exponents determined by cross-section geometry and roughness [29, 33, 48, 49]. The confined, leveed plane-bed channel is narrow with steep banks, so each discharge increment produces a large stage response and dynamic storage accumulates rapidly. The wider, floodplain-connected restored channel develops less stage per unit discharge, so dynamic storage accumulates more gradually. Across the four flow states, $q_{\uparrow}$ at a given alluvial depth traces a non-monotonic path: it first declines as expanding wetted area recruits lower-relief surfaces that dilute the spatial average, then recovers as steeper bank surfaces re-engage at higher flows.

Variation in $q_{\uparrow}$ across our scenarios traces back to variation in the mean VHG. Darcy's law [28] provides the link:

$$q_{\uparrow} = -K\frac{dh}{dl}, \tag{26}$$

Hydraulic conductivity (K) is constant across all scenarios in our model, so $q_{\uparrow}$ is proportional to the mean VHG. We use Δh to denote the mean head difference that, expressed over the relevant flow-path length, produces this gradient:

$$q_{\uparrow} \propto \Delta h. \tag{27}$$

The restored channel produces higher $q_{\uparrow}$ than the unrestored channel at every flow and alluvial depth (Figure 16), which means restoration enhanced mean Δh throughout the system. The restored channel's meandering pool-riffle morphology generates both planform and profile heterogeneity that the unrestored plane-bed channel lacks. In profile, the pool-riffle sequence forms a periodic bedform whose amplitude is the elevation difference from pool bottom to riffle crest (conventionally measured as residual pool depth) and whose wavelength is the spacing between successive crests. Greater amplitude and shorter wavelength concentrate elevation differences over shorter distances. In planform, increased sinuosity introduces meander bends with their own amplitude and wavelength, imposing cross-bend pressure contrasts at the streambed surface [11, 14]. Bed topography sets head differences across the streambed surface; the resulting hyporheic flow paths penetrate the subsurface to a depth that scales with bedform wavelength [31, 38, 92]. Where alluvium is shallow, bedrock truncates the flow paths before they reach their natural penetration depth, so much of the available geomorphic Δh goes unrealized as gradient near the streambed. Each additional meter of alluvium lets the flow paths develop further before truncation; the gain diminishes as alluvial depth approaches the natural penetration depth. The restored channel's greater bedform relief and sinuosity set larger head differences across the streambed; its within-series rises in $q_{\uparrow}$ are steeper because more Δh is available to express as alluvial depth increases.

During the three within-bank flow states (base, annual flood, and bankfull), the pattern of $q_{\uparrow}$ change with increasing discharge is similar across the restored and unrestored channels (Figure 16), indicating that the change in mean VHGs with increasing flow is similar for both channel types so long as flow remains within the banks. In contrast, from bankfull to overbank, water spreads substantially farther onto the floodplain in the restored channel than in the unrestored channel at the same stream discharge (Figure 14), and the $q_{\uparrow}$ responses diverge: $q_{\uparrow}$ continues to increase in the unrestored channel but declines in the restored channel. On the restored floodplain, the expansive overbank surfaces contribute negligible exchange because surface water velocity is low, roughness is high, and the distal floodplain lacks the bed features that generate hydraulic gradients.

Whole Floodplain Aquifer Discharge

Total aquifer discharge across the floodplain ($Q_\uparrow$) is by definition the product of specific discharge ($q_\uparrow$) and wetted area (A). With hydraulic conductivity constant in the model, $q_\uparrow$ is proportional to the mean vertical head difference Δh (by Darcy's law, established above):

$$\begin{aligned} Q_\uparrow &= A\, q_\uparrow \\ &\propto A \Delta h. \end{aligned} \tag{28}$$

Restoration influences $Q_\uparrow$ through both factors, area and specific discharge. The wider, floodplain-connected restored channel wets more streambed area at any given Q, expanding the domain over which exchange fluxes are integrated [30]. Elevating the streambed increases aquifer storage (S) and proportionally steepens hydraulic gradients, increasing $q_\uparrow$. Pool-riffle morphology further increases $q_\uparrow$ through the bedform- and planform-scale head differences described above. Bed topography is a strong predictor of hyporheic exchange at reach scale [57], and the head variations it generates are the dominant control on exchange flux in pool-riffle channels [83].

A natural question arises: as $Q_\uparrow$ varies across flow magnitudes and between restoration states, how much of that variation is attributable to differences in A, and how much to differences in $q_\uparrow$? Movement along an isopleth in Figure 18 represents a pure area effect at constant specific discharge. Where the observed slope between two points is steeper or shallower than the isopleth, $q_\uparrow$ must also have changed; the departure from unit slope indicates the direction and relative magnitude of the $q_\uparrow$ change. Because $Q_\uparrow = A\, q_\uparrow$ is multiplicative, fractional changes in A and $q_\uparrow$ do not simply sum to the fractional change in $Q_\uparrow$ but compound, generating an interaction term that grows with the magnitude of each change:

$$\frac{\Delta Q_{\uparrow}}{Q_{\uparrow}} = \frac{\Delta A}{A} + \frac{\Delta q_{\uparrow}}{q_{\uparrow}} + \frac{\Delta A}{A} \cdot \frac{\Delta q_{\uparrow}}{q_{\uparrow}}. \tag{29}$$

(See Appendix C for derivation.) We quantify this decomposition for each flow transition and between restoration states in Appendix C, and draw on those results throughout the following discussion.

The same specific discharge produces more total exchange where wetted area is larger, because $Q_{\uparrow} = A\, q_{\uparrow}$. At baseflow, wetted area is small, so even strong vertical hydraulic gradients produce modest $Q_{\uparrow}$. As stream discharge increases, the expanding wetted area amplifies the effect of S on $Q_{\uparrow}$. This amplification should be stronger in the restored channel, where the wider floodplain-connected morphology wets substantially more streambed at every flow. Figure 17 confirms these expectations and reveals additional structure in how A and $q_{\uparrow}$ shape both the magnitude and efficiency of streambed exchange.

Across flow transitions, the fractional change in wetted area consistently exceeds the fractional change in specific discharge in both geomorphologies, but the pattern of area gains reflects channel geometry (Appendix C). These contrasting patterns reflect the cross-section geometries of the two channels: the restored channel's wide, low-banked cross section produces a large width response at sub-bankfull flows, while the confined channel's steep banks concentrate the discharge response in depth. The wider restored channel wets most of its between-bank area at flows below bankfull, as A roughly triples between baseflow and annual flow ($\Delta A/A \approx 200\%$) then gains little additional area until the floodplain inundates above bankfull. In the narrower, confined plane-bed channel, wetted area increases more gradually across the full range of flows. Above bankfull, floodplain connection further differentiates the two: the restored channel wets its floodplain directly, while the leveed plane-bed channel gains area primarily by seepage where the water table intersects low-lying surfaces behind the levee (Figure 14).

Expanding wetted area dilutes the spatial average of $q_\uparrow$ because the surfaces recruited at each successive flow differ in topographic character from those already wetted. As discharge rises, $q_\uparrow$ falls while the growing wetted area drives $Q_\uparrow$ upward. Boano et al. (2013) [14] found the same mechanism at the bedform scale: water exchange per unit streambed area decreases with discharge because each bedform footprint grows faster than its volumetric exchange rate. Their simulations held channel width constant, so the per-area decline was not offset by area expansion; in our reach-scale analysis, the growing wetted area more than compensates. Across the baseflow-to-annual transition, $q_\uparrow$ declines 24–39% while A nearly triples, yielding a net increase in $Q_\uparrow$ of 77–135% depending on restoration state (Tables 29 and 32; Figure 17).

Storage increases produce proportional gains in Δh and $q_\uparrow$ regardless of flow magnitude, but the resulting gain in $Q_\uparrow$ scales with wetted area and therefore grows with discharge (Figure 17). The interaction term captures this amplification: it is substantial wherever both A and $q_\uparrow$ changes are large (Appendix C). The restored channel, having already wetted most of its between-bank area at annual flow, amplifies the storage effect across a wider range of flows than the confined plane-bed channel.

Restoration increases $Q_\uparrow$ at every flow magnitude, but the effect diminishes with increasing discharge. At baseflow the restored channel produces roughly four times the streambed discharge of the unrestored channel, driven by its larger wetted area ($\Delta A/A \approx$ 144%) reinforced by steeper vertical hydraulic gradients ($\Delta q_\uparrow/q_\uparrow \approx 70\%$; Table 35). The effect peaks at annual flow, where both area and specific discharge differences are large enough that their interaction alone exceeds either individual contribution (Table 36). Above annual flow, the contrast between channels narrows. At bankfull, the unrestored channel has expanded within its banks and narrowed the area gap, while the specific discharge contrast, now the larger term, reflects the pool-riffle morphology's greater bedform relief. By overbank flow, the specific discharge difference has largely collapsed ($\Delta q_{\uparrow}/q_{\uparrow} < 15\%$) even as the area difference persists ($\Delta A/A \approx 55\%$; Table 38), and the restoration effect drops below twofold.

The asymptotic $q_{\uparrow}$–S relationship established above, where each additional meter of alluvium contributes less incremental Δh as hyporheic flow paths approach their natural penetration depth, propagates into $Q_{\uparrow}$. The $Q_{\uparrow}$–S curves in Figure 17 are concave down at all flows and in both geomorphologies. This concavity is stronger at higher flows, where larger wetted areas amplify both the magnitude of $Q_{\uparrow}$ and the rate at which marginal gains decline. The restored channel exhibits greater concavity across all flows. The decomposition accounts for the multiplicative interaction between A and $q_{\uparrow}$ but does not explain why the marginal response weakens. That explanation requires examining two geomorphic constraints on $Q_{\uparrow}$ that we develop in the following section.

Geomorphic Controls on Exchange Capacity

The asymptotic $Q_{\uparrow}$–S curves in Figure 17 and the narrowing contrast between channels at high flows arise from two independent constraints on $Q_{\uparrow}$, each subject to its own diminishing returns. The first is the finite extent of the exchange interface: as developed above, expanding wetted area recruits progressively lower-relief surfaces, so the marginal gain in $Q_{\uparrow}$ per unit of A declines. The second is the finite depth to which geomorphic head differences propagate as hydraulic gradients. The pressure distributions imposed by bedform relief and by sinuosity [22, 70] decay exponentially below the streambed, and the resulting hyporheic flow paths penetrate to a depth set by bedform wavelength. Where alluvium is shallow, bedrock truncates these flow paths before the full geomorphic Δh is expressed as gradient [31, 83, 92]. Each additional meter of alluvium therefore steepens gradients less than the last, even as it adds the same increment to storage.

These two constraints operate simultaneously and compound via Darcy's law. When both A and Δh are far from their respective maxima, changes in either factor amplify the other, and the interaction term in the decomposition is large. This is the condition at intermediate flows in the restored channel, where the exchange interface is still expanding and gradients have not yet exhausted the available geomorphic relief; the interaction term at annual flow exceeds either individual contribution (Table 36). At overbank flow, both channels approach their respective maxima and the compounding attenuates.

Restoration acts on both constraints. A wider, lower-banked cross section lets rising discharge spread through width rather than depth, expanding the exchange interface over a broader range of flows. Greater residual pool depth, shorter bedform wavelength, and increased sinuosity steepen hydraulic gradients. The model represents these features through the LiDAR-derived surface topography of each scenario (§**??**). Moreover, the restored channel sustains gradient development to greater depth because its increased alluvial depth lets hyporheic flow paths develop further before reaching bedrock. At Meacham Creek, however, maximum alluvial depth reaches only approximately 5 m, and bedrock truncates the flow paths before the full geomorphic Δh develops; gradient potential remains unrealized. In deeper alluvial settings such as the Nyack floodplain of the Middle Fork Flathead River [62, 74], where alluvium exceeds 50 m, hyporheic flow paths develop fully and additional storage beyond the penetration depth adds volume without further steepening gradients.

<u>Exchange Efficiency and Turnover Rate</u> Turnover rate ($1/\bar{\tau} = Q_{\uparrow}/S$) measures how rapidly stored water is exchanged through the streambed. Because exchange rate, storage volume, and water age are inexorably linked in any hyporheic zone [64], the geomorphic controls on $Q_{\uparrow}$ identified above necessarily shape turnover as well. Because $Q_{\uparrow} = A\,q_{\uparrow}$, turnover rate can be written

$$\frac{1}{\bar{\tau}} = \frac{Q_{\uparrow}}{S} = \frac{q_{\uparrow}}{S/A}, \tag{30}$$

which separates two controls. The numerator, $q_\uparrow$, reflects how fully geomorphic head differences are expressed as hydraulic gradients at a given alluvial depth. The denominator, S/A, is the aquifer storage volume per unit of wetted streambed. Where the hyporheic zone is confined beneath the wetted channel [83], S/A equals the mean aquifer depth below the streambed. In our setting, the floodplain aquifer extends well beyond the channel margins, so S/A no longer reduces to a vertical depth. It generalizes to the mean length of hyporheic flow paths, a characteristic length scale of the circulation. Each unit of wetted streambed must turn over aquifer volume that lies both beneath and laterally beyond it. S/A therefore exceeds the mean aquifer depth below the streambed; the excess measures the lateral storage each unit must still turn over.

Rewriting Equation 30 as $1/\bar{\tau} = q_\uparrow \cdot (A/S)$ reveals the same multiplicative structure as $Q_\uparrow = A\, q_\uparrow$, and the same fractional decomposition applies:

$$\frac{\Delta(1/\bar{\tau})}{1/\bar{\tau}} = \frac{\Delta q_\uparrow}{q_\uparrow} + \frac{\Delta(A/S)}{A/S} + \frac{\Delta q_\uparrow}{q_\uparrow} \cdot \frac{\Delta(A/S)}{A/S}. \tag{31}$$

(See Appendix D for derivation.) As with the $Q_\uparrow$ decomposition, the interaction term is a bookkeeping consequence of the multiplicative structure, not a separate physical mechanism. The first two terms isolate the contributions of changing gradient intensity and changing storage burden per unit area, while the interaction captures their compounding. Full results across all flow transitions and alluvial depths are reported in Appendix D.

At fixed flow, turnover rate declines monotonically as alluvial depth increases (Figure 19, within-series slopes). Wetted area is approximately constant along a series, so S/A increases in proportion to S, and the decline indicates that $q_\uparrow$ does not keep pace. This is diminishing returns on gradient development: each additional meter of alluvium steepens gradients less than the last while adding the same increment to storage. In the framework of [64], the added storage is disproportionately older water traversing longer, deeper flow paths that contribute less to discharge per unit time. Hence, the age distribution shifts toward older water as turnover slows. The restored channel shows the more pronounced within-series response because pool-riffle morphology imposes a periodic head distribution at the streambed that drives hyporheic flow paths to a wavelength-scaled penetration depth. The plane-bed unrestored channel lacks comparable periodic bedforms, so the streambed-imposed head distribution is unstructured and the gradient available to develop with alluvial depth is correspondingly limited.

When discharge rises at fixed alluvial depth, the wetted streambed expands faster than storage volume grows. Each square meter of streambed then services a smaller volume of aquifer water, and turnover rate rises (Figure 19). The mechanism is not intensified flux per unit area: between baseflow and annual flow, $q_{\uparrow}$ declines 24–39% as newly wetted low-relief surfaces dilute the spatial average (Tables 29 and 32). Yet turnover more than doubles in the restored channel and rises 47–87% in the unrestored channel (Tables 42 and 39). Wetted area roughly triples while total storage increases modestly, so the storage burden per unit streambed drops sharply. The A/S term in the turnover decomposition increases 142–190% across positions and channels at this transition (Tables 39 and 42), far exceeding the $q_{\uparrow}$ decline. Because $q_{\uparrow}$ and A/S shift in opposite directions, the interaction term is negative and partially offsets the A/S gain without reversing it. At higher flows, area continues to expand and accounts for most of the additional turnover gain. The efficiency increase with flow is thus primarily an area effect: expanding the exchange interface reduces the per-unit-area storage burden faster than the dilution of $q_{\uparrow}$ can offset it.

The contrast in turnover rate between channels is largest at annual flow, approximately fivefold (Table 46), where both $q_{\uparrow}$ and A/S contribute. The restored channel has a higher A/S because its wider morphology wets nearly three times the area at similar total storage. It also has a higher $q_{\uparrow}$ because its pool-riffle relief and greater sinuosity generate steeper gradients. At overbank flow, both channels have recruited most of their available exchange area and gradients have largely exhausted the available geomorphic relief, and the difference narrows to less than twofold. The restored bankfull-to-overbank transition is particularly revealing: turnover rate barely changes because the $q_{\uparrow}$ decline from flooding low-gradient floodplain surfaces (approximately -29%) nearly cancels the A/S gain from the accompanying area expansion (approximately $+42\%$), with the negative interaction absorbing the residual (Table 44).

Implications for Restoration

Restoration at Meacham Creek acted on both the area limit and the gradient limit. Repositioning the channel from its incised path, where the streambed sat near bedrock, onto thicker floodplain deposits increased effective alluvial depth, modestly raising the gradient limit. Separately, reconstructing pool-riffle morphology with greater sinuosity imposed steeper pressure variations at the streambed surface, increasing the head differences available to drive exchange within the alluvial depth available to express them. Widening the channel and lowering the banks produced a cross-section shape with a larger width exponent, extending the area limit across a broader range of flows. The interaction between these effects is largest at intermediate flows, where neither constraint is yet binding and the multiplicative structure of Darcy's law allows modest gains in each factor to compound. At overbank flow, both channels approach their respective limits and the restoration effect attenuates, not because restoration ceases to matter, but because both constraints are nearly fully expressed.

The contrasting AHG responses also clarify why the turnover increase with discharge is primarily an area effect rather than a storage efficiency effect. In the restored channel, discharge increases are preferentially accommodated by width, expanding the exchange interface, rather than by depth, which adds dynamic storage. The ratio S/A therefore shrinks rapidly with discharge; each square meter of streambed services a smaller volume of aquifer water. In the plane-bed channel, where stream depth accommodates a larger share of the discharge response, dynamic storage grows faster relative to area and the S/A reduction is less pronounced. The contrast in turnover between channels is largest at the flows where the restored channel's AHG response most strongly favors width over depth.

Several questions raised by this work extend beyond the scope of our analysis. In deeper alluvial settings, where alluvial depth exceeds the natural penetration depth of hyporheic flow paths, the gradient limit would be fully expressed and additional structural storage would add aquifer volume without further increasing exchange. Similarly, our steady-flow modeling assumes that each flow state persists long enough to reach equilibrium, an assumption that likely holds at baseflow but not at brief high-flow events. The modeling also does not capture how transient flood pulses interact with the area limit and gradient limit on event timescales, a dynamic that may matter most for ecological processes governed by exchange during rising and falling hydrographs. Finally, connecting the exchange metrics developed here (turnover rate, the S/A ratio, and the decomposition of $Q_{\uparrow}$) to measurable ecological outcomes such as thermal buffering, nutrient cycling, and benthic habitat quality would strengthen the case for incorporating hyporheic objectives explicitly into restoration design.

Conclusions

Our factorial modeling experiment at Meacham Creek showed that floodplain restoration altered how aquifer discharge couples to wetted area and hydraulic gradients across the hydrograph. Aquifer discharge rose under restoration across all modeled flows and storage scenarios, with relative gains of roughly fivefold at annual flood and below twofold at overbank. Gains in wetted area carried the largest share of the aquifer-discharge gain across the hydrograph. At moderate flows, wetted-area and specific-discharge gains compounded, consistent with Darcy's law when neither the exchange interface nor hydraulic gradients have reached their geomorphic limits. Position-by-position tables of the $Q_\uparrow = A\,q_\uparrow$ decomposition appear in Appendix C.

The systematic variation in restoration effects across the hydrograph reflects two geomorphic constraints that jointly bound exchange capacity, each subject to diminishing returns. The first is the area limit: the active extent of the exchange interface, governed by channel cross-section shape and its expression through AHG. The restored pool-riffle channel, with its wider cross section and lower banks, spreads the discharge response across width, recruiting new exchange surface over a broad range of sub-bankfull flows. The confined plane-bed channel concentrates the response in depth, approaching its area limit earlier. The second is the gradient limit: the degree to which geomorphic head differences propagate as hydraulic gradients into the subsurface, constrained by the depth of alluvium above bedrock. Where alluvium is shallow, bedrock truncates hyporheic flow paths and gradient potential goes unrealized; greater bedform relief and sinuosity in the restored channel impose larger head differences at the streambed but cannot overcome the alluvial depth available to express them as gradient.

The turnover analysis confirmed that efficiency gains with increasing discharge are primarily an area effect: expanding the exchange interface reduces the storage volume each square meter of streambed must turn over (S/A) faster than the accompanying drop in specific discharge can offset it. Restoration design can target specific geomorphic features controlling each constraint: cross-section shape and floodplain connectivity for the area limit, bedform relief and alluvial depth for the gradient limit. Area-limit and gradient-limit effects should compound most strongly at the moderate flows that dominate annual hydrographs. Unlike semi-empirical approaches that resolve exchange from discrete morphometric parameters such as bedform wavelength and amplitude [42, 83], our decomposition treats the geomorphic state as an integrated whole. It separates how much of the restoration effect flows through area expansion versus gradient intensification, but does not identify which specific design elements drive $\Delta q_{\uparrow}$. Chapter 3 partitions $\Delta q_{\uparrow}$ between storage change and geomorphic complexity, though it too treats complexity as a whole-state comparison rather than resolving discrete morphometric parameters.

PARTITIONING THE RESTORATION EFFECT AMONG CHANNEL COMPLEXITY, ALLUVIAL DEPTH, AND EXCHANGE AREA

Introduction

Stream restoration has evolved through distinct paradigms that increasingly recognize the importance of process-based design. Historically, restoration emphasized form-based solutions derived from channel classification schemes [71], relying heavily on engineering and construction to design channel forms that emulated the characteristic morphology of target stream classes. More recent restoration paradigms emphasize designs that eliminate physical constraints on fluvial processes, such as levees, to promote normative geomorphic processes that shape and maintain channel reach geomorphology [9, 25, 91]. A related approach recognizes that widespread loss of floodplain storage due to bed degradation necessitates strategies to encourage bed aggradation [26, 61]. Some restoration practitioners now recognize deliberate restoration of hyporheic processes as fundamental to recovering stream ecosystem functions, rather than merely an incidental outcome of channel restoration [41].

We recognize three primary restoration outcomes that systematically alter hyporheic hydrology, regardless of the specific paradigm or combination of paradigms that guided the restoration design. First, reconstructing pool-riffle morphology with greater sinuosity steepens the near-bed pressure variations that drive water into and out of the streambed. Second, removing levees and reconnecting the floodplain wets more streambed at any given flow, expanding the interface through which the stream and aquifer exchange water. Third, repositioning the channel onto thicker floodplain deposits deepens the alluvium available for hyporheic flow, allowing pressure fields to propagate further into the subsurface. The three outcomes act at any restored site, individually or simultaneously, but how much each contributes to increased hyporheic exchange, and whether that balance shifts with discharge, has not been resolved.

Two decades of research have established that hyporheic exchange scales with bedform geometry and alluvial depth [20, 24, 82]. Bedform amplitude and wavelength set the near-bed pressure variations that drive vertical exchange [11, 55, 85], while stream sinuosity generates lateral exchange across meander bends [12, 22]. Bedform and sinuosity controls interact across spatial scales in ways that resist simple superposition [13, 42–44]. Tonina and Buffington [84] present a systematic treatment for confined pool-riffle channels, demonstrating that hyporheic volume scales with bedform wavelength, bedform elevation, and alluvial depth, and that alluvial depth limits its maximum vertical extent. Although their findings may not directly apply to unconfined floodplain rivers, where sinuosity generates exchange across meander bends, alluvial depth likely limits both the maximum vertical expression and maximum rate of hyporheic exchange in bedrock-bounded mountain drainage basins.

In Chapter 2, we used the multiplicative form of Darcy's law, which expresses aquifer discharge as the product of specific discharge and wetted area ($Q_{\uparrow} = A\,q_{\uparrow}$), to decompose changes in aquifer discharge across flow transitions and between restoration states at Meacham Creek. That decomposition showed that expanding the wetted streambed was consistently the single largest contributor to increased $Q_{\uparrow}$, that the restored channel produced higher $Q_{\uparrow}$ at every flow, and that the restoration effect diminished with increasing discharge as both channels approached their respective area and gradient constraints. The decomposition quantified how much of each change in $Q_{\uparrow}$ traced to wetted area versus specific discharge, but it could not resolve what produced the flux differences between channels. Increased channel complexity, greater alluvial depth, and their interaction all plausibly contribute to the restored channel's higher $q_{\uparrow}$, and disentangling these requires a model that relates $q_{\uparrow}$ to its geomorphic controls.

Resolving these contributions matters beyond this site. Restoration projects operate under constraints that rarely permit every possible intervention, and practitioners need to know which geomorphic changes produce the largest hyporheic gains at the flows most relevant to their ecological objectives. A framework that partitions $\Delta Q_{\uparrow}$ among its geomorphic controls would connect the research literature on hyporheic exchange mechanisms to the practical problem of evaluating restoration design tradeoffs.

In this chapter, we develop a semi-empirical model that predicts specific discharge from aquifer storage and geomorphic state, fit it to factorial hydrogeologic simulations of the Meacham Creek restoration, and use it to partition $\Delta Q_{\uparrow}$ among the exchange interface, channel complexity, and alluvial depth across four flow conditions. The partitioning reveals how the relative importance of each restoration outcome shifts with discharge, and why.

Model Development

The model predicts $q_{\uparrow}$ from aquifer storage (S) and geomorphic state (G, unrestored or restored). Rather than isolating individual exchange mechanisms [84], this approach captures the collective effect of switching geomorphic states, which integrates changes in bedform amplitude, pool spacing, sinuosity, and cross-section shape. The analytical framework we develop is pragmatic: it evaluates how restoration-induced geomorphic changes affect hyporheic exchange in bedrock-bounded mountain drainage basins, where multi-scale topographic features interact in complex, non-linear ways [11, 15].

We herein systematize our approach by considering fundamental changes in hyporheic hydrology between the unrestored and restored states, which we denote using "delta" notation. Throughout this paper, the notation Δx refers to the difference between a restored state (x_r) and an unrestored state (x_u):

$$\Delta x = x_r - x_u \tag{32}$$

As such, x and Δx always share the same dimensions.

Restoration modifies three hydrologic quantities: wetted surface area (ΔA; $[L^2]$), aquifer water storage (ΔS; $[L^3]$), and mean hyporheic transit time ($\Delta\bar{\tau}$; $[T]$). Changes in these quantities drive changes in hyporheic water exchange ($\Delta Q_{\uparrow}$; $[L^3][T]^{-1}$). For purposes of contrast, we view the hyporheic zone as a pool of S with an inflow that approximates outflow ($Q_{\downarrow} \approx Q_{\uparrow}$) and consider two fundamental hydrologic relationships: that between $Q_{\uparrow}$, S, and $\bar{\tau}$:

$$Q_{\uparrow} = \frac{S}{\bar{\tau}} \tag{33}$$

and that between $Q_{\uparrow}$, A, and specific discharge ($q_{\uparrow}$; $[L][T]^{-1}$):

$$Q_{\uparrow} = Aq_{\uparrow} \tag{34}$$

In bedrock-bounded mountain drainage basins, where alluvial depth is much less than potential hyporheic depth, we assume that the entire floodplain aquifer participates in hyporheic exchange. Under these conditions, any increase in alluvial depth directly increases hyporheic exchange volume and influences residence time distributions.

The magnitudes of $\Delta Q_{\uparrow}$, ΔA, ΔS, and $\Delta\bar{\tau}$ are inherently site-specific, shaped by how the restoration design interacts with local geomorphology and hydrology. Nevertheless, most restoration designs yield one or more of the following:

- an increase in A, via adding sinuosity and lateral habitats such as side channels or by increasing the hydrologic connection between channels and floodplains [9, 26];

- an increase in S, by elevating stream channels to reverse past streambed degradation [26, 61];
- a reduction in $\bar{\tau}$, by adding channel complexity (e.g., meander bends, side channels, bars, off-channel aquatic habitats) or increasing stream-bed topography (e.g., pool-riffle sequences, roughness elements), thereby reducing mean hyporheic flow-path length [64, 81, 84].

Considering the form of Equations 33 and 34, a positive ΔA, a positive ΔS, or a negative $\Delta\bar{\tau}$ would each tend to contribute to a positive $\Delta Q_{\uparrow}$.

To partition these contributions, we need an equation that predicts $q_{\uparrow}$ from measurable quantities. The following development builds that equation from the relationships above.

Ideally, to investigate the interactive effects of ΔA, ΔS and $\Delta\bar{\tau}$ on $Q_{\uparrow}$, we would derive an equation from first principles that expresses $Q_{\uparrow} = f(A, S, \bar{\tau})$. However, Equations 33 and 34 show that $Q_{\uparrow}$ is fully described by any given combination of S and $\bar{\tau}$. Therefore, from the perspective of first principles, A cannot be included with S and $\bar{\tau}$ as an independent predictor of $Q_{\uparrow}$. Restoration actions induce ΔA, ΔS, and $\Delta\bar{\tau}$ simultaneously, and each influences $\Delta Q_{\uparrow}$ through complex interactions.

The apparent tension between the mathematical constraint and the physical reality that all three variables respond independently to restoration can be resolved by using an empirical equation, guided by first principles. If we combine Equations 33 and 34, we find:

$$Aq_{\uparrow} = \frac{S}{\bar{\tau}} \tag{35}$$

suggesting that, for any given A:

$$q_{\uparrow} \propto \frac{S}{\bar{\tau}} \tag{36}$$

The hypothesized relation between restoration and hyporheic response suggests that many stream restoration projects influence $\bar{\tau}$ in two specific, but countervailing ways. First, an increase in S creates the opportunity for longer-duration hyporheic flow paths, thereby increasing $\bar{\tau}$. In contrast, increased channel and floodplain geomorphic complexity (i.e., ΔG; unitless) from the pre-restoration state ($G = 0$) to the post-restoration state ($G = 1$) tends to reduce flow path duration, thereby reducing $\bar{\tau}$. If $\bar{\tau} = f(S, G)$, substituting into Proportionality 36 yields:

$$q_{\uparrow} \propto \frac{S}{f(S, G)} \tag{37}$$

Proportionality 37 takes its form from first principles but gives us guidance to design a semi-empirical equation to predict $q_{\uparrow}$ from S under unrestored ($G = 0$) and restored ($G = 1$) conditions. Our data further indicate that $q_{\uparrow}$ is predictable using a multiple linear regression with $\log(S)$ and G and an interaction term:

$$\hat{q}_{\uparrow} = \beta_1 \log(S) + \beta_2 G + \beta_3 G \log(S) + c \tag{38}$$

Equation 38 takes the form of a multiple regression but is semi-empirical: its structure derives from the proportionality in Equation 37. The logarithmic transformation of S should adequately represent non-linearity between $q_{\uparrow}$ and S because S appears in both numerator and denominator of 37. For unrestored conditions ($G = 0$), Equation 38 reduces to:

$$\hat{q}_{u\uparrow} = \beta_1 \log(S) + c \tag{39}$$

which simply describes a linear relationship between $\hat{q}_{u\uparrow}$ and $\log(S)$ for a fixed geomorphic state. For restored conditions ($G = 1$), Equation 38 posits an altered linear relationship between $\hat{q}_{r\uparrow}$ and $\log(S_r)$, expressed as a change in slope ($\Delta\beta_1$) and intercept (Δc) relative to Equation 39:

$$\hat{q}_{r\uparrow} = (\beta_1 + \Delta\beta_1)\log(S_r) + (c + \Delta c) \tag{40}$$

In Equation 38, $\beta_2 = \Delta c$ and $\beta_3 = \Delta\beta_1$, as can be demonstrated by substituting β_2 and β_3 into Equation 40 to derive Equation 38 for $G = 1$:

$$\begin{aligned} \hat{q}_{\uparrow} &= (\beta_1 + \beta_3)\text{log}(S) + (c + \beta_2) \\ &= \beta_1\text{log}(S) + \beta_2 + \beta_3\text{log}(S) + c. \\ &= \beta_1\text{log}(S) + \beta_2 G + \beta_3 G\text{log}(S) + c. \end{aligned} \tag{41}$$

Combining Equation 38 with Equation 34 yields a semi-empirical equation predicting $Q_{\uparrow}$ from A, S, and G:

$$\hat{Q}_{\uparrow} = A(\beta_1\log(S) + \beta_2 G + \beta_3 G\log(S) + c) \tag{42}$$

In this chapter, we apply Equation 42 to partition simulated $\Delta Q_{\uparrow}$ among its constituent factors: wetted area (A), aquifer storage (S), geomorphic state (G), and the storage-geomorphology interaction ($G{:}S$). The Meacham Creek restoration produced three measurable geomorphic changes, each of which enters the partitioning model through a distinct variable. We refer to these throughout by the geomorphic outcome they describe, regardless of the specific paradigm or combination of paradigms that guided the restoration design.

Channel complexity (G) captures the integrated change in profile and planform heterogeneity between the unrestored and restored states. The restored channel exhibits greater residual pool depth, closer pool spacing, and a more sinuous planform than the unrestored plane-bed channel. In the model, G enters as a binary indicator ($G = 0$ for the unrestored state, $G = 1$ for the restored state) that shifts both the intercept and the storage sensitivity of specific discharge (Equation 38). Because G bundles multiple morphometric features into a single state variable, it resolves the collective effect of increased channel complexity on $q_{\uparrow}$ but does not isolate individual contributions from bedform amplitude, wavelength, or sinuosity.

The exchange interface (A) is the wetted streambed area through which the aquifer and stream exchange water [30]. In Chapter 2, we showed that A defines the active domain for exchange and that expanding A was the single largest contributor to increased $Q_{\uparrow}$ across most flow conditions. In the partitioning model, A multiplies specific discharge to yield total aquifer discharge ($\hat{Q}_{\uparrow} = A\hat{q}_{\uparrow}$; Equation 42). Floodplain reconnection (the removal of levees and realignment of the channel) is the restoration action that expanded the exchange interface.

Alluvial depth (S) is the geometric quantity that aquifer storage represents in a bedrock-bounded system. Because bedrock is effectively impermeable and the alluvium is highly transmissive, the volume of stored water is proportional to the mean depth of alluvium above bedrock. In the model, S enters as aquifer storage volume, and $q_{\uparrow}$ scales with $\log(S)$ (Equation 38), reflecting the diminishing returns on gradient steepening as alluvial depth increases beyond the penetration depth of the geomorphic pressure field (Chapter 2). The restoration achieved greater alluvial depth not through grade control structures but by repositioning the channel atop thicker floodplain deposits.

Together, these three outcomes (channel complexity, the exchange interface, and alluvial depth) account for the full partitioning of $\Delta Q_{\uparrow}$ presented in this chapter. The model decomposes $\Delta Q_{\uparrow}$ in two layers: first into contributions from the exchange interface (A) and from changes in specific discharge ($\Delta q_{\uparrow}$), and then further decomposes $\Delta q_{\uparrow}$ into effects attributable to alluvial depth (S), channel complexity (G), and their interaction ($G{:}S$).

Methods

Study Area

Meacham Creek flows northward through the western Blue Mountains of north central Oregon, draining a 464 km^2 basin in the Columbia River Basalt terrane [54] before joining the Umatilla River (Figure 11). Along its lower 25 km, the creek flows through a ribbon-like floodplain 200–300 m wide, consisting of gravelly cobble alluvium 2–5 m deep overlying bedrock and bordered by steep valley walls with minimal soil development. Meacham Creek's bedrock-bounded, coarse-grained floodplain contains a phreatic aquifer that actively exchanges water with the creek. Consequently, the entire floodplain functions as a hyporheic zone.

The study reach is located approximately 8 km upstream of the confluence with the Umatilla River. The eastern edge of the floodplain is bounded by the Union Pacific Railroad and an adjacent access road. After historical high flows in 1965, the creek was confined to the western valley wall by a 4–5 m high levee, and spur dikes were constructed to deflect the creek away from the railway. In summer 2011, the Confederated Tribes of the Umatilla Indian Reservation completed a 1.6 km floodplain and channel restoration project that removed levees and dikes, realigned the channel, added large woody debris, and re-established riparian vegetation.

Three design elements at Meacham Creek correspond to the restoration outcomes the partitioning evaluates.

Channel complexity (G). By 2011, the levee-confined channel had incised to the bedrock valley floor, functioning like a flume: a straightened, plane-bed channel with low width-to-depth ratio and minimal profile and planform variability. The resulting uniformity limited the bedform-scale and reach-scale pressure variations that drive hyporheic exchange. Designed from historical aerial photographs and reference reaches in the basin, the restored channel features a sinuous, multi-threaded, pool-riffle morphology with substantially greater profile and planform heterogeneity. Larger bedform amplitudes and meander-bend geometry generate stronger near-bed pressure variations that drive hyporheic exchange. In the partitioning model, this change in morphological heterogeneity enters as channel complexity (G).

Alluvial depth (S). With the alluvium scoured to bedrock, the pre-restoration channel offered minimal storage for hyporheic flow. Strategic channel realignment achieved functional aggradation: relocating flow from the incised channel to the adjacent, unincised floodplain surface produced the effect of aggradation without sediment deposition. The new streambed sits above the original channel, raising the base level without grade control. By positioning the channel atop thicker floodplain deposits, the realignment expanded the volume of alluvium available for hyporheic exchange. In the partitioning model, this increased alluvial depth enters as aquifer storage (S).

The exchange interface (A). Confined and incised against the western valley wall, the pre-restoration channel developed only a narrow, inset floodplain typical of leveed systems. Levee removal and channel realignment restored lateral connectivity, and the sinuous, multi-threaded morphology readily accesses its floodplain at moderate flows, producing substantially greater wetted streambed area across the hydrograph. In the partitioning model, this expanded wetted area enters as the exchange interface (A).

The restored and unrestored reaches share the same valley geometry, alluvial stratigraphy, and hydrologic regime, isolating restoration design as the experimental variable. Pre- and post-restoration datasets support the factorial comparison: high-resolution LiDAR topography from 2009 and 2011, an as-built channel profile survey, floodplain water table elevation time series from twelve wells throughout the study area (2011–2016), and records from a United States Geological Survey (USGS) stream gauging station located 6 km downstream that has been active since 1975.

Model Fitting

We calculate $q_\uparrow$ for each scenario from

$$q_\uparrow = \frac{Q_\uparrow}{A}, \tag{43}$$

where $Q_\uparrow$ and A are obtained from aquifer systems with known tuples of $(Q_\uparrow, A, S, G)$.

Hydrogeologic modeling Fitting the semi-empirical model requires tuples of $(Q_\uparrow, A, S, G)$ spanning the factorial space of geomorphic states, discharge conditions, and alluvial depths. We generated these tuples using the same HydroGeoSphere simulation model (HGS) as Chapter 2. HGS is a 3-dimensional control-volume finite element model that simulates coupled surface-subsurface flow and hyporheic exchange. The model domain spans a 3.5 km reach of the Meacham Creek floodplain, encompassing the 1.6 km restoration project and adjacent unrestored channel. We constructed the model domain using a 5 m square mesh tessellation representing floodplain stratigraphy with an alluvial layer overlying basaltic bedrock. Surface topography used 2009 LiDAR data for unrestored conditions and 2013 LiDAR data for restored conditions. We held hydraulic conductivities (400 md^{-1} for alluvium, 0.00273 md^{-1} for bedrock), boundary conditions, and material properties constant across scenarios. We set upstream discharge using flux nodal boundaries, established downstream boundaries using critical depth conditions, and increased alluvial depth in 1 m increments by lowering the bedrock boundary from its existing surface. The zero-decrement position (existing site alluvial conditions without simulated deepening) represents the as-built alluvial depth at the time of the pre- and post-restoration surveys.

Our factorial design simulated variation in $Q_{\uparrow}$ across different restoration states, discharge conditions, and aquifer storage volumes. We considered:

- the unrestored and restored states ($G \in \{0, 1\}$); thus $n_G = 2$;
- four stream discharge rates (Q, $[\mathrm{L}^3][\mathrm{T}^{-1}]$): baseflow, the 1.25-year return interval (hereafter annual flow), the 2-year return interval (bankfull), and the 5-year return interval (overbank); $n_Q = 4$;
- five values of S, corresponding to existing alluvial depth and four successive 1 m increments; $n_S = 5$

for a total of $n = n_G \times n_S \times n_Q = 40$ model scenarios. For each scenario, we determined $q_{\uparrow}$ from Equation 43, yielding 40 $(Q_{\uparrow}, q_{\uparrow}, A, G, S)$ tuples. We divided the tuples into four groups of 10 tuples, with each group representing one level of Q. We then fit Equation 38 to the $(q_{\uparrow}, S, G)$ values of each group, yielding β values for each level of stream Q.

Partitioning restoration-induced hyporheic exchange In Chapter 2, we decomposed changes in $Q_{\uparrow}$ across flow transitions within each channel using the multiplicative form of Darcy's law ($Q_{\uparrow} = A\, q_{\uparrow}$), showing that expanding the wetted streambed consistently accounted for a larger share of increased exchange than intensified flux. Here, we apply the same decomposition to the between-channel comparison, partitioning $\Delta Q_{\uparrow}$ between changes in wetted area, changes in specific discharge, and their interaction. The extension is direct: the Chapter 2 decomposition compared successive flows within one channel, whereas this decomposition compares the restored and unrestored channels at matched flow and storage conditions.

By definition, $\Delta Q_{\uparrow}$ is the difference between restored aquifer discharge ($Q_{\uparrow r} = A_r\, q_{\uparrow r}$) and unrestored aquifer discharge ($Q_{\uparrow u} = A_u\, q_{\uparrow u}$):

$$\Delta Q_{\uparrow} = A_r\, q_{\uparrow r} - A_u\, q_{\uparrow u} \tag{44}$$

Substituting $q_{\uparrow r} = \Delta q_{\uparrow} + q_{\uparrow u}$ and $A_r = \Delta A + A_u$:

$$\begin{aligned}
\Delta Q_{\uparrow} &= A_r(\Delta q_{\uparrow} + q_{\uparrow u}) - A_u q_{\uparrow u} \\
&= A_r \Delta q_{\uparrow} + A_r q_{\uparrow u} - A_u\, q_{\uparrow u} \\
&= A_r\, \Delta q_{\uparrow} + \Delta A\, q_{\uparrow u} \\
&= (\Delta A + A_u)\, \Delta q_{\uparrow} + \Delta A\, q_{\uparrow u} \\
&= \underbrace{A_u \Delta q_{\uparrow}}_{\text{intensification}} + \underbrace{\Delta A\, \Delta q_{\uparrow}}_{\text{interaction}} + \underbrace{\Delta A\, q_{\uparrow u}}_{\text{expansion}}
\end{aligned} \tag{45}$$

The three terms partition $\Delta Q_{\uparrow}$ between the streambed that both channels share (A_u) and the additional streambed that restoration created (ΔA). The intensification term ($A_u \cdot \Delta q_{\uparrow}$) is the additional exchange produced by higher specific discharge over the shared streambed. The interaction term ($\Delta A \cdot \Delta q_{\uparrow}$) captures the compound effect that arises because the new area operates at the higher restored flux rather than the unrestored flux. The expansion term ($\Delta A \cdot q_{\uparrow u}$) is the additional exchange produced by the new wetted area at the unrestored flux. The decomposition is purely definitional and requires no model assumptions.

For each level of stream Q, we use Equation 38 to apportion $\Delta \hat{q}_{\uparrow}$ among contributions from S, G, and their interaction:

$$\Delta\hat{q}_{\uparrow} = \Delta\hat{q}_{\uparrow_S} + \Delta\hat{q}_{\uparrow_G} + \Delta\hat{q}_{\uparrow_{G:S}}. \tag{46}$$

Because the intensification and interaction terms share the factor $\Delta q_{\uparrow}$, they combine as $A_r\,\Delta q_{\uparrow}$. We denote this flux-attributable portion of $\Delta Q_{\uparrow}$ as $\Delta Q_{\uparrow,\Delta q}$. The fitted coefficients β_1, β_2, and β_3 decompose $\Delta Q_{\uparrow,\Delta q}$ into contributions from storage, channel complexity, and their interaction. Because A_r is constant at any given stream Q:

$$\begin{aligned} \Delta Q_{\uparrow,\Delta q} = A_r\,\Delta\hat{q}_{\uparrow} &= A_r\Delta\hat{q}_{\uparrow_S} + A_r\Delta\hat{q}_{\uparrow_G} + A_r\Delta\hat{q}_{\uparrow_{G:S}} \\ &= \Delta\hat{Q}_{\uparrow_S} + \Delta\hat{Q}_{\uparrow_G} + \Delta\hat{Q}_{\uparrow_{G:S}} \end{aligned} \tag{47}$$

$\Delta\hat{q}_{\uparrow_S}$ is the difference in $\hat{q}_{\uparrow}$ calculated using the restored aquifer storage (S_r) vs. the unrestored aquifer storage (S_u), while holding geomorphic state constant ($G = 0$). Referencing Equation 39:

$$\begin{aligned} \Delta\hat{q}_{\uparrow_S} &= \Big(\beta_1\log(S_r) + c\Big) - \Big(\beta_1\log(S_u) + c\Big) \\ &= \beta_1(\log(S_r) - \log(S_u)) \\ &= \beta_1\Delta\log(S). \end{aligned} \tag{48}$$

Similarly, $\Delta\hat{q}_{\uparrow_G}$ is the difference in $\hat{q}_{\uparrow}$ calculated using the restored ($G = 1$) vs. unrestored ($G = 0$) geomorphic states, while holding S constant at $S = S_u$. Referencing

Equations 38 and 39:

$$\begin{aligned}\Delta\hat{q}_{\uparrow G} &= \Big(\beta_1 \log(S_u) + \beta_2 + \beta_3 \log(S_u) + c\Big) - \Big(\beta_1 \log(S_u) + c\Big) \\ &= \beta_2 + \beta_3 \log(S_u)\end{aligned} \tag{49}$$

Lastly, $\Delta\hat{q}_{\uparrow G:S}$ is the remainder of $\Delta\hat{q}_{\uparrow}$ not included in $\Delta\hat{q}_{\uparrow S}$ or $\Delta\hat{q}_{\uparrow G}$:

$$\Delta\hat{q}_{\uparrow G:S} = \Delta\hat{q}_{\uparrow} - \Delta\hat{q}_{\uparrow S} - \Delta\hat{q}_{\uparrow G} \tag{50}$$

By definition, $\Delta\hat{q}_{\uparrow}$ is

$$\begin{aligned}\Delta\hat{q}_{\uparrow} &= \hat{q}_{\uparrow r} - \hat{q}_{\uparrow u} \\ &= \Big(\beta_1 \log(S_r) + \beta_2 + \beta_3 \log(S_r) + c\Big) - \Big(\beta_1 \log(S_u) + c\Big) \\ &= \beta_1 \Delta\log(S) + \beta_2 + \beta_3 \log(S_r).\end{aligned} \tag{51}$$

Substituting for all addends in Equation 50

$$\begin{aligned}\Delta\hat{q}_{\uparrow G:S} &= \Big(\beta_1 \Delta\log(S) + \beta_2 + \beta_3 \log(S_r)\Big) - \Big(\beta_1 \Delta\log(S)\Big) - \Big(\beta_2 + \beta_3 \log(S_u)\Big) \\ &= \beta_3 \log(S_r) - \beta_3 \log(S_u) \\ &= \beta_3 \Delta\log(S).\end{aligned} \tag{52}$$

We multiply each $\Delta\hat{q}_{\uparrow i}$ (where $i \in \{S, G, G{:}\,S\}$) by either A_u or ΔA, partitioning $\Delta\hat{Q}_{\uparrow i}$ into the portion attributable to the unrestored wetted area ($\Delta\hat{Q}_{\uparrow i, A_u}$) and the portion attributable to the *additional* wetted area added by restoration ($\Delta\hat{Q}_{\uparrow i, \Delta A}$).

We arranged the resulting values into four tables, one for each stream discharge, with a column for each factor (S, G, $G : S$, A) and a row for each area component (A_u, ΔA). Each value is normalized by $\Delta\hat{Q}_{\uparrow}$ to express the contribution as a fraction of total $\Delta\hat{Q}_{\uparrow}$ (Table 7). Partitioning values are reported at the zero-decrement alluvial position, which represents existing site conditions.

Table 7: Structure of the partitioning table. Rows separate contributions by streambed area (shared vs. additional); columns separate contributions by flux factor. Each cell expresses its contribution as a percentage of total $\Delta Q_{\uparrow}$.

	$q_{\uparrow u}$	$\Delta q_{\uparrow}$
A_u	–	Contribution of $q_{\uparrow}$ ($\frac{\Delta q_{\uparrow} A_u}{\Delta Q_{\uparrow}}$)
ΔA	Contribution of A ($\frac{q_{\uparrow u}\Delta A}{\Delta Q_{\uparrow}}$)	Interaction ($\frac{\Delta q_{\uparrow}\Delta A}{\Delta Q_{\uparrow}}$)

Results

Semi-empirical model fits

The fitted model (Equation 42) achieved adjusted $R^2 = 1.00$ across all four flow conditions (Table 8). Fitted values of $Q_{\uparrow}$ track the simulation outputs closely across the full range of aquifer storage and geomorphic states (Figure 20), confirming that the combination of wetted area (A), aquifer storage (S), and channel complexity (G) captures the primary controls on $Q_{\uparrow}$ in this system.

The fitted coefficients vary systematically across flows (Table 8). The storage coefficient (β_1) remains stable (0.25–0.31), indicating that the sensitivity of specific discharge to aquifer storage changes little with discharge. The channel complexity coefficient (β_2) shifts from strongly negative at baseflow (-1.27) to slightly positive at overbank ($+0.11$), and the interaction term (β_3) shifts from strongly positive at baseflow ($+0.25$) to near zero at overbank (-0.02). The opposing signs of β_2 and β_3 at sub-overbank flows, and their convergence toward zero at overbank, indicate that channel complexity's effect on specific discharge is strongly flow-dependent.

	Model			
	Baseflow	Annual	Bankfull	Overbank
Intercept	-1.206 ± 0.041	-1.282 ± 0.018	-1.523 ± 0.030	-1.575 ± 0.015
$\log(S)$	0.260 ± 0.007	0.253 ± 0.003	0.298 ± 0.005	0.313 ± 0.003
G	-1.267 ± 0.065	-0.901 ± 0.026	-0.648 ± 0.043	0.113 ± 0.021
$\log(S)$:G	0.251 ± 0.011	0.186 ± 0.004	0.142 ± 0.007	-0.016 ± 0.004
Adjusted R^2	1.00	1.00	1.00	1.00

Table 8: Fitted coefficients of the semi-empirical model (Equation 42) for each flow condition; standard errors are in parentheses.

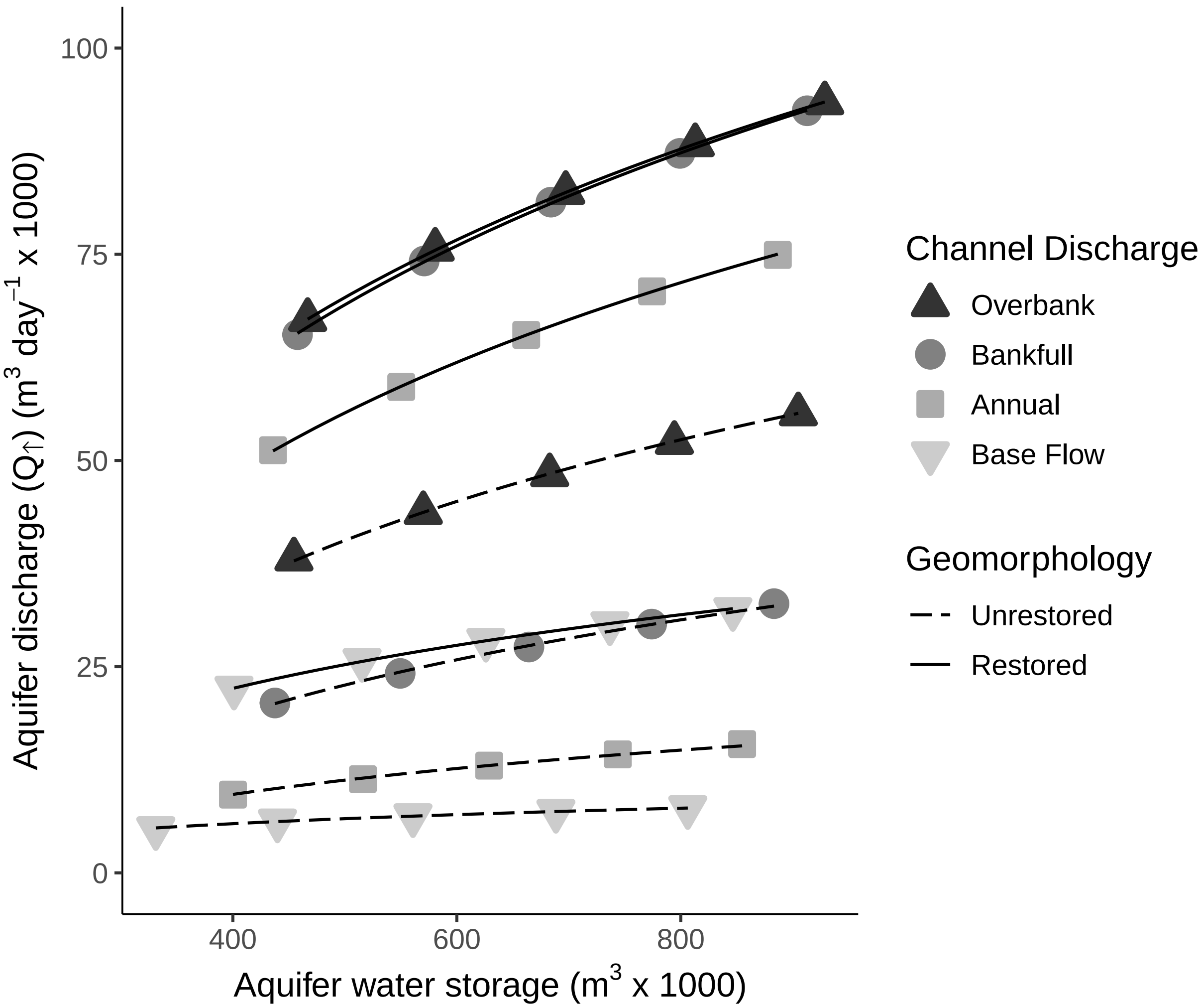

Figure 20: Simulated aquifer discharge ($Q_{\uparrow}$) versus aquifer storage (S) for unrestored and restored states at each stream discharge rate. Points are simulation outputs from the factorial design; lines are fitted values from Equation 42.

<u>Partitioning of $\Delta Q_{\uparrow}$</u>

Restoration consistently enhanced aquifer discharge across all flow conditions and storage scenarios. The partitioning tables (Tables 9–12) and Figure 21 decompose $\Delta Q_{\uparrow}$ by factor and by area, revealing two principal patterns.

First, expanding the exchange interface accounts for the largest share of $\Delta Q_{\uparrow}$ at every flow. The ΔA row (expansion plus interaction terms) ranges from 53.9% at bankfull to 81.6% at overbank, with the expansion term alone ($\Delta A \cdot q_{\uparrow u}$) contributing 26.9–71.5% depending on flow. The expansion term is largest at overbank (71.5%), where floodplain inundation recruits the widest additional streambed. At bankfull, the ΔA row reaches its minimum because the unrestored channel has expanded within its levees, increasing A_u and shifting more of $\Delta Q_{\uparrow}$ into the intensification column.

Second, channel complexity (G) is the most flow-variable factor, ranging from 25.2% of $\Delta Q_{\uparrow}$ at overbank to 69.4% at bankfull. At bankfull, the G contribution is distributed across both the shared streambed (A_u: 43.8%) and the additional restored area (ΔA: 25.6%). At overbank, the G contribution drops sharply, consistent with the near-zero values of β_2 and β_3 at that flow. The shift between these two conditions reflects a change in both the flux difference between channels and the area of streambed over which that difference acts. Pool-riffle pressure variations are strongest when flow depth is comparable to bedform amplitude; at overbank, deep submergence dampens these variations and collapses the flux difference between channels.

Alluvial depth (S) and the storage-complexity interaction ($G{:}S$) together account for 3–13% of $\Delta Q_{\uparrow}$ across flows, with the largest contributions at baseflow (7.4% and 5.8%, respectively) and the smallest at bankfull and overbank. The interaction term effectively vanishes at overbank (−0.04%).

Total $\Delta Q_{\uparrow}$ increased from approximately 40,000 $m^3\ day^{-1}$ at baseflow to 60,000 $m^3\ day^{-1}$ at overbank (Figure 21). Although the percentage share of the exchange interface is smallest at bankfull, the absolute magnitude of $\Delta Q_{\uparrow}$ from all factors increases with discharge because both A and $q_{\uparrow}$ increase.

	Aquifer Discharge ($\Delta Q_{\uparrow}$) by Factor				
	$q_{\uparrow A}$	$\Delta q_{\uparrow S}$	$\Delta q_{\uparrow G}$	$\Delta q_{\uparrow G:S}$	
Attributable to:	Area	Storage (S)	Complexity (G)	G:S Interaction	Total by Area
Unrestored A (A_u)	–	3.0%	16.8%	2.9%	22.2%
Additional A (ΔA)	45.7%	4.4%	24.3%	3.4%	77.8%
Restored A (A_r)	45.7%	7.4%	41.2%	5.8%	100.0%

Table 9: Baseflow partitioning of $\Delta Q_{\uparrow}$ by factor, at existing site conditions (zero decrement). Values are percentages of total $\Delta Q_{\uparrow}$ at matched storage.

	Aquifer Discharge ($\Delta Q_{\uparrow}$) by Factor				
	$q_{\uparrow A}$	$\Delta q_{\uparrow S}$	$\Delta q_{\uparrow G}$	$\Delta q_{\uparrow G:S}$	
Attributable to:	Area	Storage (S)	Complexity (G)	G:S Interaction	Total by Area
Unrestored A (A_u)	–	1.4%	23.3%	1.1%	25.8%
Additional A (ΔA)	34.8%	2.1%	35.7%	1.6%	74.2%
Restored A (A_r)	34.8%	3.5%	59.0%	2.7%	100.0%

Table 10: Annual flow partitioning of $\Delta Q_{\uparrow}$ by factor, at existing site conditions (zero decrement). Values are percentages of total $\Delta Q_{\uparrow}$ at matched storage.

	Aquifer Discharge ($\Delta Q_{\uparrow}$) by Factor				
	$q_{\uparrow A}$	$\Delta q_{\uparrow S}$	$\Delta q_{\uparrow G}$	$\Delta q_{\uparrow G:S}$	
Attributable to:	Area	Storage (S)	Complexity (G)	G:S Interaction	Total by Area
Unrestored A (A_u)	–	1.4%	43.8%	0.9%	46.1%
Additional A (ΔA)	26.9%	0.8%	25.6%	0.5%	53.9%
Restored A (A_r)	26.9%	2.3%	69.4%	1.4%	100.0%

Table 11: Bankfull partitioning of $\Delta Q_{\uparrow}$ by factor, at existing site conditions (zero decrement). Values are percentages of total $\Delta Q_{\uparrow}$ at matched storage.

	Aquifer Discharge ($\Delta Q_{\uparrow}$) by Factor				
	$q_{\uparrow A}$	$\Delta q_{\uparrow S}$	$\Delta q_{\uparrow G}$	$\Delta q_{\uparrow G:S}$	
Attributable to:	Area	Storage (S)	Complexity (G)	G:S Interaction	Total by Area
Unrestored A (A_u)	–	2.1%	16.3%	-0.03%	18.4%
Additional A (ΔA)	71.5%	1.2%	8.9%	-0.01%	81.6%
Restored A (A_r)	71.5%	3.3%	25.2%	-0.04%	100.0%

Table 12: Overbank partitioning of $\Delta Q_{\uparrow}$ by factor, at existing site conditions (zero decrement). Values are percentages of total $\Delta Q_{\uparrow}$ at matched storage.

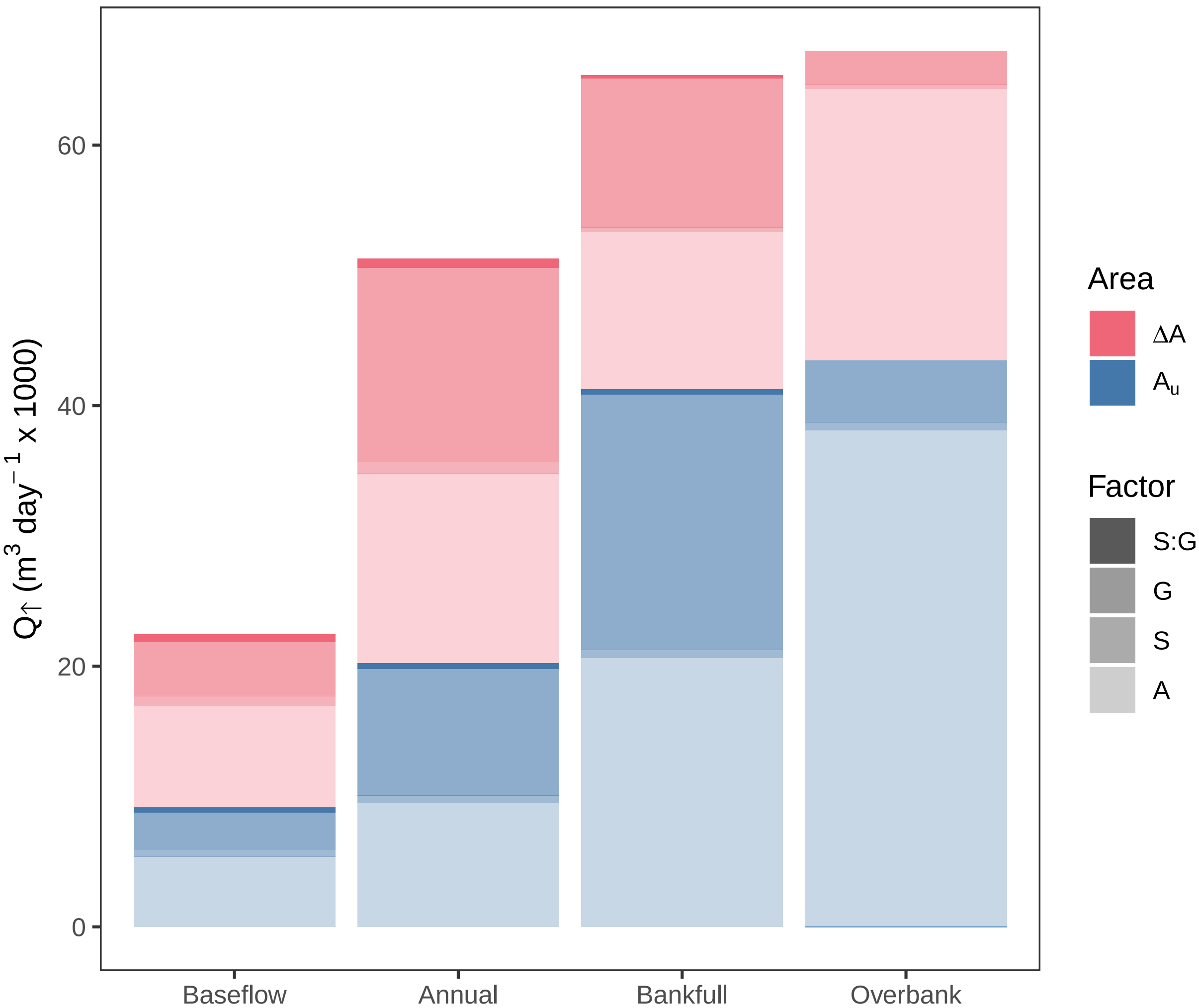

Figure 21: Partitioning of aquifer discharge ($Q_{\uparrow}$) for each flow condition. Stacked bars show absolute contributions (m^3 day^{-1} $\times$ 1000) from unrestored area (A_u), additional area from restoration (ΔA), storage (S), channel complexity (G), and storage-complexity interaction ($G : S$).

Discussion

Physical interpretation of the semi-empirical model

The model's Darcy form, $\hat{Q}_{\uparrow} = A\hat{q}_{\uparrow}$, separates wetted area from the processes that govern flux through the streambed. The fitted coefficients (Table 8; Figure 20) reveal how those processes shift across flows and between geomorphic states.

For the unrestored channel ($G = 0$), Equation 38 reduces to

$$\hat{q}_{\uparrow} = \beta_1 \log(S) + c,$$

so that specific discharge increases with the logarithm of aquifer storage. The logarithmic form has a physical basis: in bedrock-bounded systems, bedform-induced pressure fields decay with depth below the streambed, so each successive increment of alluvial depth steepens hydraulic gradients less than the one before, even as it adds the same volume of storage (Chapter 2; [84]). The $\log(S)$ form captures these diminishing returns. The sensitivity of specific discharge to storage is nearly constant across flows ($\beta_1 = 0.25$–0.31; Table 8), indicating that this relationship depends primarily on the geometry of the pressure field rather than on discharge magnitude.

For the restored channel ($G = 1$), the equation becomes

$$\hat{q}_{\uparrow} = (\beta_1 + \beta_3) \log(S) + (\beta_2 + c).$$

Specific discharge still increases logarithmically with storage, but the relationship shifts. Two new coefficients enter. β_2 adjusts the baseline: it is the difference in predicted $q_{\uparrow}$ between restored and unrestored geomorphologies when other terms are held equal, and it reflects how the change in channel morphology alone alters specific discharge. β_3 adjusts the storage sensitivity: it is the additional increment of $q_\uparrow$ per unit $\log(S)$ gained (or lost) under restored conditions, and it reflects whether the restored morphology extracts more or less gradient from a given increase in alluvial depth than the unrestored channel does.

The influence of channel complexity on specific discharge varies systematically across the hydrograph, as reflected in the fitted values of β_2 and β_3 (Table 8). From baseflow through bankfull, β_2 is negative (-1.27 to -0.65) and β_3 is positive ($+0.14$ to $+0.25$). The negative β_2 means that, all else equal, switching from the unrestored to the restored morphology initially lowers the predicted specific discharge. This is consistent with the character of the restored channel: its wider cross section wets more low-gradient surfaces at any given flow, pulling the spatial average of $q_\uparrow$ downward. The positive β_3 means that the restored channel recovers this deficit as alluvial depth increases, and it does so faster than the unrestored channel. This too has a physical basis. The deeper, higher-amplitude bedforms and greater sinuosity of the pool-riffle channel impose larger head differences (Δh) than the plane-bed channel, but those larger head differences require more alluvial depth to fully develop. Where alluvium is shallow, bedrock truncates the restored channel's deeper pressure field more severely than it truncates the shallower pressure field of the plane-bed channel. As alluvial depth increases, the pool-riffle morphology's capacity to steepen gradients is more fully expressed, and by the alluvial depths present at Meacham Creek the restored channel's specific discharge exceeds the unrestored channel's at all sub-overbank flows (Figure 20).

At overbank flow, the coefficient pattern reverses. β_2 turns slightly positive ($+0.11$) and β_3 approaches zero (-0.02). The restored channel no longer starts at a deficit that alluvial depth must overcome; instead, it predicts modestly higher specific discharge than the unrestored channel regardless of storage. The shift is consistent with the submergence effect described by [84]: as flow depth increases well beyond bedform amplitude, the near-bed pressure variations that drive vertical exchange are dampened. At overbank flow, both channels are deeply submerged, and bedform-scale pressure differences contribute little to the spatial variation in $q_{\uparrow}$. The storage sensitivity of both channels converges ($\beta_1 + \beta_3 \approx \beta_1$) because the pressure fields being truncated by bedrock are themselves already diminished by submergence. What remains is a small, uniform contribution from sinuosity-driven lateral exchange, which persists because meander-bend head differences are set by planform geometry rather than by bedform relief.

The model partitions two physically distinct controls on specific discharge: a storage-gradient relationship that is stable across flows (β_1), and a channel-complexity perturbation that is strongly flow-dependent (β_2, β_3). The storage-gradient relationship (captured by β_1) operates through the same pressure-field mechanism regardless of flow or geomorphic state. Channel complexity enters as a perturbation to that relationship: β_2 shifts the baseline and β_3 modifies the storage sensitivity. That perturbation is strongly flow-dependent because the mechanisms through which pool-riffle morphology generates head differences (bedform relief, partial submergence, sinuosity) respond differently to increasing discharge. The coefficient patterns foreshadow the partitioning results: the exchange interface (A) accounts for the largest share of $\Delta Q_{\uparrow}$ at flows where β_2 and β_3 are small or offsetting, while channel complexity (G) contributes most at flows where the baseline shift and heightened storage sensitivity compound to produce large differences in $q_{\uparrow}$.

Partitioning restoration effects on hyporheic exchange

The area and flux decompositions (Equations 45 and 46) locate every parcel of $\Delta Q_{\uparrow}$ along two dimensions: whether it occurs over the shared or additional streambed, and whether it traces to area expansion, alluvial depth, channel complexity, or their interaction. The subsections that follow trace how each restoration outcome's contribution shifts across the hydrograph, and why.

<u>The exchange interface</u> Expanding wetted streambed area consistently accounts for the largest share of $\Delta Q_{\uparrow}$ across the hydrograph (Tables 9–12; Figure 21). Removing levees, designing a wider sinuous pool-riffle channel, and reconnecting the floodplain exposed new streambed to exchange. Even if the flux through that new streambed were identical to the unrestored channel's, the additional area alone would produce a substantial increase in $Q_{\uparrow}$ [15]. This is consistent with the Chapter 2 finding that expanding A was the single largest contributor to increased $Q_{\uparrow}$ across flow transitions within each channel. The contrasting at-a-station hydraulic geometry of the two channels explains why. The restored channel's wider, lower cross section spreads the discharge response across width, recruiting new exchange surface over a broad range of sub-bankfull flows. The confined plane-bed channel concentrates the same discharge increase in stage [29, 33, 49]. The area effect dips at bankfull because the unrestored channel has filled within its levees: a larger A_u shifts more of the same flux difference onto the shared streambed, where it registers in the intensification column rather than in ΔA.

<u>Channel complexity</u> The contribution of channel complexity to $\Delta Q_{\uparrow}$ varies more across the hydrograph than any other factor (Tables 9–12). The variation reflects less a change in the flux difference between channels than a change in the area of streambed over which that difference acts.

Channel complexity contributes the most at bankfull because the flux difference between channels compounds across large wetted areas in both the shared and additional streambed (Table 11). The restored channel still maintains meaningful ΔA because its wider, lower cross section had already recruited bar surfaces, point-bar margins, and shallow channel edges at lower flows (Chapter 2). The flux difference from pool-riffle morphology ($\Delta q_{\uparrow_G}$), acting across both A_u and ΔA, accounts for more than two-thirds of the total restoration effect. A moderate difference in specific discharge, compounded over large wetted areas, produces a disproportionate share of $\Delta Q_{\uparrow}$.

At baseflow, channel complexity still accounts for a substantial share, but the balance shifts. Here A_u is small because the plane-bed channel confines flow to a narrow wetted width, so most of the G effect acts over the additional restored area, where it compounds with the expansion term.

At overbank flow, the contribution drops sharply. As flow depth increases well beyond bedform amplitude, submergence dampens the near-bed pressure variations that generate the pool-riffle channel's higher $q_{\uparrow}$ at lower flows [11, 84]. Above bankfull, the at-a-station hydraulic geometry framework no longer applies [29] and floodplain connectivity becomes the relevant area control (Chapter 2). Both channels have recruited most of their available exchange surface, and the flux difference between them has largely collapsed. What remains likely reflects sinuosity-driven lateral exchange [12, 22, 70], which scales with planform geometry rather than bedform amplitude.

Alluvial depth and the storage-complexity interaction Alluvial depth (S) and its interaction with channel complexity ($G{:}S$) together account for the smallest contributions in the partitioning across all flows (Tables 9–12), but they reflect a physically important control: the depth of alluvium above bedrock determines how fully the geomorphic pressure field develops into hydraulic gradients.

The storage term ($\Delta q_{\uparrow S} = \beta_1 \Delta \log(S)$) is modest because the difference in $\log(S)$ between channels at matched alluvial positions is itself modest. The restoration increased effective alluvial depth by repositioning the channel onto the floodplain surface rather than through aggradation, and the resulting storage difference is smaller in relative terms than the differences in area or morphology.

Though small in the partitioning, alluvial depth reflects a constraint that the other factors do not share. A practitioner can widen a channel, construct pool-riffle sequences, or remove levees, but the depth to bedrock at a given site is fixed. In Chapter 2, we distinguished structural storage (the permanently saturated volume set by alluvial depth) from dynamic storage (the variably saturated volume that responds to stream discharge). The partitioning tables report at existing site conditions, where only the between-channel difference in structural storage contributes to ΔS. The physical importance of alluvial depth is larger than its percentage suggests: as established above, shallow alluvium truncates the restored channel's deeper pressure field, capping the gradients that pool-riffle morphology can express.

The truncation is visible in the interaction term: β_3 is largest at baseflow, where the restored channel's pressure field has the most unrealized depth, and collapses at overbank, where submergence has already dampened the pressure fields that additional alluvium would amplify.

Conclusions

Findings Summary

In Chapter 2, the multiplicative decomposition of $Q_{\uparrow} = A\, q_{\uparrow}$ separated the restoration effect into area expansion and gradient intensification but did not identify what produced the flux differences between channels. The partitioning developed here answers that question: it attributes $\Delta Q_{\uparrow}$ to the exchange interface, channel complexity, and alluvial depth, and shows that their relative contributions shift systematically with discharge. The shift is not a sequence of discrete regimes in which one factor dominates and others switch off. It is a continuous rebalancing driven by three physical pathways that have different relationships to discharge: cross-section geometry governs how rapidly the exchange interface expands with stage, bedform submergence governs how strongly channel complexity generates flux differences, and the depth to bedrock governs how fully those flux differences propagate into the subsurface.

The fitted coefficients connect these pathways to the partitioning results. The storage sensitivity (β_1) is stable across flows, indicating that the relationship between alluvial depth and hydraulic gradients is a property of the pressure-field geometry rather than of discharge. The channel complexity coefficients (β_2, β_3) vary systematically, shifting from strongly opposing signs at within-bank flows to near zero at overbank, consistent with submergence damping of near-bed pressure variations. Because the model predicts $Q_{\uparrow}$ as the product of wetted area and a specific discharge equation whose coefficients map to storage, complexity, and their interaction, the partitioning percentages trace to physical processes rather than to statistical artifacts. The partitioning therefore informs restoration design: the factors that matter most at a given flow are predictable from the geomorphic setting and the discharge regime.

Design Implications

The partitioning offers practical guidance for restoration designs that target hyporheic exchange. Because expanding the exchange interface accounts for the largest share of $\Delta Q_{\uparrow}$ at every flow, design actions that widen the channel and reconnect the floodplain yield the most consistent returns across the hydrograph. The mechanism is specific: a wider cross section produces a width-dominated stage response that recruits new exchange surface across sub-bankfull flows, whereas a confined cross section concentrates the same discharge increase in stage. Restoration designs that achieve this cross-section geometry, whether through levee removal, channel realignment, or floodplain grading, produce a persistent increase in exchange area that compounds with any concurrent change in morphology or storage.

Channel complexity contributes most at intermediate flows, where the higher flux generated by pool-riffle morphology acts over large wetted areas in both the shared and additional streambed. For projects where baseflow and bankfull exchange matter most, for instance where cold-water refugia or nutrient processing during summer low flows are priorities [41], investing in morphological heterogeneity yields substantial returns. At overbank flows, submergence dampens those same pressure variations, and the exchange interface carries most of the restoration effect regardless of morphology.

Alluvial depth is the one factor constrained by geology and geomorphic setting rather than by engineering, but incision can reduce effective alluvial depth well below the geomorphic potential of a site. Where past degradation has lowered the streambed toward bedrock, strategies that promote aggradation, such as grade control structures, beaver dam analogs [61], or the strategic channel realignment employed at Meacham Creek, can recover lost alluvial depth and with it the capacity for the geomorphic pressure field to develop steeper gradients [84]. The partitioning results suggest that such recovery matters most where it enables channel complexity to express itself: the storage-complexity interaction (β_3) is largest at within-bank flows, meaning that restoring alluvial depth allows pool-riffle morphology to express steeper gradients. At sites where alluvium is already deep relative to bedform amplitude, further increases yield diminishing returns on exchange, and design effort is better directed toward the exchange interface and channel complexity. The geologic setting ultimately limits what aggradation can achieve, but in incised systems the gap between current and potential alluvial depth represents recoverable hyporheic capacity.

Limitations

Three limitations of our analysis merit consideration. First, the binary geomorphic state variable (G) resolves the collective effect of switching from plane-bed to pool-riffle morphology but cannot distinguish among the individual contributions of bedform amplitude, pool spacing, sinuosity, and cross-section shape. The coefficient patterns are consistent with mechanisms identified in the hyporheic exchange literature, but applying the partitioning framework to sites with different morphological contrasts would require refitting the model rather than transferring the Meacham Creek coefficients directly. Replacing G

with continuous morphometric variables in a factorial design that varies bedform amplitude, sinuosity, and pool spacing independently would resolve these individual contributions, but such a design requires substantially more simulation scenarios than the binary comparison presented here.

Second, our steady-flow experimental design likely underestimates the importance of alluvial depth for annual hyporheic function. Under transient conditions, flood pulses drive water deeper into the alluvium and temporarily expand the hyporheic zone, producing exchange fluxes and residence times that vary far more than the steady-state pressure field alone would predict [38, 88]. Individual discharge events can increase the reactive efficiency of the hyporheic zone by flushing solutes through flow paths that are inactive at baseflow [85]. Aquifer storage buffers these pulses between events (the dynamic storage response described in Chapter 2), and the seasonal patterns of filling and draining that this buffering produces were not captured in our simulations. The 2–7% contribution attributed to alluvial depth in the partitioning reflects its effect on gradients at steady state; its role in sustaining exchange between events, and in mediating the depth and duration of transient hyporheic flow paths, is a separate and potentially larger contribution that future work incorporating unsteady flow would need to assess.

Third, the model fits (adjusted $R^2 = 1.00$) reflect the controlled nature of numerical simulations with known boundary conditions, uniform hydraulic properties, and no measurement error. Field application would introduce heterogeneity in alluvial properties, uncertainty in wetted area delineation, and variability in bedrock topography that the current framework does not account for. Whether the log-linear relationship between $q_{\uparrow}$ and S holds under these conditions, and whether the partitioning percentages are robust to observational noise, remain to be tested.

Broader significance

Restoration projects rarely permit unconstrained design. Infrastructure, land ownership, regulatory requirements, and budgets limit the palette of available interventions at any given site. The partitioning framework developed here offers a way to evaluate these tradeoffs in terms of hyporheic outcomes. By identifying which restoration outcome carries the most weight at the flows that matter for a project's ecological objectives, practitioners can direct limited design resources where they will produce the largest hyporheic returns. At Meacham Creek, for example, floodplain reconnection delivered the most consistent gains across the hydrograph, while channel complexity mattered most at the intermediate flows relevant to summer baseflow habitat. A different site with different constraints and objectives might arrive at a different priority, but the framework for making that evaluation is transferable even where the specific coefficients are not. Applying the framework at another site requires comparing restored and unrestored conditions through a parametric model fitted to factorial variation in storage and geomorphic state. In practice, the necessary inputs are routinely available: restoration projects generate topographic and bathymetric surveys for both existing and design conditions, and hydrogeologic simulation tools can produce the factorial tuples from those surveys. The approach has precedent in the principle of similitude that underlies hydraulic geometry and other scaling exercises in hydrology, where parametric relationships fitted at one site transfer through their structural form even when site-specific coefficients must be refit. The specific coefficients reported here reflect Meacham Creek's geology, morphology, and flow regime, but the model structure and the partitioning logic it supports are not bound to this site.

CONCLUSION

Synthesis

The introduction to this dissertation identified three gaps separating hyporheic process research from restoration practice. No established basis existed for applying temperature-based analytical methods to floodplain-scale flow paths. No framework existed for quantifying how much restoration changes hyporheic exchange across the hydrograph. And no means existed for attributing that change to specific design outcomes. The three studies presented here address these gaps in sequence and build on one another.

Chapter 1 established where temperature-based methods reliably characterize floodplain aquifer properties and built the simulation platform that Chapters 2 and 3 extended to the restoration problem. Chapter 2 quantified the restoration effect and separated it into area expansion and gradient intensification, revealing the diminishing-returns constraints that shape both. Chapter 3 attributed the flux differences between restored and unrestored channels to the exchange interface, channel complexity, and alluvial depth, showing that their relative contributions shift systematically with discharge.

Together, the three studies build a chain from measurement to attribution. Chapter 1's methods characterize subsurface transport at a restoration site. Chapter 2's decomposition quantifies how much exchange changes across the hydrograph. Chapter 3's partitioning identifies which design outcomes produced the change and at which flows. Each step rests on Darcy's law, preserves physical interpretability, and connects directly to the geomorphic variables that restoration projects modify.

The practitioner perspective

The questions that motivated this dissertation arose from restoration practice. Practitioners reshape channels and floodplains to recover hyporheic function, but evaluating whether a design achieved its subsurface objectives, and why, has required tools that did not exist. The framework developed here provides them.

Chapter 1 addresses the most basic practical need: characterizing subsurface transport at a restoration site using data that monitoring programs already collect. The proximal zone concept identifies where in the floodplain temperature-based estimates of aquifer properties remain reliable, and where vertical heat losses degrade them. Practitioners gain a physical basis for monitoring well placement and for interpreting the annual temperature records that restoration projects routinely generate.

The decomposition answers the next question: how much did exchange change? By separating aquifer discharge into wetted area and specific discharge, the Chapter 2 decomposition locates the restoration effect along two axes and tracks how their balance shifts across the hydrograph. A practitioner measuring increased exchange after a project can distinguish how much of the gain came from wetting more streambed versus driving water into the alluvium more intensely, and can anticipate how that balance shifts between summer baseflow and winter high water.

The partitioning answers the question that follows: which design outcomes produced the gain? Chapter 3's attribution of the flux differences to the exchange interface, channel complexity, and alluvial depth tells a practitioner which lever carried the most weight at the flows relevant to a project's ecological objectives. At Meacham Creek, floodplain reconnection delivered the most consistent returns, while channel complexity mattered most at intermediate flows relevant to summer habitat. A different site would yield different percentages, but the partitioning framework transfers even where the coefficients do not.

The geomorphic controls that govern exchange are themselves coupled through power laws. At a station, wetted width, depth, and velocity each scale with discharge as power functions whose exponents reflect cross-section shape and roughness [33, 48, 49]. Restoration changes those exponents: a wider, shallower restored channel wets more streambed per unit increase in discharge than the incised channel it replaced. The Chapter 2 area limit expresses this hydraulic geometry directly. Below the streambed, Poole et al. [64] showed that storage, exchange rate, and residence time in hyporheic zones are linked through power-law age distributions, extending the same scaling framework into the subsurface. The Darcy flux that Chapter 3 models reflects an analogous multiplicative coupling between conductivity and gradient, both governed by geomorphic boundary conditions. Refitting the Chapter 3 model as a power law would convert site-specific increments to portable restoration ratios, aligning the model with the multiplicative structure of the underlying system. The partition structure would survive unchanged, and the multiplicative form would open a route from mass exchange ratios to dimensionless relationships for thermal and solute transport.

From mass to energy

The three chapters characterize how much water cycles through the subsurface and how restoration changes that cycling. But water carries thermal energy, and the same variables that control mass exchange control the thermal budget of the stream–aquifer system through three physical levers.

First, increased hyporheic flux (the $q_{\uparrow}$ that Chapter 3 models) sets the rate at which thermal energy enters the aquifer. More pool-riffle structure and steeper near-bed pressure gradients drive more water through the subsurface, increasing the thermal current between stream and aquifer.

Second, increased aquifer volume enlarges the thermal capacitance of the system [6, 35]. The total energy a floodplain aquifer can absorb per degree of temperature change scales with the volume of saturated alluvium and the volumetric heat capacity of the matrix ($C_{thermal} = \rho c \cdot V$). For saturated gravel-bed alluvium, the bulk volumetric heat capacity is the porosity-weighted average of the water and mineral fractions, yielding $\rho c \approx 2.5$–3.0 MJ/m^3/°C for typical streambed porosities [68, 76]. Aggradation, water table rise, and floodplain reconnection all enlarge this volume.

Third, the residence time distribution determines how completely each water parcel equilibrates toward ambient aquifer temperature before returning to the channel. How far a parcel's temperature shifts depends on a thermal Péclet number: the ratio of advective to conductive heat transport along the flow path [23, 52]. When this ratio is large, conduction brings the water to aquifer temperature before it returns to the stream. When it is small, the water retains most of its original thermal signal. Marzadri et al. [56] showed that stream morphology controls this balance, with larger bedforms producing longer residence times and more thermally equilibrated return flows.

Over a year, the stream charges the aquifer thermally in summer and draws on that stored energy in winter. Restoration changes both the rate of energy delivery (through $q_{\uparrow}$) and the capacity of the store (through aquifer volume). The mass exchange framework developed in Chapters 2 and 3 already quantifies these variables and attributes their changes to specific design outcomes. Extending that framework to thermal predictions requires coupling the mass partitioning to an energy balance, not building a new conceptual structure.

Recent field observations underscore the need for this extension. Flitcroft et al. [1] reported that stream temperatures at Stage 0 restoration sites in western Oregon were warmer than expected post-restoration, with daily maxima exceeding predicted unrestored values by up to 4°C at one site. The authors identified increased solar exposure and dam operations as contributing factors but lacked a subsurface energy framework to interpret the results. The thermal capacitance and energy delivery framework described above suggests that some warming is a predictable consequence of restoration. Spreading flow across a wider, shallower surface increases atmospheric thermal loading and simultaneously enlarges the volume of alluvium available to absorb and later release that energy. Whether restoration produces net warming or cooling at a given site depends on the balance between surface energy input and subsurface thermal storage, a balance the partitioning framework is designed to resolve.

The dimensional analysis tools for this extension already exist. Tonina and Buffington [84] applied Buckingham Pi analysis to derive dimensionless predictions of hyporheic exchange depth and residence time from morphometric variables in pool-riffle channels. Huang and Chui [42] extended and validated those relationships across a broader range of channel conditions. These dimensionless frameworks relate mass exchange to the same geomorphic variables (bedform geometry, alluvial depth, Reynolds number) that the Chapter 3 partitioning resolves. Coupling the mass exchange partitioning to the advection-diffusion framework of Luce et al. [52] would close the loop between geomorphic design, mass exchange, and thermal outcome. The power-law refit described above is the natural entry point: the multiplicative form of the restoration effect maps directly onto the products of dimensionless groups that Buckingham Pi analysis yields.

The infrastructure for this work exists. A thermal HGS model of the Meacham Creek site is operational with preliminary results confirming the coupling between mass exchange and thermal outcomes. One Chapter 1 question requires more than heuristic simulations: how much does floodplain heterogeneity erode the 1D approximation at a real site? Rotating the calibration through the Meacham Creek wells, one held out per pass, would allocate the error directly. The questions are defined, the methods identified, and the data in hand.

<u>Research products</u>

Four products of this work will be released with DOIs as independently citable resources. The `temperheic` R package implements the Luce et al. [52] closed-form solutions for 1D heat transport, with the Luce et al. [53] fitting updates; the package is Chapter 1's method made operational. The Meacham Creek floodplain temperature database compiles five years of monitoring well records, with co-located surface water temperatures, from the restoration site. The HGS model repository carries the input grids, boundary conditions, and parameterization for every simulation in this dissertation, including the operational thermal model.

Three frontiers extend beyond the conditions Meacham Creek represents. Deeper alluvium would lengthen residence times and the thermal capacitance that buffers winter temperatures. Transient hydrographs would mobilize storage and release dynamics that steady-flow simulations suppress; bank storage and floodplain inundation reorganize the exchange interface across rising and falling limbs. Restorations whose pre/post contrast differs from Meacham Creek's incision-to-reconnection step would test whether the partitioning coefficients transfer or the framework itself requires revision.

The introduction to this dissertation asked how restoration changes hyporheic exchange and through what physical mechanisms. The three studies answer that question for one site across the hydrograph, and in doing so build a framework that extends beyond it. The decomposition and partitioning are grounded in Darcy's law and the geomorphic variables that govern hyporheic exchange; the methods and analytical structure transfer to any bedrock-bounded alluvial system where restoration modifies those variables. What remains is the thermal problem that motivated this work from the beginning: connecting the mass exchange framework to the energy balance that ultimately governs the stream's capacity to support cold-water habitat. The path to that connection runs through the tools this dissertation developed.

REFERENCES

[1] Rehabilitating valley floors to a stage 0 condition: A synthesis of opening outcomes. *Frontiers in Environmental Science*, 10, 7 2022. ISSN 2296665X. doi: 10.3389/fenvs.2022.892268.

[2] Mary P Anderson. Heat as a ground water tracer. *Ground Water*, 43(6):951–968, 2005. ISSN 0017-467X. doi: 10.1111/j.1745-6584.2005.00052.x. URL http://www.ncbi.nlm.nih.gov/pubmed/16324018.

[3] C. Andrus and J. Middel. Meacham Creek Watershed Analysis and Action Plan. 2003.

[4] Aquanty. *HydroGeoSphere User Manual*. Waterloo, Ont, 2015.

[5] Aquanty Inc. HGS Reference Manual, 2025. URL https://hydrogeosphere.blob.core.windows.net/hydrogeosphere/hgs/hydrosphere_ref.pdf.

[6] Alicia S Arrigoni, Geoffrey C Poole, Leal a K Mertes, Scott J O'Daniel, William W Woessner, and Steven a Thomas. Buffered, lagged, or cooled? Disentangling hyporheic influences on temperature cycles in stream channels. *Water Resources Research*, 44(9): 1–13, 9 2008. ISSN 0043-1397. doi: 10.1029/2007WR006480. URL http://www.agu.org/pubs/crossref/2008/2007WR006480.shtml.

[7] H.H. Barnes. Roughness characteristics of natural channels U.S. Geological Survey, Water Supply Paper 1849. Technical report, 1967. URL https://pubs.usgs.gov/publication/wsp1849.

[8] Jacob Bear and Alexander H.D. Cheng. *Modeling Groundwater Flow and Contaminant Transport*. Springer-Verlag, 2010. ISBN 978-1-4020-6682-5.

[9] Timothy J. Beechie, David A. Sear, Julian D. Olden, George R. Pess, John M. Buffington, Hamish Moir, Philip Roni, and Michael M. Pollock. Process-based Principles for Restoring River Ecosystems. *BioScience*, 60(3):209–222, 3 2010. ISSN 0006-3568. doi: 10.1525/bio.2010.60.3.7. URL http://www.jstor.org/stable/10.1525/bio.2010.60.3.7.

[10] Kyle W. Blasch, Jim Constantz, and David A. Stonestrom. Thermal Methods for Investigating Ground-Water Recharge. Professional Paper 1703, United States Geological Survey, 2007. URL http://pubs.er.usgs.gov/publication/pp17031.

[11] F. Boano, J. W. Harvey, A. Marion, A. I. Packman, R. Revelli, L. Ridolfi, and A. Wörman. Hyporheic flow and transport processes: Mechanisms, models, and biogeochemical implications. *Reviews of Geophysics*, 52(4):603–679, 12 2014. ISSN 87551209. doi: 10.1002/2012RG000417. URL http://doi.wiley.com/10.1002/2012RG000417.

[12] Fulvio Boano, Carlo Camporeale, Roberto Revelli, and Luca Ridolfi. Sinuosity-driven hyporheic exchange in meandering rivers. *Geophysical Research Letters*, 33(18):L18406,

2006. ISSN 0094-8276. doi: 10.1029/2006GL027630. URL http://www.agu.org/pubs/crossref/2006/2006GL027630.shtml.

[13] Fulvio Boano, Roberto Revelli, and Luca Ridolfi. Reduction of the hyporheic zone volume due to the stream-aquifer interaction. *Geophysical Research Letters*, 35(9), 5 2008. ISSN 0094-8276. doi: 10.1029/2008GL033554.

[14] Fulvio Boano, Roberto Revelli, and Luca Ridolfi. Modeling hyporheic exchange with unsteady stream discharge and bedform dynamics. *Water Resources Research*, 49:4089–4099, 7 2013. ISSN 19447973. doi: 10.1002/wrcr.20322.

[15] Fulvio Boano, Roberto Revelli, and Luca Ridolfi. Modeling hyporheic exchange with unsteady stream discharge and bedform dynamics. *Water Resources Research*, 49(7): 4089–4099, 7 2013. ISSN 19447973. doi: 10.1002/wrcr.20322.

[16] Paul Dirk Bons, Boudewijn Philip van Milligen, and Philipp Blum. A general unified expression for solute and heat dispersion in homogeneous porous media. *Water Resources Research*, 49(10):6166–6178, oct 2013. ISSN 00431397. doi: 10.1002/wrcr.20488. URL http://doi.wiley.com/10.1002/wrcr.20488.

[17] A J Boulton, T Datry, T Kasahara, M Mutz, and J A Stanford. Ecology and management of the hyporheic zone: stream-groundwater interactions of running waters and their floodplains. *Journal of the North American Benthological Society*, 29:26–40, 2010. ISSN 0887-3593. doi: 10.1899/08-017.1. URL <GotoISI>://000275023500003.

[18] Martin A Briggs, Laura K Lautz, Jeffrey M McKenzie, Ryan P Gordon, and Danielle K Hare. Using high-resolution distributed temperature sensing to quantify spatial and temporal variability in vertical hyporheic flux. *Water Resources Research*, 48, 2012. ISSN 0043-1397. doi: W0252710.1029/2011wr011227. URL <GotoISI>://WOS:000300824300003.

[19] Philip Brunner and Craig T. Simmons. HydroGeoSphere: A Fully Integrated, Physically Based Hydrological Model. *Groundwater*, 50(2):170–176, 3 2012. ISSN 0017-467X. doi: 10.1111/j.1745-6584.2011.00882.x.

[20] John M. Buffington and Daniele Tonina. Hyporheic Exchange in Mountain Rivers II: Effects of Channel Morphology on Mechanics, Scales, and Rates of Exchange. *Geography Compass*, 3(3):1038–1062, 5 2009. ISSN 17498198. doi: 10.1111/j.1749-8198.2009.00225.x. URL http://doi.wiley.com/10.1111/j.1749-8198.2009.00225.x.

[21] E. R. Burns, C. F. Williams, S. E. Ingebritsen, C. I. Voss, F. A. Spane, and J. DeAngelo. Understanding heat and groundwater flow through continental flood basalt provinces: insights gained from alternative models of permeability/depth relationships for the Columbia Plateau, USA. *Geofluids*, 15(1-2):120–138, 2 2015. ISSN 14688115. doi: 10.1111/gfl.12095. URL http://doi.wiley.com/10.1111/gfl.12095.

[22] M. Bayani Cardenas. A model for lateral hyporheic flow based on valley slope and channel sinuosity. *Water Resources Research*, 45(1):W01501, 1 2009. ISSN 0043-1397. doi: 10.1029/2008WR007442. URL `http://www.agu.org/pubs/crossref/2009/2008WR007442.shtml`.

[23] M. Bayani Cardenas and John L. Wilson. Effects of current–bed form induced fluid flow on the thermal regime of sediments. *Water Resources Research*, 43(8):W08431, 2007. ISSN 0043-1397. doi: 10.1029/2007WR005844.

[24] M. Bayani Cardenas, J. L. Wilson, and V. A. Zlotnik. Impact of heterogeneity, bed forms, and stream curvature on subchannel hyporheic exchange. *Water Resources Research*, 40(8), 8 2004. ISSN 0043-1397. doi: 10.1029/2004WR003008.

[25] Damion C. Ciotti, Jared Mckee, Karen L. Pope, G. Mathias Kondolf, and Michael M. Pollock. Design Criteria for Process-Based Restoration of Fluvial Systems, 8 2021. ISSN 15253244.

[26] B. Cluer and C. Thorne. A stream evolution model integrating habitat and ecosystem benefits. *River Research and Applications*, 30(2):135–154, 2 2014. ISSN 15351459. doi: 10.1002/rra.2631.

[27] Jim Constantz and Carole L. Thomas. The Use of Streambed Temperature Profiles to Estimate the Depth, Duration, and Rate of Percolation Beneath Arroyos. *Water Resources Research*, 32(12):3597–3602, 12 1996. ISSN 00431397. doi: 10.1029/96WR03014. URL `http://doi.wiley.com/10.1029/96WR03014`.

[28] Henry Darcy. The public fountains of the city of Dijon. *Experience and Application. Paris*, 1856.

[29] S. Lawrence Dingman and Shahab Afshari. Field verification of analytical at-a-station hydraulic-geometry relations. *Journal of Hydrology*, 564:859–872, 9 2018. ISSN 00221694. doi: 10.1016/j.jhydrol.2018.07.020.

[30] D. N. Dralle, D. A. Lapides, D. M. Rempe, and W. J. Hahm. Mapping Surface Water Presence and Hyporheic Flow Properties of Headwater Stream Networks With Multispectral Satellite Imagery. *Water Resources Research*, 59(7), 2023. ISSN 0043-1397. doi: 10.1029/2022WR034169.

[31] Alexander H. Elliott and Norman H. Brooks. Transfer of nonsorbing solutes to a streambed with bed forms: Theory. *Water Resources Research*, 33(1):123–136, 1997. doi: 10.1029/96WR02784.

[32] John F. England, Timothy A. Cohn, Beth A. Faber, Jery R. Stedinger, Wilbert O. Thomas, Andrea G. Veilleux, Julie E. Kiang, and Robert R. Mason. Guidelines for determining flood flow frequency — Bulletin 17C. Technical report, 2018.

[33] R.I. Ferguson. Hydraulics and hydraulic geometry. *Progress in Physical Geography: Earth and Environment*, 10(1):1–31, 3 1986. ISSN 0309-1333. doi: 10.1177/030913338601000101. URL https://journals.sagepub.com/doi/10.1177/030913338601000101.

[34] Stuart Findlay. Importance of surface-subsurface exchange in stream ecosystems: The hyporheic zone. *Limnology and Oceanography*, 40(1):159–164, 1 1995. ISSN 0024-3590. doi: 10.4319/lo.1995.40.1.0159.

[35] S. Kathleen Fogg, Ann Marie Reinhold, Scott J. O'Daniel, Adam A. Hyman, and Geoffrey C. Poole. Thermal insulation versus capacitance: A simulation experiment comparing effects of shade and hyporheic exchange on daily and seasonal stream temperature cycles. *Hydrological Processes*, 37(9):e14973, 2023. ISSN 0885-6087. doi: 10.1002/hyp.14973.

[36] Lynn W. Gelhar, Claire Welty, and Kenneth R. Rehfeldt. A critical review of data on field-scale dispersion in aquifers. *Water Resources Research*, 28(7):1955–1974, 7 1992. ISSN 00431397. doi: 10.1029/92WR00607. URL http://doi.wiley.com/10.1029/92WR00607.

[37] Michael N. Gooseff, Steve M. Wondzell, Roy Haggerty, and Justin Anderson. Comparing transient storage modeling and residence time distribution (RTD) analysis in geomorphically varied reaches in the Lookout Creek basin, Oregon, USA. *Advances in Water Resources*, 26(9):925–937, 9 2003. ISSN 03091708. doi: 10.1016/S0309-1708(03)00105-2. URL http://linkinghub.elsevier.com/retrieve/pii/S0309170803001052.

[38] Stanley B. Grant, Ahmed Monofy, Fulvio Boano, Jesus D. Gomez-Velez, Ian Guymer, Judson Harvey, and Marco Ghisalberti. Unifying advective and diffusive descriptions of bedform pumping in the benthic biolayer of streams. *Water Resources Research*, 56 (11), 2020. doi: 10.1029/2020WR027967.

[39] C E Hatch, A T Fisher, J S Revenaugh, J Constantz, and C Ruehl. Quantifying surface water-groundwater interactions using time series analysis of streambed thermal records: Method development. *Water Resources Research*, 42:14, 2006. ISSN 0043-1397. doi: 10.1029/2005wr004787. URL <GotoISI>://000241303300003.

[40] C E Hatch, A T Fisher, C R Ruehl, and G Stemler. Spatial and temporal variations in streambed hydraulic conductivity quantified with time-series thermal methods. *Journal of Hydrology*, 389:276–288, 2010. ISSN 0022-1694. doi: 10.1016/j.jhydrol.2010.05.046. URL <GotoISI>://000280976600004.

[41] Erich T Hester and Michael N Gooseff. Moving Beyond the Banks: Hyporheic Restoration Is Fundamental to Restoring Ecological Services and Functions of Streams. *Environmental Science & Technology*, 44:1521–1525, 2010. ISSN 0013-936X. doi: 10.1021/es902988n. URL <GotoISI>://WOS:000274842000004.

[42] Peng Huang and Ting Fong May Chui. Empirical Equations to Predict the Characteristics of Hyporheic Exchange in a Pool-Riffle Sequence. *Groundwater*, 56(6):947–958, 11 2018. ISSN 17456584. doi: 10.1111/gwat.12641.

[43] Peng Huang and Ting Fong May Chui. Hyporheic Exchange in a Straight Pool-Riffle Stream With Floodplain. *Water Resources Research*, 57(7), 7 2021. ISSN 19447973. doi: 10.1029/2020WR029182.

[44] Peng Huang and Ting Fong May Chui. Hyporheic Exchange in a Straight Stream With Alternate Bars. *Water Resources Research*, 58(10), 10 2022. ISSN 19447973. doi: 10.1029/2022WR032221.

[45] John Keery, Andrew Binley, Nigel Crook, and Jonathan W.N. Smith. Temporal and spatial variability of groundwater–surface water fluxes: Development and application of an analytical method using temperature time series. *Journal of Hydrology*, 336(1-2):1–16, 3 2007. ISSN 00221694. doi: 10.1016/j.jhydrol.2006.12.003. URL `http://linkinghub.elsevier.com/retrieve/pii/S0022169406006354`.

[46] L K Lautz. Impacts of nonideal field conditions on vertical water velocity estimates from streambed temperature time series. *Water Resources Research*, 46, 2010. ISSN 0043-1397. doi: W0150910.1029/2009wr007917.

[47] L K Lautz, N T Kranes, and D I Siegel. Heat tracing of heterogeneous hyporheic exchange adjacent to in-stream geomorphic features. *Hydrological Processes*, 24: 3074–3086, 2010. ISSN 0885-6087. doi: 10.1002/hyp.7723. URL `<GotoISI>://000283089000009`.

[48] S. Lawrence, Dingman. Analytical derivation of at-a-station hydraulic–geometry relations. *Journal of Hydrology*, 334(1-2):17–27, 2 2007. ISSN 00221694. doi: 10.1016/j.jhydrol.2006.09.021.

[49] Luna Bergere Leopold and Thomas Maddock. The hydraulic geometry of stream channels and some physiographic implications. Technical report, 1953.

[50] J D Logan and V Zlotnik. The convection-diffusion equation with periodic boundary conditions. *Applied Mathematics Letters*, 8(3):55–61, 1995. ISSN 0893-9659. doi: http://dx.doi.org/10.1016/0893-9659(95)00030-T. URL `http://www.sciencedirect.com/science/article/pii/089396599500030T`.

[51] J. David Logan. *Transport Modeling in Hydrogeochemical Systems*. Springer-Verlag, New York, NY, 2001. ISBN 978-1-4419-2932-7. URL `http://link.springer.com/book/10.1007/978-1-4757-3518-5`.

[52] Charles H. Luce, Daniele Tonina, Frank Gariglio, and Ralph Applebee. Solutions for the diurnally forced advection-diffusion equation to estimate bulk fluid velocity and diffusivity in streambeds from temperature time series. *Water*

Resources Research, 49(1):488–506, 1 2013. ISSN 00431397. doi: 10.1029/2012WR012380. URL http://www.agu.org/pubs/crossref/pip/2012WR012380.shtmlhttp://doi.wiley.com/10.1029/2012WR012380.

[53] Charles H. Luce, Daniele Tonina, Ralph Applebee, and Timothy DeWeese. Was That Assumption Necessary? Reconsidering Boundary Conditions for Analytical Solutions to Estimate Streambed Fluxes. *Water Resources Research*, 53(11):9771–9790, 11 2017. ISSN 19447973. doi: 10.1002/2017WR020618.

[54] I. P. Madin and R.P. Geitgey. Oregon Department of Geology and Mineral Industries Open-File Report O-07-15, Preliminary Geologic Map of the Umatilla Basin, Morrow and Umatilla Counties, Oregon. Technical report, Oregon Department of Geology and Mineral Industries, 2007.

[55] A Marzadri, D Tonina, A Bellin, G Vignoli, and M Tubino. Semianalytical analysis of hyporheic flow induced by alternate bars. *Water Resources Research*, 46:14, 2010. ISSN 0043-1397. doi: W0753110.1029/2009wr008285. URL <GotoISI>://000280340200001.

[56] a. Marzadri, D. Tonina, and A. Bellin. Effects of stream morphodynamics on hyporheic zone thermal regime. *Water Resources Research*, 49(4):2287–2302, 4 2013. ISSN 00431397. doi: 10.1002/wrcr.20199. URL http://doi.wiley.com/10.1002/wrcr.20199.

[57] Alessandra Marzadri, Daniele Tonina, James A. McKean, Matthew G. Tiedemann, and Rohan M. Benjankar. Multi-scale streambed topographic and discharge effects on hyporheic exchange at the stream network scale in confined streams. *Journal of Hydrology*, 519:1997–2011, 11 2014. ISSN 00221694. doi: 10.1016/j.jhydrol.2014.09.076.

[58] Mark C. Mastin, Christopher P. Konrad, Andrea G. Veilleux, and Alison E. Tecca. Magnitude, frequency, and trends of floods at gaged and ungaged sites in Washington, based on data through water year 2014. Technical report, 2016.

[59] A. M. McCallum, M. S. Andersen, G. C. Rau, and R. I. Acworth. A 1-D analytical method for estimating surface water-groundwater interactions and effective thermal diffusivity using temperature time series. *Water Resources Research*, 48(11):n/a–n/a, nov 2012. ISSN 00431397. doi: 10.1029/2012WR012007. URL http://doi.wiley.com/10.1029/2012WR012007.

[60] D R Montgomery and J M Buffington. Channel-reach morphology in mountain drainage basins. *Geological Society of America Bulletin*, 109:596–611, 1997. ISSN 0016-7606. doi: 10.1130/0016-7606(1997)109<0596:crmimd>2.3.co;2. URL <GotoISI>://WOS:A1997WY67100008.

[61] Michael M. Pollock, Timothy J. Beechie, Joseph M. Wheaton, Chris E. Jordan, Nick Bouwes, Nicholas Weber, and Carol Volk. Using beaver dams to restore incised stream ecosystems, 4 2014. ISSN 15253244.

[62] G C Poole, J A Stanford, S W Running, and C A Frissell. Multiscale geomorphic drivers of groundwater flow paths: subsurface hydrologic dynamics and hyporheic habitat diversity. *Journal of the North American Benthological Society*, 25:288–303, 2006. ISSN 0887-3593. URL <GotoISI>://000237891600003.

[63] G C Poole, S J O'Daniel, K L Jones, W W Woessner, E S Bernhardt, A M Helton, J A Stanford, B R Boer, and T J Beechie. Hydrologic spiralling: The role of multiple interactive flow paths in stream ecosystems. *River Research and Applications*, 24:1018–1031, 2008. ISSN 1535-1459. doi: 10.1002/rra.1099. URL <GotoISI>://000259584900010.

[64] Geoffrey C. Poole, S. Kathleen Fogg, Scott J. O'Daniel, Byron E. Amerson, Ann Marie Reinhold, Samuel P. Carlson, Elizabeth J. Mohr, and Hayley C. Oakland. Hyporheic hydraulic geometry: Conceptualizing relationships among hyporheic exchange, storage, and water age. *PLoS ONE*, 17(1 January 2022), 1 2022. ISSN 19326203. doi: 10.1371/journal.pone.0262080.

[65] Paul D. Powers, Matt Helstab, and Sue L. Niezgoda. A process-based approach to restoring depositional river valleys to Stage 0, an anastomosing channel network. *River Research and Applications*, 35(1):3–13, 1 2019. ISSN 1535-1459. doi: 10.1002/rra.3378. URL https://onlinelibrary.wiley.com/doi/abs/10.1002/rra.3378.

[66] R Core Team. R: A Language and Environment for Statistical Computing, 2023. URL https://www.R-project.org/.

[67] Gabriel C. Rau, Martin S. Andersen, and R. Ian Acworth. Experimental investigation of the thermal dispersivity term and its significance in the heat transport equation for flow in sediments. *Water Resources Research*, 48(3), 3 2012. ISSN 00431397. doi: 10.1029/2011WR011038. URL http://doi.wiley.com/10.1029/2011WR011038.

[68] Gabriel C. Rau, Martin S. Andersen, Andrew M. McCallum, Hamid Roshan, and R. Ian Acworth. Heat as a tracer to quantify water flow in near-surface sediments. *Earth-Science Reviews*, 129:40–58, 2014. ISSN 0012-8252. doi: 10.1016/j.earscirev.2013.10.015.

[69] Gabriel C. Rau, Mark O. Cuthbert, Andrew M. McCallum, Landon J. S. Halloran, and Martin S. Andersen. Assessing the accuracy of 1-D analytical heat tracing for estimating near-surface sediment thermal diffusivity and water flux under transient conditions. *Journal of Geophysical Research: Earth Surface*, 120(8):1551–1573, aug 2015. ISSN 21699003. doi: 10.1002/2015JF003466. URL http://doi.wiley.com/10.1002/2015JF003466.

[70] Roberto Revelli, Fulvio Boano, Carlo Camporeale, and Luca Ridolfi. Intra-meander hyporheic flow in alluvial rivers. *Water Resources Research*, 44(12), 2008.

[71] D L Rosgen. A CLASSIFICATION OF NATURAL RIVERS. *Catena*, 22:169–199, 1994. ISSN 0341-8162. URL <GotoISI>://A1994NU40600001.

[72] M Shanafield, C Hatch, and G Pohll. Uncertainty in thermal time series analysis estimates of streambed water flux. *Water Resources Research*, 47, 2011. ISSN 0043-1397. doi: W0350410.1029/2010wr009574.

[73] R. W. Stallman. Steady one-dimensional fluid flow in a semi-infinite porous medium with sinusoidal surface temperature. *Journal of Geophysical Research*, 70(12):2821, 1965. ISSN 0148-0227. doi: 10.1029/JZ070i012p02821. URL http://www.agu.org/pubs/crossref/1965/JZ070i012p02821.shtml.

[74] Jack A. Stanford and J. V. Ward. An Ecosystem Perspective of Alluvial Rivers: Connectivity and the Hyporheic Corridor. *Journal of the North American Benthological Society*, 12(1):48–60, 3 1993. ISSN 0887-3593. doi: 10.2307/1467685.

[75] David A. Stonestrom, Jim Constantz, Ty P.A. Ferre, and Stanley A. Leake. Ground-Water Recharge in the Arid and Semiarid Southwestern United States YR - 2007. Technical report, United States Geological Survey, 2007. URL http://pubs.er.usgs.gov/thumbnails/usgs_thumb.jpghttp://pubs.usgs.gov/pp/pp1703/.

[76] David Arthur Stonestrom and Jim Constantz. Heat as a tool for studying the movement of ground water near streams, 2003. URL http://pubs.water.usgs.gov/circ1260/.

[77] David Arthur Stonestrom, Jim Constantz, and Geological Survey (U.S.). *Using temperature to study stream-ground water exchanges*. U.S. Geological Survey, Menlo Park, CA, 2004. URL http://water.usgs.gov/pubs/fs/2004/3010/.

[78] Richard G. Storey, Kenneth W. F. Howard, and D. Dudley Williams. Factors controlling riffle-scale hyporheic exchange flows and their seasonal changes in a gaining stream: A three-dimensional groundwater flow model. *Water Resources Research*, 39(2), 2 2003. ISSN 0043-1397. doi: 10.1029/2002WR001367.

[79] Michael J. Thoma, Warren Barrash, Michael Cardiff, John Bradford, and Jodi Mead. Estimating Unsaturated Hydraulic Functions for Coarse Sediment from a Field-Scale Infiltration Experiment. *Vadose Zone Journal*, 13(3):vzj2013.05.0096, mar 2014. ISSN 15391663. doi: 10.2136/vzj2013.05.0096. URL http://doi.wiley.com/10.2136/vzj2013.05.0096.

[80] D Tonina and J M Buffington. A three-dimensional model for analyzing the effects of salmon redds on hyporheic exchange and egg pocket habitat. *Canadian Journal of Fisheries and Aquatic Sciences*, 66:2157–2173, 2009. ISSN 0706-652X. doi: 10.1139/f09-146. URL <GotoISI>://000273419200011.

[81] D Tonina, C H Luce, B Rieman, J M Buffington, P Goodwin, S R Clayton, S M Ali, J J Barry, and C Berenbrock. Hydrological response to timber harvest in northern Idaho: implications for channel scour and persistence of salmonids. *Hydrological Processes*, 22:3223–3235, 2008. ISSN 0885-6087. doi: 10.1002/hyp.6918. URL <GotoISI>://000258519700001.

[82] Daniele Tonina and John M. Buffington. Hyporheic Exchange in Mountain Rivers I: Mechanics and Environmental Effects. *Geography Compass*, 3(3):1063–1086, 5 2009. ISSN 17498198. doi: 10.1111/j.1749-8198.2009.00226.x. URL `http://doi.wiley.com/10.1111/j.1749-8198.2009.00226.x`.

[83] Daniele Tonina and John M. Buffington. Effects of stream discharge, alluvial depth and bar amplitude on hyporheic flow in pool-riffle channels. *Water Resources Research*, 47: W08508, 8 2011. ISSN 0043-1397. doi: 10.1029/2010WR009140. URL `http://www.agu.org/pubs/crossref/2011/2010WR009140.shtml`.

[84] Daniele Tonina and John M. Buffington. Effects of stream discharge, alluvial depth and bar amplitude on hyporheic flow in pool-riffle channels. *Water Resources Research*, 47(8):W08508, 8 2011. ISSN 0043-1397. doi: 10.1029/2010WR009140. URL `http://www.agu.org/pubs/crossref/2011/2010WR009140.shtml`.

[85] Nico Trauth, Christian Schmidt, Uli Maier, Michael Vieweg, and Jan H. Fleckenstein. Coupled 3-D stream flow and hyporheic flow model under varying stream and ambient groundwater flow conditions in a pool-riffle system. *Water Resources Research*, 49(9): 5834–5850, 9 2013. ISSN 19447973. doi: 10.1002/wrcr.20442.

[86] M. Th. van Genuchten. A Closed-form Equation for Predicting the Hydraulic Conductivity of Unsaturated Soils. *Soil Science Society of America Journal*, 44(5): 892–898, sep 1980. ISSN 03615995. doi: 10.2136/sssaj1980.03615995004400050002x. URL `http://doi.wiley.com/10.2136/sssaj1980.03615995004400050002x`.

[87] T. Vogt, M. Schirmer, and O. A. Cirpka. Investigating riparian groundwater flow close to a losing river using diurnal temperature oscillations at high vertical resolution. *Hydrology and Earth System Sciences*, 16(2):473–487, 2 2012. ISSN 1607-7938. doi: 10.5194/hess-16-473-2012. URL `http://www.hydrol-earth-syst-sci.net/16/473/2012/`.

[88] A S Ward, M N Gooseff, and K Singha. Imaging hyporheic zone solute transport using electrical resistivity. *Hydrological Processes*, 24:948–953, 2010. ISSN 0885-6087. doi: 10.1002/hyp.7672. URL `<GotoISI>://000276161500012`.

[89] Adam S. Ward. The evolution and state of interdisciplinary hyporheic research, 1 2016. ISSN 20491948.

[90] Hadley Wickham, Mara Averick, Jennifer Bryan, Winston Chang, Lucy McGowan, Romain François, Garrett Grolemund, Alex Hayes, Lionel Henry, Jim Hester, Max Kuhn, Thomas Pedersen, Evan Miller, Stephan Bache, Kirill Müller, Jeroen Ooms, David Robinson, Dana Seidel, Vitalie Spinu, Kohske Takahashi, Davis Vaughan, Claus Wilke, Kara Woo, and Hiroaki Yutani. Welcome to the Tidyverse. *Journal of Open Source Software*, 4(43):1686, 11 2019. ISSN 2475-9066. doi: 10.21105/joss.01686.

[91] Ellen Wohl, Stuart N. Lane, and Andrew C. Wilcox. The science and practice of river restoration. *Water Resources Research*, 51(8):5974–5997, 8 2015. ISSN 0043-1397. doi: 10.1002/2014WR016874.

[92] Anders Wörman, Aaron I. Packman, Lars Marklund, Judson W. Harvey, and Susa H. Stone. Exact three-dimensional spectral solution to surface-groundwater interactions with arbitrary surface topography. *Geophysical Research Letters*, 33(7):L07402, 2006. doi: 10.1029/2006GL025747.

[93] Natalia V. Zakharova, David S. Goldberg, E. Charlotte Sullivan, Michael M. Herron, and James A. Grau. Petrophysical and geochemical properties of Columbia River flood basalt: Implications for carbon sequestration. *Geochemistry, Geophysics, Geosystems*, 13(11):2012GC004305, nov 2012. ISSN 1525-2027. doi: 10.1029/2012GC004305. URL `https://onlinelibrary.wiley.com/doi/abs/10.1029/2012GC004305`.

APPENDICES

APPENDIX A

MODEL RMSD

Table 13: RMSD (°C) between model year 4 and 5 for K = 100 md^{-1}.

	RMSD (°C)		
	U	UB	UBS
Flow Path (m)			
0	0e+00	0e+00	0e+00
10	0e+00	5.54e-05	5.02e-05
20	0e+00	1.52e-04	1.38e-04
30	0e+00	2.52e-04	2.26e-04
40	0e+00	3.46e-04	3.05e-04
50	0e+00	4.38e-04	3.75e-04
60	1.36e-11	5.26e-04	4.35e-04
70	1.36e-11	6.11e-04	4.86e-04
80	1.36e-11	6.96e-04	5.29e-04
90	6.06e-19	7.78e-04	5.64e-04
100	1.36e-10	8.6e-04	5.92e-04
200	2.73e-11	1.62e-03	6.47e-04
300	1.36e-11	2.29e-03	5.56e-04
400	1.23e-10	2.84e-03	4.63e-04
500	1.36e-11	3.28e-03	3.97e-04
600	1.09e-10	3.56e-03	3.59e-04
700	1.91e-10	3.65e-03	3.4e-04
800	1.36e-11	3.53e-03	3.32e-04
900	5.46e-11	3.23e-03	3.3e-04
1000	1.23e-10	2.86e-03	3.3e-04

Table 14: RMSE (°C) between model year 4 and 5 for $K = 400$ md^{-1}.

	RMSD (°C)		
	U	UB	UBS
Flow Path (m)			
0	0e+00	0e+00	0e+00
10	0e+00	1.2e-05	1.16e-05
20	1.36e-10	3.55e-05	3.42e-05
30	0e+00	6.07e-05	5.82e-05
40	0e+00	8.54e-05	8.09e-05
50	0e+00	1.09e-04	1.02e-04
60	0e+00	1.32e-04	1.2e-04
70	0e+00	1.55e-04	1.37e-04
80	0e+00	1.77e-04	1.52e-04
90	0e+00	1.99e-04	1.64e-04
100	0e+00	2.21e-04	1.75e-04
200	0e+00	4.34e-04	2.03e-04
300	0e+00	6.45e-04	1.54e-04
400	0e+00	8.53e-04	8.54e-05
500	1.36e-11	1.06e-03	2.02e-05
600	0e+00	1.25e-03	3.3e-05
700	0e+00	1.44e-03	7.31e-05
800	0e+00	1.63e-03	1.02e-04
900	0e+00	1.81e-03	1.21e-04
1000	0e+00	1.98e-03	1.35e-04

APPENDIX B

EMPIRICAL PARAMETER SOLUTIONS

Table 15: Fitted solutions of amplitude ratio ($A_{x_1:x_2}$) using $K = 100$ m/d.

A_2/A_1; $K = 100$ (m/d)

	U	UB	UBS
Flow Path Length (m)			
0	1.000	1.000	1.000
10	0.999	0.982	0.988
20	0.997	0.953	0.966
30	0.996	0.924	0.941
40	0.994	0.897	0.914
50	0.993	0.872	0.885
60	0.991	0.848	0.855
70	0.990	0.825	0.824
80	0.988	0.803	0.793
90	0.987	0.781	0.762
100	0.985	0.761	0.732
200	0.970	0.582	0.544
300	0.956	0.446	0.551
400	0.942	0.342	0.569
500	0.928	0.261	0.569
600	0.914	0.199	0.569
700	0.900	0.154	0.569
800	0.887	0.120	0.569
900	0.874	0.090	0.569
1000	0.861	0.064	0.569

Table 16: Fitted solutions of amplitude ratio ($A_{x_1:x_2}$) using $K = 400$ m/d.

A_2/A_1; $K = 400$ (m/d)			
	U	UB	UBS
Flow Path Length (m)			
0	1.000	1.000	1.000
10	1.000	0.996	0.999
20	1.000	0.989	0.997
30	1.000	0.982	0.995
40	1.000	0.975	0.993
50	1.000	0.968	0.990
60	0.999	0.961	0.987
70	0.999	0.955	0.984
80	0.999	0.949	0.981
90	0.999	0.942	0.977
100	0.999	0.936	0.974
200	0.998	0.878	0.934
300	0.997	0.823	0.896
400	0.996	0.771	0.866
500	0.995	0.723	0.847
600	0.994	0.678	0.837
700	0.994	0.636	0.833
800	0.993	0.596	0.832
900	0.992	0.560	0.832
1000	0.991	0.526	0.832

Table 17: Fitted solutions of phase difference ($\Delta\phi$) using K = 100 m/d.

$\Delta\phi$; K = 100 (m/d)			
	U	UB	UBS
Flow Path Length (m)			
0	0.000	0.000	0.000
10	0.121	0.137	0.124
20	0.241	0.284	0.243
30	0.362	0.429	0.350
40	0.483	0.573	0.445
50	0.604	0.715	0.530
60	0.725	0.856	0.604
70	0.846	0.996	0.668
80	0.967	1.136	0.723
90	1.088	1.276	0.769
100	1.209	1.416	0.807
200	2.417	2.811	0.829
300	3.626	4.205	0.736
400	4.835	5.598	0.742
500	6.044	6.990	0.751
600	7.253	8.389	0.752
700	8.462	9.793	0.751
800	9.671	11.172	0.751
900	10.880	12.525	0.752
1000	12.076	13.939	0.752

Table 18: Fitted solutions of phase difference ($\Delta\phi$) using $K = 400$ m/d.

$\Delta\phi$; $K = 400$ (m/d)			
	U	UB	UBS
Flow Path Length (m)			
0	0.000	0.000	0.000
10	0.030	0.034	0.029
20	0.060	0.072	0.056
30	0.090	0.109	0.082
40	0.121	0.147	0.107
50	0.151	0.184	0.129
60	0.181	0.221	0.151
70	0.211	0.257	0.172
80	0.241	0.294	0.191
90	0.272	0.330	0.209
100	0.302	0.367	0.226
200	0.604	0.730	0.351
300	0.907	1.093	0.413
400	1.209	1.457	0.439
500	1.511	1.820	0.445
600	1.814	2.184	0.444
700	2.116	2.548	0.440
800	2.418	2.912	0.437
900	2.720	3.275	0.435
1000	3.020	3.635	0.435

Table 19: Fitted solutions of η using $K = 100$ m/d.

η; $K = 100$ (m/d)			
	U	UB	UBS
Flow Path Length (m)			
0	NA	NA	NA
10	0.0125	0.1314	0.0968
20	0.0124	0.1696	0.1408
30	0.0124	0.1837	0.1729
40	0.0124	0.1894	0.2016
50	0.0124	0.1919	0.2299
60	0.0124	0.1929	0.2589
70	0.0124	0.1933	0.2890
80	0.0124	0.1934	0.3204
90	0.0124	0.1934	0.3532
100	0.0124	0.1934	0.3873
200	0.0124	0.1924	0.7341
300	0.0124	0.1919	0.8104
400	0.0124	0.1917	0.7612
500	0.0124	0.1920	0.7500
600	0.0124	0.1924	0.7512
700	0.0124	0.1912	0.7510
800	0.0124	0.1897	0.7504
900	0.0124	0.1923	0.7502
1000	0.0124	0.1975	0.7501

Table 20: Fitted solutions of η using $K = 400$ m/d.

η; $K = 400$ (m/d)			
	U	UB	UBS
Flow Path Length (m)			
0	NA	NA	NA
10	0.0031	0.1067	0.0303
20	0.0031	0.1477	0.0468
30	0.0030	0.1648	0.0588
40	0.0031	0.1725	0.0688
50	0.0030	0.1761	0.0778
60	0.0030	0.1778	0.0861
70	0.0030	0.1787	0.0941
80	0.0030	0.1791	0.1020
90	0.0030	0.1793	0.1097
100	0.0030	0.1794	0.1174
200	0.0030	0.1789	0.1940
300	0.0030	0.1787	0.2666
400	0.0030	0.1785	0.3275
500	0.0030	0.1784	0.3720
600	0.0030	0.1782	0.4001
700	0.0030	0.1779	0.4151
800	0.0030	0.1776	0.4214
900	0.0030	0.1773	0.4229
1000	0.0030	0.1770	0.4224

Table 21: Fitted solutions of x_d (m) using $K = 100$ m/d.

x_d; $K = 100$ (m/d)			
	U	UB	UBS
Flow Path Length (m)			
0	NA	NA	NA
10	6,661	556	833
20	6,657	415	585
30	6,658	380	496
40	6,657	369	445
50	6,657	365	411
60	6,657	363	384
70	6,657	363	362
80	6,657	364	345
90	6,658	365	331
100	6,658	365	320
200	6,658	370	329
300	6,658	372	503
400	6,657	373	709
500	6,658	372	888
600	6,658	372	1,063
700	6,658	374	1,241
800	6,657	378	1,419
900	6,658	374	1,596
1000	6,673	363	1,774

Table 22: Fitted solutions of x_d (m) using $K = 400$ m/d.

x_d; $K = 400$ (m/d)			
	U	UB	UBS
Flow Path Length (m)			
0	NA	NA	NA
10	105,393	2,762	11,397
20	108,184	1,892	7,560
30	108,518	1,664	6,202
40	108,697	1,580	5,457
50	108,271	1,544	4,966
60	108,392	1,528	4,610
70	108,647	1,521	4,334
80	108,486	1,519	4,110
90	108,393	1,519	3,924
100	108,520	1,520	3,765
200	108,669	1,531	2,937
300	108,641	1,536	2,722
400	108,629	1,538	2,783
500	108,666	1,540	3,018
600	108,659	1,542	3,379
700	108,676	1,544	3,830
800	108,656	1,547	4,341
900	108,657	1,550	4,887
1000	108,907	1,555	5,449

Table 23: Fitted solutions of v_d (ms^{-1}) using $K = 100$ m/d.

v_d; $K = 100$ (m/d)			
	U	UB	UBS
Flow Path Length (m)			
0	NA	NA	NA
10	1.4	1.8	1.9
20	1.4	1.9	2.1
30	1.4	2.0	2.4
40	1.4	2.0	2.6
50	1.4	2.0	2.9
60	1.4	2.0	3.2
70	1.4	2.0	3.5
80	1.4	2.0	3.8
90	1.4	2.0	4.2
100	1.4	2.0	4.5
200	1.4	2.1	10.2
300	1.4	2.1	17.4
400	1.4	2.1	22.9
500	1.4	2.1	28.2
600	1.4	2.1	33.9
700	1.4	2.1	39.5
800	1.4	2.1	45.2
900	1.4	2.1	50.8
1000	1.4	2.1	56.4

Table 24: Fitted solutions of v_d (ms^{-1}) using K = 400 m/d.

v_d; K = 400 (m/d)			
	U	UB	UBS
Flow Path Length (m)			
0	NA	NA	NA
10	5.8	7.0	6.3
20	5.7	7.3	6.9
30	5.7	7.5	7.4
40	5.7	7.6	7.9
50	5.7	7.6	8.3
60	5.7	7.6	8.8
70	5.7	7.6	9.3
80	5.7	7.6	9.8
90	5.7	7.7	10.3
100	5.7	7.7	10.8
200	5.7	7.7	16.5
300	5.7	7.7	23.5
400	5.7	7.7	31.6
500	5.7	7.7	40.6
600	5.7	7.7	49.9
700	5.7	7.7	59.4
800	5.7	7.7	68.6
900	5.7	7.7	77.6
1000	5.7	7.7	86.4

Table 25: Fitted solutions for K using K = 100 m/d.

K; K = 100 (m/d)			
	U	UB	UBS
Flow Path Length (m)			
0	NA	NA	NA
10	100	85	96
20	100	80	96
30	100	79	98
40	100	79	100
50	100	79	103
60	100	79	105
70	100	79	107
80	100	79	109
90	100	79	110
100	100	79	111
200	100	80	87
300	100	80	102
400	100	80	174
500	100	80	225
600	100	80	269
700	100	80	314
800	100	81	360
900	100	81	405
1000	100	80	450

Table 26: Fitted solutions for K using $K = 400$ m/d.

K; $K = 400$ (m/d)			
	U	UB	UBS
Flow Path Length (m)			
0	NA	NA	NA
10	405	348	416
20	402	323	426
30	402	314	438
40	401	310	450
50	401	309	461
60	401	308	473
70	401	308	485
80	401	309	496
90	400	309	508
100	400	309	520
200	400	311	639
300	400	311	761
400	400	311	888
500	400	312	1,028
600	400	312	1,184
700	400	312	1,357
800	400	312	1,545
900	400	312	1,741
1000	400	312	1,940

Table 27: Fitted solutions for β using K = 100 m/d.

β; K = 100 (m/d)

Flow Path Length (m)	U	UB	UBS
0	NA	NA	NA
10	1	10	8
20	1	12	12
30	1	13	15
40	1	14	19
50	1	14	23
60	1	14	28
70	1	14	33
80	1	14	40
90	1	14	47
100	1	14	56
200	1	14	384
300	1	14	963
400	1	14	976
500	1	14	1,141
600	1	14	1,376
700	1	14	1,605
800	1	14	1,828
900	1	14	2,054
1000	1	15	2,282

Table 28: Fitted solutions for β using $K = 400$ m/d.

β; $K = 400$ (m/d)			
	U	UB	UBS
Flow Path Length (m)			
0	NA	NA	NA
10	1	32	10
20	1	42	17
30	1	46	22
40	1	48	26
50	1	49	30
60	1	50	34
70	1	50	39
80	1	50	43
90	1	50	48
100	1	50	53
200	1	51	115
300	1	51	208
400	1	51	334
500	1	51	485
600	1	50	644
700	1	50	797
800	1	50	937
900	1	50	1,064
1000	1	50	1,183

APPENDIX C

AQUIFER DISCHARGE FRACTIONAL DECOMPOSITION

Derivation

From Darcy's law, total aquifer discharge is the product of wetted area and specific discharge:

$$Q_\uparrow = A\, q_\uparrow$$

Let subscripts 1 and 2 denote two model states being compared. Fractional changes are defined as:

$$\frac{\Delta A}{A} = \frac{A_2 - A_1}{A_1}, \qquad \frac{\Delta q_\uparrow}{q_\uparrow} = \frac{q_{\uparrow,2} - q_{\uparrow,1}}{q_{\uparrow,1}}$$

so that:

$$A_2 = A_1\left(1 + \frac{\Delta A}{A}\right), \qquad q_{\uparrow,2} = q_{\uparrow,1}\left(1 + \frac{\Delta q_\uparrow}{q_\uparrow}\right)$$

The discharge in state 2 is:

$$Q_{\uparrow,2} = A_2\, q_{\uparrow,2} = Q_{\uparrow,1}\left(1 + \frac{\Delta A}{A}\right)\left(1 + \frac{\Delta q_\uparrow}{q_\uparrow}\right)$$

Expanding the product:

$$Q_{\uparrow,2} = Q_{\uparrow,1}\left(1 + \frac{\Delta A}{A} + \frac{\Delta q_\uparrow}{q_\uparrow} + \frac{\Delta A}{A}\cdot\frac{\Delta q_\uparrow}{q_\uparrow}\right)$$

Subtracting $Q_{\uparrow,1}$ and dividing by $Q_{\uparrow,1}$ yields the decomposition:

$$\frac{\Delta Q_\uparrow}{Q_\uparrow} = \frac{\Delta A}{A} + \frac{\Delta q_\uparrow}{q_\uparrow} + \frac{\Delta A}{A}\cdot\frac{\Delta q_\uparrow}{q_\uparrow} \tag{53}$$

The three terms are: (1) the area term, representing the fractional change attributable to area change alone; (2) the specific discharge term, representing the fractional change attributable to $q_\uparrow$ change alone; and (3) the interaction term, a bookkeeping consequence of the multiplicative structure of Darcy's law. The interaction term is negligible when fractional changes are small but becomes substantial when both $\Delta A/A$ and $\Delta q_\uparrow/q_\uparrow$ are large. At the fractional changes present in this analysis (commonly 40–200%), the interaction term must be retained.

The identity was verified against all 40 model states. For every pairwise comparison, the three-term sum matched the directly computed fractional change to machine precision (maximum residual: 8.88×10^{-16}).

Within-Channel Flow Transitions

All values are expressed as percentages of the lower flow state's $Q_{\uparrow}$. Position 0 corresponds to existing alluvial depth; positions 1–4 correspond to successive 0.5 m bedrock lowering increments.

Unrestored Geomorphology

Table 29: Unrestored: base flow → annual flood.

Position	ΔS ($\times 10^3$ m^3)	$\Delta A/A$ (%)	$\Delta q_{\uparrow}/q_{\uparrow}$ (%)	Interaction (%)	$\Delta Q_{\uparrow}/Q_{\uparrow}$ (%)
0	68.9	192.5	−39.3	−75.7	77.5
1	76.4	193.0	−38.2	−73.8	81.0
2	68.1	193.9	−36.0	−69.8	88.1
3	55.3	192.6	−34.0	−65.5	93.1
4	48.5	194.4	−32.8	−63.8	97.7

Table 30: Unrestored: annual flood → bankfull.

Position	ΔS ($\times 10^3$ m^3)	$\Delta A/A$ (%)	$\Delta q_{\uparrow}/q_{\uparrow}$ (%)	Interaction (%)	$\Delta Q_{\uparrow}/Q_{\uparrow}$ (%)
0	37.5	85.5	17.0	14.6	117.1
1	33.2	85.0	15.1	12.9	112.9
2	35.5	84.4	14.2	12.0	110.6
3	30.3	84.1	14.0	11.8	110.0
4	28.5	83.3	14.1	11.7	109.1

Table 31: Unrestored: bankfull → overbank.

Position	ΔS ($\times 10^3$ m^3)	$\Delta A/A$ (%)	$\Delta q_{\uparrow}/q_{\uparrow}$ (%)	Interaction (%)	$\Delta Q_{\uparrow}/Q_{\uparrow}$ (%)
0	17.0	47.8	25.0	12.0	84.8
1	20.6	47.3	22.7	10.7	80.7
2	18.5	46.7	20.2	9.4	76.3
3	20.3	46.1	18.5	8.5	73.1
4	21.7	45.7	17.0	7.8	70.6

Restored Geomorphology

Table 32: Restored: base flow → annual flood.

Position	ΔS ($\times 10^3$ m^3)	$\Delta A/A$ (%)	$\Delta q_\uparrow/q_\uparrow$ (%)	Interaction (%)	$\Delta Q_\uparrow/Q_\uparrow$ (%)
0	34.9	203.0	−24.4	−49.6	129.0
1	35.0	202.7	−24.4	−49.4	128.9
2	36.0	204.0	−23.9	−48.7	131.5
3	37.7	203.6	−23.1	−47.0	133.5
4	40.2	203.6	−22.7	−46.2	134.8

Table 33: Restored: annual flood → bankfull.

Position	ΔS ($\times 10^3$ m^3)	$\Delta A/A$ (%)	$\Delta q_\uparrow/q_\uparrow$ (%)	Interaction (%)	$\Delta Q_\uparrow/Q_\uparrow$ (%)
0	21.9	16.1	9.6	1.6	27.3
1	20.5	16.3	8.3	1.4	25.9
2	22.1	16.2	7.3	1.2	24.7
3	24.9	16.4	6.3	1.0	23.7
4	26.2	16.4	5.9	1.0	23.3

Table 34: Restored: bankfull → overbank.

Position	ΔS ($\times 10^3$ m^3)	$\Delta A/A$ (%)	$\Delta q_\uparrow/q_\uparrow$ (%)	Interaction (%)	$\Delta Q_\uparrow/Q_\uparrow$ (%)
0	9.1	44.3	−28.7	−12.7	2.9
1	9.8	44.3	−29.4	−13.0	1.9
2	13.2	44.3	−29.7	−13.2	1.5
3	13.7	44.1	−29.7	−13.1	1.2
4	15.7	44.0	−29.8	−13.1	1.1

Between-Channel Comparisons: Unrestored → Restored

All Δ values are fractional changes (%) using the unrestored state as the base: (Restored − Unrestored) / Unrestored × 100%.

Table 35: Unrestored → restored at base flow.

Position	ΔS ($\times 10^3$ m^3)	$\Delta A/A$ (%)	$\Delta q_\uparrow/q_\uparrow$ (%)	Interaction (%)	$\Delta Q_\uparrow/Q_\uparrow$ (%)
0	69.8	144.4	71.3	103.0	318.7
1	75.5	143.2	68.7	98.4	310.3
2	65.1	141.5	68.8	97.3	307.7
3	48.2	140.0	69.1	96.7	305.8
4	40.3	140.1	68.4	95.8	304.3

Table 36: Unrestored → restored at annual flood.

Position	ΔS ($\times 10^3$ m^3)	$\Delta A/A$ (%)	$\Delta q_\uparrow/q_\uparrow$ (%)	Interaction (%)	$\Delta Q_\uparrow/Q_\uparrow$ (%)
0	35.8	153.1	113.4	173.7	440.2
1	34.2	151.3	106.5	161.0	418.8
2	33.1	149.8	100.8	151.0	401.7
3	30.6	149.1	97.1	144.7	390.9
4	31.9	147.6	93.9	138.5	380.0

Table 37: Unrestored → restored at bankfull.

Position	ΔS ($\times 10^3$ m^3)	$\Delta A/A$ (%)	$\Delta q_\uparrow/q_\uparrow$ (%)	Interaction (%)	$\Delta Q_\uparrow/Q_\uparrow$ (%)
0	20.2	58.5	99.9	58.4	216.8
1	21.4	57.9	94.3	54.6	206.8
2	19.7	57.5	88.6	50.9	197.0
3	25.2	57.4	83.7	48.1	189.2
4	29.6	57.2	80.0	45.8	183.1

Table 38: Unrestored → restored at overbank.

Position	ΔS ($\times 10^3$ m^3)	$\Delta A/A$ (%)	$\Delta q_\uparrow/q_\uparrow$ (%)	Interaction (%)	$\Delta Q_\uparrow/Q_\uparrow$ (%)
0	12.3	54.6	14.0	7.7	76.3
1	10.6	54.8	11.9	6.5	73.1
2	14.3	55.0	10.3	5.7	70.9
3	18.6	55.3	8.9	4.9	69.2
4	23.6	55.4	8.0	4.4	67.7

APPENDIX D

TURNOVER RATE FRACTIONAL DECOMPOSITION

Derivation

Mean turnover rate is defined as total aquifer discharge divided by total aquifer storage:

$$\frac{1}{\bar{\tau}} = \frac{Q_{\uparrow}}{S}$$

Because $Q_{\uparrow} = A\, q_{\uparrow}$, this can be rewritten as:

$$\frac{1}{\bar{\tau}} = \frac{A\, q_{\uparrow}}{S} = q_{\uparrow} \cdot \frac{A}{S}$$

This expression is multiplicative in $q_{\uparrow}$ and A/S, exactly as $Q_{\uparrow} = A\, q_{\uparrow}$ is multiplicative in A and $q_{\uparrow}$. The same fractional decomposition therefore applies.

Let subscripts 1 and 2 denote two model states. Fractional changes are:

$$\frac{\Delta q_{\uparrow}}{q_{\uparrow}} = \frac{q_{\uparrow,2} - q_{\uparrow,1}}{q_{\uparrow,1}}, \qquad \frac{\Delta(A/S)}{A/S} = \frac{(A/S)_2 - (A/S)_1}{(A/S)_1}$$

The turnover rate in state 2 is:

$$\frac{1}{\bar{\tau}_2} = q_{\uparrow,1}\left(1 + \frac{\Delta q_{\uparrow}}{q_{\uparrow}}\right) \cdot (A/S)_1 \left(1 + \frac{\Delta(A/S)}{A/S}\right) = \frac{1}{\bar{\tau}_1}\left(1 + \frac{\Delta q_{\uparrow}}{q_{\uparrow}}\right)\left(1 + \frac{\Delta(A/S)}{A/S}\right)$$

Expanding and simplifying:

$$\frac{\Delta(1/\bar{\tau})}{1/\bar{\tau}} = \frac{\Delta q_{\uparrow}}{q_{\uparrow}} + \frac{\Delta(A/S)}{A/S} + \frac{\Delta q_{\uparrow}}{q_{\uparrow}} \cdot \frac{\Delta(A/S)}{A/S} \tag{54}$$

The three terms are: (1) the specific discharge term, reflecting gradient intensity; (2) the area-to-storage ratio term, reflecting the storage burden per unit exchange interface; and (3) the interaction term. The $q_{\uparrow}$ term is positive when gradients steepen and negative when newly wetted low-relief surfaces dilute the spatial average. The A/S term is positive when wetted area expands faster than storage, reducing the volume each square meter of streambed must turn over. The interaction term is positive when both factors change in the same direction and negative when they oppose each other.

Percentage contributions are computed as:

$$\%\text{ from } q_{\uparrow} = \frac{\Delta q_{\uparrow}/q_{\uparrow}}{\Delta(1/\bar{\tau})/(1/\bar{\tau})} \times 100, \qquad \%\text{ from } A/S = \frac{\Delta(A/S)/(A/S)}{\Delta(1/\bar{\tau})/(1/\bar{\tau})} \times 100$$

These sum to 100% with the interaction percentage. Percentages become uninformative when $\Delta(1/\bar{\tau})/(1/\bar{\tau}) \approx 0$; in such cases the absolute fractional values are reported.

The identity was verified against all 40 model states. Maximum absolute residual across all 50 pairwise comparisons: 8.88×10^{-16}.

Within-Channel Flow Transitions

Position 0 corresponds to existing alluvial depth; positions 1–4 correspond to successive 0.5 m bedrock lowering increments. Percentage columns express each term as a share of the total fractional change. Dashes indicate that percentages are uninformative because the total change is near zero.

Unrestored Geomorphology

Table 39: Unrestored turnover decomposition: base flow → annual flood.

Pos.	$\frac{\Delta(1/\bar{\tau})}{1/\bar{\tau}}$	$\frac{\Delta q_\uparrow}{q_\uparrow}$	$\frac{\Delta(A/S)}{A/S}$	Inter.	% $q_\uparrow$	% A/S	% Inter.
0	+0.469	−0.393	+1.421	−0.559	−83.9	+303.0	−119.2
1	+0.542	−0.382	+1.497	−0.572	−70.5	+276.0	−105.5
2	+0.677	−0.360	+1.621	−0.583	−53.1	+239.3	−86.1
3	+0.787	−0.340	+1.708	−0.581	−43.2	+217.0	−73.8
4	+0.865	−0.328	+1.777	−0.584	−38.0	+205.4	−67.4

Table 40: Unrestored turnover decomposition: annual flood → bankfull.

Pos.	$\frac{\Delta(1/\bar{\tau})}{1/\bar{\tau}}$	$\frac{\Delta q_\uparrow}{q_\uparrow}$	$\frac{\Delta(A/S)}{A/S}$	Inter.	% $q_\uparrow$	% A/S	% Inter.
0	+0.985	+0.170	+0.697	+0.119	+17.3	+70.7	+12.0
1	+1.001	+0.151	+0.738	+0.112	+15.1	+73.7	+11.2
2	+0.994	+0.142	+0.745	+0.106	+14.3	+75.0	+10.7
3	+1.018	+0.140	+0.769	+0.108	+13.8	+75.6	+10.6
4	+1.024	+0.141	+0.774	+0.109	+13.8	+75.6	+10.6

Table 41: Unrestored turnover decomposition: bankfull → overbank.

Pos.	$\frac{\Delta(1/\bar{\tau})}{1/\bar{\tau}}$	$\frac{\Delta q_\uparrow}{q_\uparrow}$	$\frac{\Delta(A/S)}{A/S}$	Inter.	% $q_\uparrow$	% A/S	% Inter.
0	+0.779	+0.250	+0.423	+0.106	+32.1	+54.3	+13.6
1	+0.741	+0.227	+0.420	+0.095	+30.6	+56.6	+12.8
2	+0.715	+0.202	+0.427	+0.086	+28.3	+59.7	+12.1
3	+0.687	+0.185	+0.423	+0.078	+26.9	+61.7	+11.4
4	+0.665	+0.170	+0.422	+0.072	+25.6	+63.5	+10.8

Restored Geomorphology

Table 42: Restored turnover decomposition: base flow → annual flood.

Pos.	$\frac{\Delta(1/\bar{\tau})}{1/\bar{\tau}}$	$\frac{\Delta q_\uparrow}{q_\uparrow}$	$\frac{\Delta(A/S)}{A/S}$	Inter.	% $q_\uparrow$	% A/S	% Inter.
0	+1.106	−0.244	+1.787	−0.437	−22.1	+161.5	−39.5
1	+1.143	−0.244	+1.834	−0.447	−21.3	+160.4	−39.1
2	+1.189	−0.239	+1.874	−0.447	−20.1	+157.7	−37.6
3	+1.222	−0.231	+1.889	−0.436	−18.9	+154.6	−35.7
4	+1.241	−0.227	+1.899	−0.431	−18.3	+152.9	−34.7

Table 43: Restored turnover decomposition: annual flood → bankfull.

Pos.	$\frac{\Delta(1/\bar{\tau})}{1/\bar{\tau}}$	$\frac{\Delta q_\uparrow}{q_\uparrow}$	$\frac{\Delta(A/S)}{A/S}$	Inter.	% $q_\uparrow$	% A/S	% Inter.
0	+0.213	+0.096	+0.106	+0.010	+45.4	+49.8	+4.8
1	+0.214	+0.083	+0.121	+0.010	+38.8	+56.5	+4.7
2	+0.207	+0.073	+0.125	+0.009	+35.3	+60.3	+4.4
3	+0.199	+0.063	+0.127	+0.008	+31.8	+64.1	+4.1
4	+0.198	+0.059	+0.131	+0.008	+30.0	+66.1	+3.9

Table 44: Restored turnover decomposition: bankfull → overbank. Percentages omitted because $\Delta(1/\bar{\tau})/(1/\bar{\tau}) \approx 0$.

Pos.	$\frac{\Delta(1/\bar{\tau})}{1/\bar{\tau}}$	$\frac{\Delta q_\uparrow}{q_\uparrow}$	$\frac{\Delta(A/S)}{A/S}$	Inter.
0	+0.009	−0.287	+0.415	−0.119
1	+0.002	−0.294	+0.419	−0.123
2	−0.005	−0.297	+0.416	−0.124
3	−0.005	−0.297	+0.416	−0.124
4	−0.007	−0.298	+0.416	−0.124

Between-Channel Comparisons: Unrestored → Restored

Fractional change in turnover rate from the unrestored to the restored state at matched flow and alluvial depth. The three decomposition terms sum exactly to the total fractional change.

Table 45: Turnover rate, unrestored → restored at base flow.

Pos.	$1/\bar{\tau}$ Unrest.	$1/\bar{\tau}$ Rest.	Ratio	$\frac{\Delta(1/\bar{\tau})}{1/\bar{\tau}}$	$\frac{\Delta q_\uparrow}{q_\uparrow}$	$\frac{\Delta(A/S)}{A/S}$	Inter.
0	0.01614	0.05582	3.46×	+2.458	+0.714	+1.018	+0.727
1	0.01427	0.04995	3.50×	+2.502	+0.687	+1.076	+0.739
2	0.01233	0.04502	3.65×	+2.653	+0.688	+1.164	+0.801
3	0.01081	0.04098	3.79×	+2.792	+0.691	+1.243	+0.859
4	0.00979	0.03770	3.85×	+2.851	+0.684	+1.286	+0.880

Table 46: Turnover rate, unrestored → restored at annual flood.

Pos.	$1/\bar{\tau}$ Unrest.	$1/\bar{\tau}$ Rest.	Ratio	$\frac{\Delta(1/\bar{\tau})}{1/\bar{\tau}}$	$\frac{\Delta q_{\uparrow}}{q_{\uparrow}}$	$\frac{\Delta(A/S)}{A/S}$	Inter.
0	0.02371	0.11758	4.96×	+3.959	+1.134	+1.324	+1.501
1	0.02200	0.10705	4.87×	+3.866	+1.065	+1.357	+1.444
2	0.02067	0.09853	4.77×	+3.766	+1.008	+1.374	+1.385
3	0.01931	0.09105	4.71×	+3.715	+0.971	+1.392	+1.352
4	0.01826	0.08450	4.63×	+3.627	+0.939	+1.387	+1.302

Table 47: Turnover rate, unrestored → restored at bankfull.

Pos.	$1/\bar{\tau}$ Unrest.	$1/\bar{\tau}$ Rest.	Ratio	$\frac{\Delta(1/\bar{\tau})}{1/\bar{\tau}}$	$\frac{\Delta q_{\uparrow}}{q_{\uparrow}}$	$\frac{\Delta(A/S)}{A/S}$	Inter.
0	0.04707	0.14256	3.03×	+2.029	+0.999	+0.515	+0.514
1	0.04402	0.12996	2.95×	+1.953	+0.943	+0.520	+0.490
2	0.04122	0.11888	2.88×	+1.884	+0.886	+0.530	+0.469
3	0.03897	0.10915	2.80×	+1.801	+0.837	+0.525	+0.439
4	0.03695	0.10122	2.74×	+1.739	+0.800	+0.521	+0.417

Table 48: Turnover rate, unrestored → restored at overbank.

Pos.	$1/\bar{\tau}$ Unrest.	$1/\bar{\tau}$ Rest.	Ratio	$\frac{\Delta(1/\bar{\tau})}{1/\bar{\tau}}$	$\frac{\Delta q_{\uparrow}}{q_{\uparrow}}$	$\frac{\Delta(A/S)}{A/S}$	Inter.
0	0.08376	0.14377	1.72×	+0.717	+0.140	+0.506	+0.071
1	0.07664	0.13024	1.70×	+0.699	+0.119	+0.519	+0.062
2	0.07070	0.11835	1.67×	+0.674	+0.103	+0.518	+0.053
3	0.06572	0.10862	1.65×	+0.653	+0.089	+0.517	+0.046
4	0.06152	0.10057	1.63×	+0.635	+0.080	+0.514	+0.041